

DEPARTMENT OF MATERIALS SCIENCE
PHD PROGRAM IN SCIENCE AND NANOTECHNOLOGY OF MATERIALS,
CYCLE XXX
CURRICULUM IN MATERIALS SCIENCE

**ROLE OF NONRADIATIVE SURFACE
DEFECTS ON EXCITON
RECOMBINATION PROCESSES IN
SEMICONDUCTOR COLLOIDAL
NANOSTRUCTURES**

MONICA LORENZON


Reg. n° 718458

Tutor: Prof. Francesco Meinardi


Co-tutor: Prof. Sergio Brovelli

Coordinator: Prof. Marco Bernasconi

ACADEMIC YEAR 2016/2017



This work has been supported by the Fondazione Cassa di Risparmio di Tortona, which I warmly thank for giving me the opportunity of pursuing my doctoral studies.



Role of nonradiative surface defects on exciton recombination processes in semiconductor colloidal nanostructures

CONTENTS

INTRODUCTION	5
---------------------	----------

CHAPTER 1: EFFECT OF NONRADIATIVE DEFECTS AND ENVIRONMENTAL OXYGEN ON EXCITON RECOMBINATION PROCESSES IN CsPbBr_3 PEROVSKITE NANOCRYSTALS	13
--	-----------

OVERVIEW	13
1.1 INTRODUCTION	15
1.2 RESULTS AND DISCUSSION	18
1.2.1 STRUCTURAL AND OPTICAL PROPERTIES OF CsPbBr_3 NANOCRYSTALS	18
1.2.2 SPECTRO-ELECTROCHEMISTRY EXPERIMENTS	20
1.2.3 OXYGEN SENSING EXPERIMENTS	28
1.3 CONCLUSIONS	33

CHAPTER 2: REVERSE OXYGEN SENSING WITH COLLOIDAL NANOPATELETS TOWARDS HIGHLY EMISSIVE PHOTORESPONSIVE VARNISHES	35
--	-----------

OVERVIEW	35
2.1 INTRODUCTION	37
2.2 RESULTS AND DISCUSSION	40
2.2.1 SYNTHESIS AND OPTICAL PROPERTIES OF COLLOIDAL NANOPATELETS	40
2.2.2 OXYGEN SENSING EXPERIMENTS	42
2.2.3 TIME-RESOLVED SPECTROSCOPY OF COLLOIDAL NANOPATELETS	53
2.2.4 MAGNETO-OPTICAL PROPERTIES OF COLLOIDAL NANOPATELETS	57
2.2.5 SPECTRO-ELECTROCHEMISTRY EXPERIMENTS	59
2.2.6 KINETIC MODEL OF SURFACE TRAPPING IN COLLOIDAL NANOPATELETS	63
2.2.7 RATE EQUATIONS	64

2.2.8	DEMONSTRATION OF NPL-BASED 'REVERSE SENSING' VARNISHES	66
2.3	CONCLUSIONS	68
<u>CHAPTER 3: SINGLE-PARTICLE RATIOMETRIC PRESSURE SENSITIVE PAINTS BASED ON 'DOUBLE-SENSOR' COLLOIDAL NANOCRYSTALS</u>		69
	OVERVIEW	69
3.1	INTRODUCTION	71
3.2	RESULTS AND DISCUSSION	77
3.2.1	OPTICAL PROPERTIES AND TEMPERATURE SENSITIVITY OF DIB-NCs	77
3.2.2	RATIOMETRIC OXYGEN SENSING USING DIB NCs	82
3.2.3	EFFECT OF TUNING THE CORE AND SHELL RELATIVE SIZES	95
3.2.4	SINGLE PARTICLE RATIOMETRIC OXYGEN SENSING USING DIB NCs	106
3.2.5	PHOTOPHYSICAL MECHANISMS OF THE DOUBLE SENSING RESPONSE	107
3.2.6	RATIOMETRIC SENSING RESPONSE WITH DIFFERENT GASES AND PRESSURE	112
3.2.7	COMPARISON BETWEEN O ₂ SENSING AND SPECTROELECTROCHEMISTRY	115
3.3	CONCLUSIONS	119
<u>CONCLUSIONS</u>		121
<u>REFERENCES</u>		124

Introduction

A surface constitutes a simplified type of interface, which can be defined as a small number of atomic layers that separate two solids in contact with one another, whose properties significantly differs from those of the bulk material they separate. In case of a surface, the solid is in contact either with the surrounding media or the vacuum.

The development of a solid theoretic background for the description of the surface electronic structure of materials has been pivotal in modern nanoscience and nanotechnology. While the study of surfaces and interfaces originated as a branch of condensed matter research, it rapidly grew first into a fundamental subject in physical chemistry, for the study of surface reactions and catalysis, and later in several other disciplines, such as micro- and nano-electronics, micro- and nano-fluidics, coatings, chemo- and bio-sensing, pressure sensing and, most importantly for this thesis, nanostructured materials¹⁻⁴.

While surfaces in bulk materials have been extensively explored and can give useful information about the material itself, they still represent a minor perturbation which does not affect the bulk properties. This is not true if we decrease the material size down to the nanoscale: excitons in nanocrystals (NCs) are confined in a volume whose size is comparable to their Bohr-exciton radius, thus making the carriers wave functions efficient probes of the surfaces^{2, 5, 6} and of surface-related imperfections.

By definition, surface atoms are missing at least one of their neighbors, which results in the formation of danglind bonds. Such undercoordinated atoms contribute to a set of electronic states whose energies lie within the energy gap of the material, rather than being resonant with either the valence or conduction band¹. These states lie within the family of extrinsic defects, in opposition to intrinsic ones that describe surface states originating from the interruption of a perfectly cleaved surface³. Extrinsic states are not limited to unpassivated dangling bonds: such defects as vacancies and adsorbate (also called surface ligands) belong to this class¹.

A lot of work has been dedicated to the active role of surface ligands: not only do they ensure good solubility to the NCs⁷, but they also provide a passivation of the uncoordinated surface atoms^{1,7} and, importantly for applicative purposes, they offer an extremely versatile platform to tune several properties of NCs, such as the bandgap, the ionization potential, electron affinity, the PL efficiency by strategically designing and implementing ligands with proper HOMO and LUMO values¹.

However, a thorough choice does not guarantee a complete passivation. Especially with smaller NCs, the steric hindrance between passivating ligands could be non-negligible^{5, 8, 9, 10}. As a result, some uncoordinated atoms become active surface defects that can directly affect the NCs properties. If a photogenerated carrier (either electron or hole) is captured by such surface defect, it suddenly becomes unavailable for the radiative recombination from the band edge of the NC, thus lowering its PL efficiency.

The first observations of this phenomenon led to a great deal of research over the past decades that was dedicated to minimize the surface defects and therefore their undesirable effects that limited their applications¹¹, reduce PL^{12, 13} and hinder transport¹⁴. The most renowned and successful strategy to overcome this issue is the passivation of the NC surface with a thin shell of a larger bandgap semiconductor, thus providing good passivation of the surface traps and therefore ensuring better optical performances¹.

Without a proper passivation, the uncoordinated sites act as efficient traps for either electrons or holes^{1, 5, 7}; following the capture of a carrier, the highly delocalized exciton state is converted into a trap state which is localized at the surface, a process that was described within the semiclassical Marcus electron transfer theory^{7, 15, 16}. Several models have been proposed to explain how the surface states affect the radiative band-edge PL. Trapped carriers are typically regarded as forming dark excitons, although the presence of a surface implicates a lowering of the symmetry of surface states, which gives rise to a non-negligible surface-induced mixing of forbidden and allowed excitonic states, as inferred from the decay rates of both dark and bright excitons^{16, 17}.

While the first studies on cadmium selenide (CdSe) NCs, regarded as a model system for semiconductor NCs, used to neglect the existence of any radiative

contribute from the defects state, recent works have thoroughly investigate the red-shifted emission with respect to the band-edge PL that can be observed in unpassivated CdSe NCs^{7, 16, 18, 19}. This additional emission has been ascribed to either shallow or deep traps, which are distinguished by different decay rates due to the fact that carriers in shallow trap can easily delocalize again and contribute to band-edge emission, while for deep traps the detrapping processes is hardly accessible even at room temperature¹⁶. Such defect-related, red-shifted PL has been widely investigated as well as exploited for white-light emission^{20, 21}, sensing²² and temperature measurements applications²³.

Despite the broad investigation on the defect-related emission, however, at the beginning of my PhD research little to no work had been dedicated to the effect of surface traps on the band-edge emission of NCs. As I report in this thesis for different NCs, tuning the population of the surface defects indeed affects the intrinsic radiative processes of the NCs.

To this aim, I setup for the first time in our laboratory spectroelectrochemistry (SEC) measurements and spectroscopic experiments under controlled atmosphere: the combination of these techniques rapidly became a powerful tool to study the PL emission of colloidal NCs while changing their environment, and therefore to assess the defect-mediated effect of the oxidative/reductive surroundings on their PL efficiency.

Spectroelectrochemistry experiments have been carried out by coupling a fundamental spectroscopic analysis with an electrochemical cell and a potentiostat. The electrochemical cell configuration that best suited my purposes is the three-electrode setup: current flows between a working electrode (WE) and a counter electrode (CE), whereas the presence of a reference electrode (RE) kept at a fixed electrochemical (EC) potential allows for measuring the potential difference between the WE and the RE itself. As a result, it is possible to precisely monitor the EC potential variation that the WE undergoes when an electrochemical reaction is taking place. The CE and RE are standard platinum and silver electrodes, respectively, whereas the WE consists of a transparent, ITO-covered quartz substrate onto which I deposit the NCs. The electrodes are placed into a quartz cuvette filled with the electrolyte (a solution of tetrabutylammonium

perchlorate, TBAClO₄, in propylene carbonate). At the beginning of the experiment, before any perturbation is applied to the system through the potentiostat, the WE is in electrochemical equilibrium, and its EC potential is measured with respect to the RE EC potential. When current starts flowing between WE and CE, a voltmeter monitors the new EC potential values at the WE with respect to the RE. The use of a transparent cell and WE allows me to optically excite the NCs layer deposited onto the WE and record their PL intensity with either a charge-coupled device or a time-resolved PL setup.

According to the change in the EC potential that the NCs are undergoing, their luminescence displays a consistent variation, which result from the change in the occupancy of the surface defects states. Such defects as dangling bonds can act as a trap for either electrons or holes; when a negative potential is applied to the WE, electrons flow to the electrode and therefore to the NCs, thus raising their Fermi energy and gradually filling the surface defects with electrons. As a result, the population of surface defects that can capture a photogenerated electron decreases, whereas the hole trapping capability of the surface states is enhanced. The PL intensity is therefore determined by the competition between the quenching effect caused by an increased hole withdrawal and the brightening effect prompted by the suppressed electron trapping, and ultimately depends on whether the electron or hole trapping rate is dominant in a particular type of nanocrystals.

The opposite description holds for the application of a positive EC potential: here, electrons are removed from the NCs and their Fermi energy decreases. This allows me to artificially expose the materials to an excess of electron poor agents with respect to the atmospheric condition and thereby to monitor the PL response to a severe oxidative environment. These conditions correspond to the progressive lowering of the Fermi level in the NCs, which activates electron traps and concomitantly suppresses hole trapping by depleting surfaces states of excess electrons. Again, the dominant process between electrons and holes capturing by surface states determines the change in the PL intensity.

Once monitored via the SEC experiments, the PL brightening/dimming can be modelled and related to the band gap structure of the material, which leads to a thorough understanding of the material's behaviour under reductive or oxidating environment.

This knowledge allows me to implement their use as active materials in optical oxygen pressure sensors, also called Pressure Sensitive Paints (PSPs)^{24, 25}.

PSPs are optical sensing coatings that enable the visualisation of the oxygen pressure in the proximity of complex or miniaturized surfaces and in structures with moving parts²⁶⁻²⁸. Besides their established use in aerodynamics tests²⁹⁻³², they have been recently employed in a variety of analysis such as ballistic studies³³, cavity acoustics³⁴⁻³⁷, adiabatic film cooling effectiveness^{38, 39}, and microchannel fluidics⁴⁰⁻⁴².

PSPs typically consist in a porous^{43, 44} or polymeric^{45, 46} binder containing a chromophore, which typically belongs to one of these three classes of organic dyes: porphyrins⁴⁶⁻⁴⁸, pyrenes^{49, 50} or ruthenium complexes^{51, 52}. Their working principle relies on the one-on-one interaction between a photoexcited chromophore and an O₂ molecule that, in its ground state, is a diradical triplet with strong electron-acceptor character. This results in rapid energy/charge transfer from the chromophore to molecular oxygen, resulting in a strong quenching of the chromophore emission^{28, 31, 53}.

Recently, great attention has been dedicated to the potential use of inorganic colloidal NCs as optical sensors, since their combination of color-tunability^{54, 55}, photostability⁵⁶, high quantum yields⁵⁷⁻⁵⁹ and exceptionally large surface-to-volume ratios^{24, 60} makes them ideal platforms to sense both specific molecules in biological environments⁶¹⁻⁶⁵ and dry or wet gases^{24, 66-69}.

Here, in the first Chapter of this work I propose a potential all-inorganic alternative to traditional dyes by employing cesium lead bromide (CsPbBr₃) perovskite NCs. Such materials have lately been the focus of intense research, mostly thanks to their exceptional optical properties^{70, 71} as well as their intrinsic resilience to structural imperfections, also known as defect tolerance⁷². I present the results of SEC experiments, which I conducted side-by-side to optical oxygen sensing measurements; both show the dominant role played by hole traps in affecting the NCs radiative recombination. Understanding and modeling their

behavior allow me to realize an all-inorganic alternative to traditional organic oxygen pressure sensors, based on the increase of their PL intensity under reduced oxygen pressure.

Traditional PSPs chromophores, however, together with perovskite NCs, rely on the disappearance of the signal in presence of oxygen, which means it may not represent the best approach when high oxygen concentrations (for instance, at atmospheric pressure) need to be detected. In Chapter 2, I demonstrated how to overcome this issue by realizing a novel-concept, inorganic 'reverse' PSP, with CdSe nanoplatelets (NPLs) as active material, since their PL intensity increases with the oxygen concentration. NPLs are strongly anisotropic systems which recently gained a lot of attention⁷³ and exhibit narrow emission spectra, giant oscillator strength^{74,75}, and suppressed Auger recombination^{75,76}, as well as an exceptionally large surface/volume ratio which makes them particularly vulnerable to nonradiative carrier trapping into surface defects. SEC experiments and optical measurements under controlled atmosphere allow me to unveil and model the unusual benefit of an oxidative environment on CdSe NPLs, which are mainly affected by hole trapping.

Although exhibiting the peculiar advantage of an increase signal in presence of oxygen, the PSPs based on CdSe NPLs share with the perovskite-based sensors the major drawback of providing a radiometric oxygen detection only, that is, the measurement solely relies on a change in the PL intensity of the chromophore. The PL, however, can also change as a result of a temperature variation or UV-induced degradation. In order to overcome this issue, in Chapter 3 I introduce a significant improvement by employing dual-emitting, core/shell cadmium selenide/cadmium sulfide (CdSe/CdS) NCs that consist of a small CdSe core overcoated with an ultra-thick CdS shell^{77, 78}. Owing to their peculiar internal structure, these NCs are capable of simultaneously sustaining core and shell excitons, whose radiative recombination leads to two-colour (red and green) luminescence under both low-fluence continuous wave (cw) optical excitation⁷⁸ and electrical injection⁷⁷. Importantly for PSP applications, the shell excitons are exposed to NC surface species, and their luminescence is highly sensitive to nonradiative electron transfer to surface defects or molecular acceptors (such as molecular oxygen) adsorbed onto the NC surface that lead to luminescence

quenching⁷⁹. In stark contrast, the emission arising from core-localized excitons is enhanced by exposure to O₂ as the removal of extra electrons generated by photocharging would quench nonradiative Auger recombination.⁷⁹ As a result of these effects, the two emission channels of the DiB NCs follow opposite trends with increasing/decreasing O₂ partial pressure, which allows me to achieve a 'double-sensor' ratiometric response, as well as suppressed cross-readout due to a zero overlap between the luminescence spectra of the two emissive states, a dynamic range of ratiometric O₂-pressure sensing of three orders of magnitude, and the temperature-independent ratiometric response between 0°C and 70°C.

Chapter 1

Effect of nonradiative defects and environmental oxygen on exciton recombination processes in CsPbBr₃ perovskite nanocrystals

This work was performed in collaboration with the Italian Institute of Technology (IIT, Genova).

Overview

Lead halide perovskite nanocrystals (NCs) are emerging as optically active materials for solution-processed optoelectronic devices. Despite their technological relevance and intrinsic resilience to structural imperfections, no in-depth study of the role of selective carrier trapping and environmental conditions on their exciton dynamics has been reported to date. In this chapter, I conduct spectro-electrochemical experiments, side-by-side to optical oxygen sensing measurements on CsPbBr₃ NCs and show the strong (60%) PL quenching under reductive potentials by trapping of photogenerated holes, with oxidizing conditions resulting in minor (5%) brightening due to suppressed hole trapping, which indicates that electron accepting states play a minor role in nonradiative exciton decay. This behaviour is rationalized through a semi-quantitative model that links the occupancy of trap sites with the position of the NC Fermi level controlled by the EC potential. PL measurements in controlled atmosphere reveal strong quenching by collisional interactions between the NCs and O₂, in contrast to the photo-brightening effect observed in perovskite films and single crystals. This indicates that O₂ acts as an efficient scavenger of photo-excited electrons without mediation by structural defects and, together with the asymmetrical SEC response, suggest that, despite the higher surface-to-volume ratio, electron rich surface defects are likely less abundant in nanostructured perovskites, leading to an emission response dominated by direct interaction with the environment.

1.1 Introduction

Lead halide perovskites are attracting growing attention as optically active materials in numerous photonics technologies⁸⁰, including high performance solar cells⁸¹⁻⁸⁶, light emitting diodes (LEDs)^{87, 88}, lasers^{71, 89, 90} and radiation- and photo-detectors^{91, 92}. Recently, colloidal synthesis routes have been developed to obtain perovskite nanocrystals (NCs) in the hybrid organic-inorganic formulation MAPbX₃ (MA=CH₃NH₃)^{93, 94}, as well as in the all-inorganic cesium lead halide perovskite form, CsPbX₃ (X = Cl, Br, or I)^{70, 95-97}, which have been demonstrated in a variety of shapes including nanocubes⁷⁰, nanoplatelets^{96, 98}, nanosheets⁹⁹ and nanowires⁹⁴. Notably, the electronic structure and the deriving optical properties of perovskite NCs are tuneable both via control of the particle size and shape (*quantum confinement effect*)^{93, 96, 98} and through halide substitution via post-synthesis anion-exchange reactions^{70, 95}, which allow for achieving full coverage of the visible spectrum ideally suitable for wide gamut displays with ultra-high color saturation^{70, 71}. For these reasons, numerous studies have recently been dedicated to the post-synthesis manipulation and assembly¹⁰⁰⁻¹⁰⁴ of perovskite NCs, as well as to spectroscopic and device aspects including single photon emission¹⁰⁵⁻¹⁰⁹, exciton¹¹⁰ and bi-exciton¹¹¹ photophysics, optical gain and lasing¹¹²⁻¹¹⁶, LEDs^{80, 117-122} and solar cells^{123, 124}. Doping of perovskite NCs with transition metal cations such as manganese¹²⁵⁻¹²⁷, cadmium, zinc, tin¹²⁸ and bismuth¹²⁹ has also been reported, resulting in widely Stokes-shifted emission from localized intragap dopant states sensitized by the NC host as well as lead-free metal-halide perovskite NCs which are technologically relevant due to toxicity concerns generated from lead-based materials¹³⁰.

A further beneficial aspect of perovskite materials is the high tolerance of their transport and photophysical properties to structural disorder, such as point defects (i.e. vacancies^{131, 132}, ionic rotations¹³³⁻¹³⁸), high ionic mobility^{135, 139} and electronic impurities¹⁴⁰, which coexist with high carrier mobilities and large diffusion lengths exhibited by both films¹⁴¹ and NCs¹⁴². This distinctive characteristics arises from their peculiar hybridized *s-p* antibonding valence band structure and strong spin-orbit coupling resulting in localized electronic states associated to structural defects to be positioned in energy inside the electronic bands or nearly resonant to their band edges¹⁴³⁻¹⁴⁶, rather than forming deep

intragap states that in II-VI, III-V or V-VI NCs are typically responsible for carrier trapping and nonradiative emission quenching^{25, 147-151}. As a result, both hybrid and all-inorganic perovskite NCs exhibit highly efficient narrowband photoluminescence (PL)^{25, 150, 152-155} without the need for electronic passivation with wider-gap shells¹⁴⁴ commonly used to enhance the emission quantum yield of metal chalcogenides NCs, and are typically less affected by photo-oxidation¹⁴⁴. Nevertheless, recent studies showed that the PL and transport of both MAPbX₃ and CsPbX₃ perovskite films and single crystals is strongly affected by the environmental conditions¹⁵⁶⁻¹⁵⁹, leaving the role of surface defects and direct interaction with the chemical surroundings an open subject of research. Specifically, the emission efficiency was consistently observed to increase in oxygen atmosphere (both dry and humid) with respect to inert environment (vacuum or inert gasses) due to passivation of photo-induced intragap states by O₂. A similar PL brightening effect has been found also in metal chalcogenide nanostructures such as CdSe nanoplatelets¹⁵⁰ and core/shell CdSe/CdS NCs²⁵, whose emission efficiency is enhanced by molecular oxygen that, being a diradical triplet with strong electron accepting character, depletes defect states on the particle surfaces from excess electrons responsible for ultrafast nonradiative trapping of photo-excited holes in vacuum conditions^{25, 150, 160, 161}. Despite the fundamental and technological relevance of tracing rational design guidelines for optimizing the optical properties of perovskite nanostructures beyond what is already available by exploiting their intrinsic resilience to structural imperfections, no in-depth study of the role of selective carrier trapping and environmental conditions on their exciton dynamics has been reported to date.

Here, in order to investigate the nature and the effects of trap states, as well as the role of the environment in the exciton recombination process in perovskite NCs, we conduct, for the first time, spectro-electrochemical (SEC) experiments on CsPbBr₃ NCs, side-by-side to optical oxygen sensing measurements. We show that, by externally tuning the position of the Fermi level through the application of an EC potential (V_{EC}), we alter the occupancy of defect states and thereby control the NC's emission intensity without degrading the NCs. Specifically, our data shows that the PL efficiency is strongly quenched upon the application of a negative (reductive) V_{EC} , which corresponds to raising the Fermi level in the NC, indicating that, consistently with bulk and thin film perovskites^{156-159, 162}, the

emission mechanism is mostly affected by trapping of photogenerated holes, whereas electron trapping plays a negligible role in nonradiative PL quenching. Accordingly, upon the application of a positive (oxidative) V_{EC} , corresponding to lowering the Fermi level in the NCs, the PL intensity increases slightly due to suppressed hole trapping in defect states depleted of excess electrons, despite the fact that oxidative conditions might concomitantly lead to the activation of electron acceptor states. The quantitative difference between the PL responses upon raising or lowering the Fermi level in the NCs, together with the relatively high PL quantum efficiency at zero EC potential ($\Phi_{PL}=30\pm 4\%$) suggest that the number of *active* intragap hole traps per NC in unperturbed conditions ($V_{EC}=0V$) is arguably very small, in agreement with the high defect tolerance of perovskite materials¹³¹⁻¹³⁹. This behaviour is rationalized through a semi-quantitative model that links the occupancy of trap sites to the position of the NC Fermi level. The model shows that trap sites, in the absence of EC potentials, are likely positioned in energy slightly above the Fermi level (that is, they are devoid of electrons) and their filling under negative V_{EC} leads to progressive PL quenching due to activated nonradiative hole trapping. Photoluminescence measurements in controlled oxygen atmosphere complement and extend the picture emerging from the SEC experiments and enable us to elucidate the role the NC environment on the exciton recombination dynamics. Specifically, these measurements reveal a strong effect of collisional interactions between the NCs and molecular oxygen that acts as an efficient scavenger of photogenerated electrons directly from the NC conduction band without mediation by structural defects. The removal of O_2 from the NC environment leads to nearly instantaneous and fully reversible $\sim 30\%$ brightening of the PL efficiency with respect to oxygen atmosphere. This behaviour indicates that the interaction mechanism between perovskite nanostructures and molecular oxygen is markedly different from the process leading to the persistent emission brightening upon O_2 exposure observed in perovskites films and single crystals¹⁵⁶⁻¹⁵⁸, which was ascribed to saturation of photogenerated intragap states by adsorption of O_2 molecules on the sample surface. In perovskite NCs, conversely, the PL quenching by O_2 , together with the weak brightening effect of oxidative EC potentials, suggests that molecular oxygen extracts photogenerated electrons directly from the NC conduction band, without the need for mediation by surface sites and further corroborates the picture that

the number of electron-rich surface states acting as hole traps in unperturbed atmospheric conditions is likely smaller than in film or bulk materials.

1.2 Results and Discussion

1.2.1 Structural and optical properties of CsPbBr₃ nanocrystals

CsPbBr₃ NCs with a schematic crystal structure depicted in Figure 1.1a were synthesized following the procedure of Protesescu *et al.*⁹⁵ by Dr Akkerman and Dr Accornero from the group of Prof. Manna at the Italian institute of Technology (IIT, Genova). Dr Prato, also from the IIT group, provided us with the transmission electron microscopy images and X-ray diffraction (XRD) measurements. The TEM image and respective size histogram reported in Figure 1.1b and 1c show particles with cubic morphology and average side length, $L = 9.6 \pm 1.2$ nm. The powder XRD pattern in Figure 1.1d confirms the orthorhombic structure of the NCs, matching with previous reports¹⁶³.

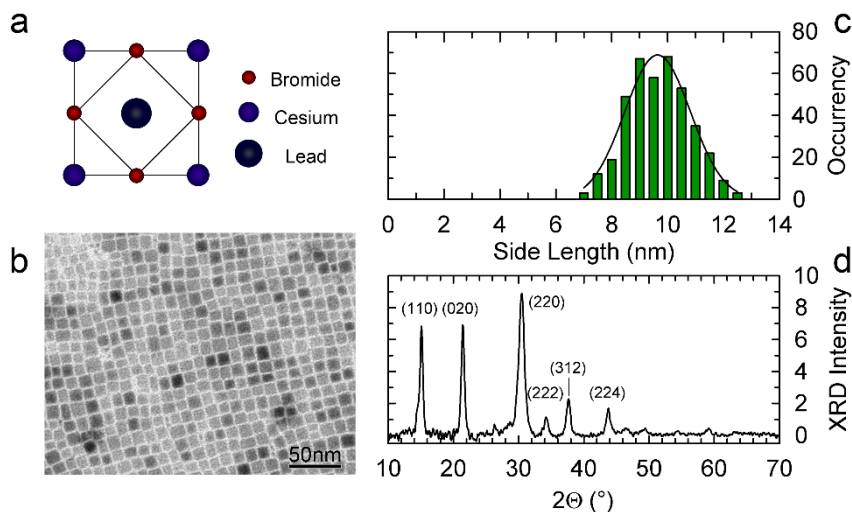


Figure 1.1. **Structural characterization of CsPbBr₃ perovskites NCs.** (a) Schematic of the crystal structure of CsPbBr₃ perovskites. The relative sizes are adjusted proportionally to the ionic radii of each ion (Br⁻: 196 pm¹⁶⁴, Cs⁺: 167 pm¹⁶⁴, Pb²⁺: 120 pm¹⁶⁵). (b) Transmission electron micrograph of CsPbBr₃ perovskite NCs and (c) related size histogram extracted from the analysis of over

300 particles, showing cubic NCs with average side length of 9 ± 1 nm. (d) X-ray diffraction pattern of CsPbBr₃ perovskite NCs at room temperature.

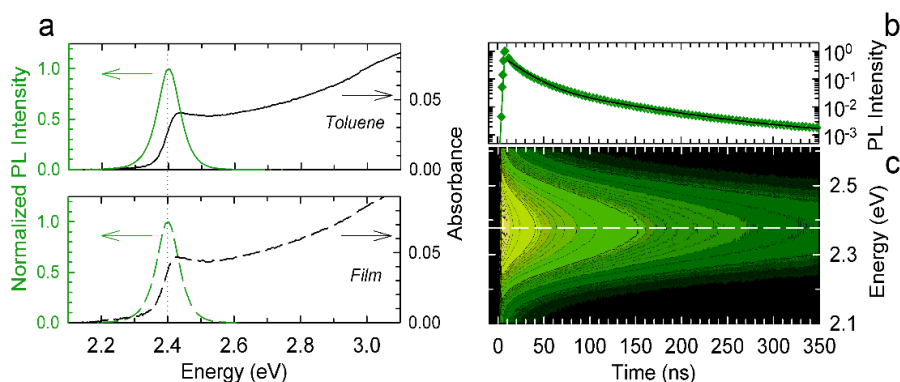


Figure 1.2. **Optical characterization of CsPbBr₃ perovskites NCs.** (a) Optical absorption (black lines) and photoluminescence (PL, green lines) spectra of the NCs in toluene solution (top panel, solid lines) and deposited onto a silica substrate (bottom panel, dashed lines) under 3.1 eV excitation (excitation fluence 100 nJ/cm²). (b) PL time decay curves measured at the PL maximum (2.43 eV) for the NCs in toluene (green diamonds) and in solid film (light green circles) and corresponding double-exponential fitting curve (black solid and black dashed lines for the solution and the film respectively, the curves are shifted vertically for clarity). (c) Contour plot of the PL time decay as a function of the emission energy for the NC film showing no spectral diffusion due to inter-dot energy transfer. The dashed white line is a guide for the eye to emphasize the invariance of the PL peak position over time. All measurements are conducted using 3.1 eV excitation with fluence of 100 nJ/cm².

The optical absorption and the PL spectra of the CsPbBr₃ NCs in toluene solution and dip-casted onto silica are reported in Figure 1.2a, showing identical spectral properties for the two systems with the characteristic steep absorption edge of perovskite NCs with first excitonic feature at 2.43 eV and narrow-band emission peak at 2.4 eV. The PL quantum yield is $\Phi_{\text{PL}}=34 \pm 4\%$ in solution and $\Phi_{\text{PL}}=30 \pm 4\%$ in solid film. Consistently, the PL decay curves collected at the emission maximum (Figure 1.2b) show identical decay dynamics in both solution and solid film. In agreement with previous reports^{70, 105}, the decay dynamics follows a double-exponential trend with a fast decay ($\tau \sim 13$ ns) responsible for

~80% of the signal followed by a longer-lived component with $\tau \sim 69$ ns accounting for the remaining ~20%. Notably, consistently with recent results by Rainò et al.¹⁰⁷, the spectrally resolved contour plot of the PL decay of the NC film in Figure 1.2c shows no shift of the emission profile over time, indicating that spectral diffusion due to dot-to-dot energy transfer in the film is negligible, despite the fact that the NCs are not coated with a wide band-gap shell that has been used to suppress inter-dot energy transfer in close packed films of chalcogenide NCs^{59, 166}.

1.2.2 Spectro-electrochemistry experiments

In order to investigate the effects of carrier trapping in intragap defects on the photophysics of CsPbBr₃ NCs, we conducted SEC measurements using the custom experimental setup illustrated in Figure 1.3a, consisting of an ITO-coated quartz substrate covered by a film of sintered ZnO particles (~50 nm diameter) and a thin layer of CsPbBr₃ NCs as the working electrode and silver and platinum wires as reference and counter electrodes, respectively. Figure 1.3a also shows a schematic band structure of the perovskite NCs with the valence band maximum (VBm) consisting of antibonding orbitals formed by *s*-orbitals of Pb and *p*-orbitals of Br and the conduction band minimum (CBm) originating from a charge transfer between *p*-orbitals of Pb and *p*-orbitals of Br, with the former providing the dominant character to the resulting orbital^{143, 167, 168}. In unperturbed conditions, the NC Fermi level (FL) is placed at the center of the energy gap, as expected for undoped semiconductors. The intragap trap states (TS) responsible for the SEC behavior are placed in energy slightly above it, according to the semi-quantitative model of the EC response described later in this section. We first apply a negative V_{EC} , which corresponds to raising the Fermi energy in the NC film, leading to progressive passivation (activation) of electron (hole) traps. In these conditions, the NC emission intensity is thus determined by the competition between the quenching effect of hole withdrawal and the brightening effect of suppressed electron trapping.

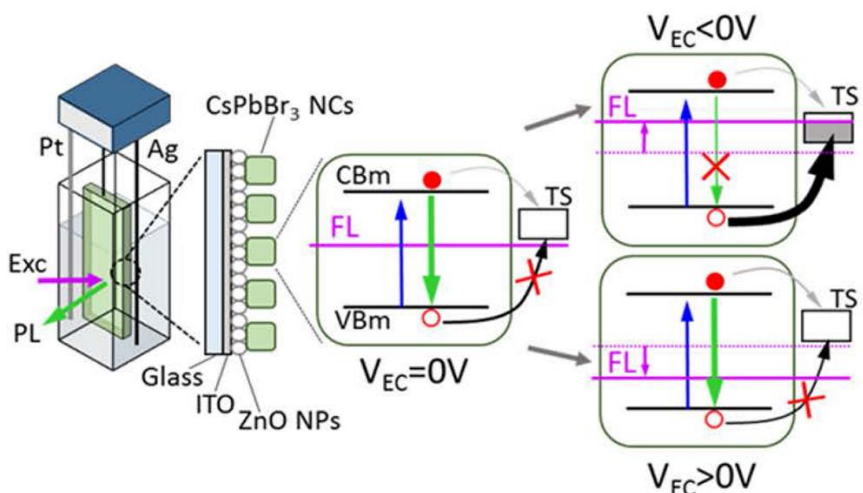


Figure 1.3. **Schematics of the SEC setup and illustration of the possible processes under EC potential.** (a) Schematics of the SEC setup consisting of an EC cell with tetra butyl ammonium perchlorate in propylene carbonate (0.1M) as an electrolyte and a working electrode comprising an ITO-coated glass covered with a layer of ZnO nanoparticles (NPs) and CsPbBr₃ perovskite NCs. The figure also illustrates the radiative recombination pathway (green arrow) of photo-excited band-edge excitons and the competitive carrier trapping processes in trap states (TS). The effect of the EC potential on the PL intensity depends on the filling/emptying of trap states (right of the band diagram) in response to changes in the position of the Fermi level (FL; pink line).

In Figure 1.4a we report the complete set of PL spectra of the NCs under application of a negative V_{EC} potential scanned from 0 V to -2.5 V and then back to 0 V (100 mV potential steps lasting 10 seconds each). To quantify the effect of the EC potential on the PL intensity, in Figure 1.4b we plot the integrated PL intensity as a function of V_{EC} normalized to its value at $V_{EC} = 0$ V. The measurement is repeated twice so as to assess the reversibility of the PL response and the absence of significant degradation effects. The weak $\sim 10\%$ PL drop, uncorrelated to the EC sweep, occurring during the whole measurement (~ 13 minutes in total) is ascribed to the dissolution of a minor population of NCs by the propylene carbonate solution.

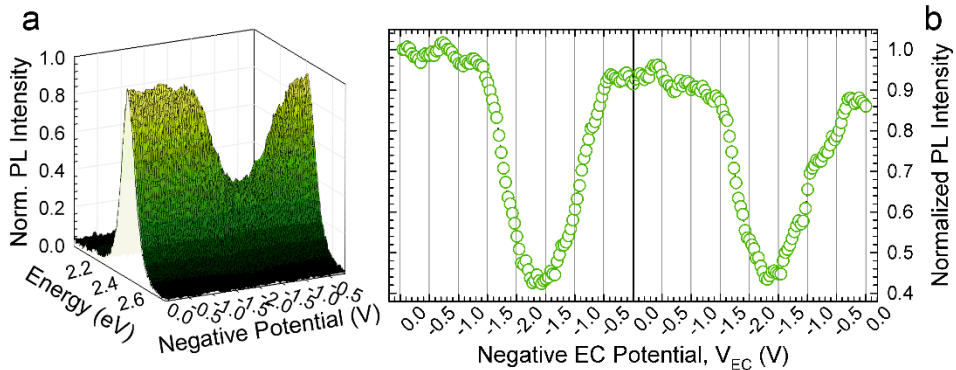


Figure 1.4. **CsPbBr₃ perovskite NCs under a negative EC potential.** (a) A series of PL spectra (0.5 s acquisition time per frame, 10 s steps) for a stepwise scan of the EC potential to negative values (100 mV steps each lasting 10s). (b) Spectrally integrated PL intensity as a function of V_{EC} extracted from the spectra in 'b'. Two sequential SEC scans are reported in order to show the repeatability of the measurement. The initial intensity is normalized to its value at $V_{EC} = 0$ V. All measurements are conducted using 3.1 eV excitation with fluence of 100 nJ/cm².

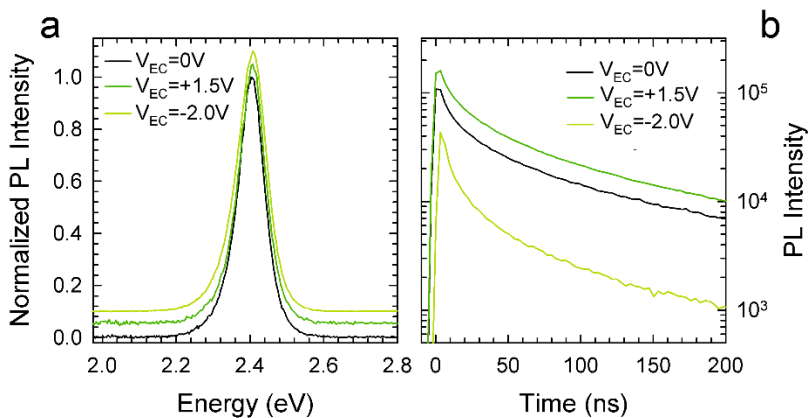


Figure 1.5. **Spectrally-resolved and time-resolved PL emission of a sample of CsPbBr₃ perovskite NCs under negative and positive EC potential.** (a) Normalized PL spectra at $V_{EC} = 0$ (black line) and $V_{EC} = -2$ V (light green line) and $V_{EC} = +1.5$ V (green line). The spectra are shifted vertically for clarity. (b) PL decay curves at $V_{EC} = 0$ V, -2 V and $+1.5$ V. The color code is the same as in 'a'. All measurements are conducted using 3.1 eV excitation with fluence of 100 nJ/cm².

Accordingly, $\sim 10\%$ decrease in the optical absorbance is observed for an equivalent amount of time without the application of an EC potential (as shown in Figure 1.6).

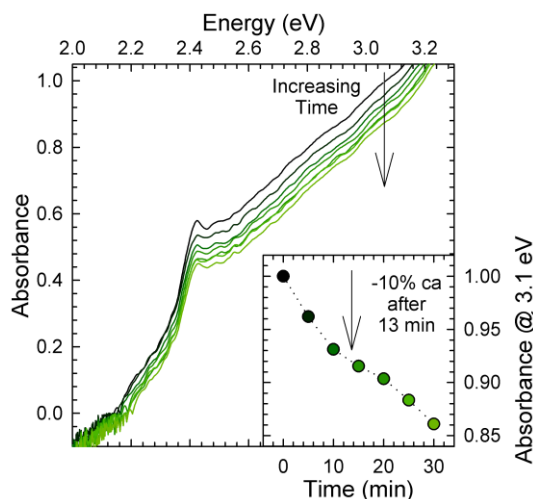


Figure 1.6. **Absorption spectra of a thin film of CsPbBr₃ NCs in the electrolyte solution over time.** Optical absorption spectra of a submonolayer film of CsPbBr₃ NCs deposited onto an ITO-coated glass covered with a layer of ZnO nanoparticles (NPs), immersed in the electrolyte solution used for the spectro-electrochemical experiments (tetrabutylammonium perchlorate, 0.1 M in propylene carbonate). The first spectrum is measured 5 seconds after the addition of the electrolyte (black line) and subsequent measurements are performed every 5 minutes (increasingly lighter green lines) up to a total time of 30 minutes, in order to cover the SEC data collection time span (13 minutes and 30 seconds for 2 cycles under negative EC potential and 10 minutes for 2 cycles under positive EC potential.) The inset shows the optical absorbance values at 3.1 eV, corresponding to the excitation energy used for the SEC experiments, extracted from the absorbance spectra and reported as a function of time.

In the initial stage of each potential ramp (up to $V_{EC} = -1.5$ V) no noticeable change in PL intensity occurs. This is common in SEC measurements on colloidal nanostructures using ITO/ZnO substrates^{150, 169-171} and is due to the combined effect of the NC coating by dielectric organic ligands and of the potential drop across the ZnO layer¹⁷² necessary to suppress PL quenching by energy- or charge-transfer from the NCs to the ITO^{171, 173}. Accordingly, the current-voltage response

during the SEC experiments reported in Fig.S2 shows an injection threshold at $\sim 1\text{V}$. At negative potentials above $|V_{\text{EC}}| > 1.5\text{V}$, the PL undergoes strong quenching, reaching 60% drop of the initial emission intensity at $V_{\text{EC}} = -2\text{V}$. When returning back to zero EC potential, for both cycles we observe almost complete recovery of the respective initial PL intensity, indicating that the potential sweeps cause no significant chemical degradation of the NCs nor permanent modifications of their surface structure. This is confirmed by the inspection of the PL spectrum collected for different V_{EC} -values (Figure 1.5a) that shows identical emission profiles in all EC conditions. The SEC results indicate that the PL intensity trends are to be ascribed to reversible EC activation/passivation of traps sites likely associated to under-coordinated atoms or dangling bonds. Specifically, since raising the NC Fermi level under negative V_{EC} suppresses electron trapping and concomitantly activates hole traps, the observed strong drop of the PL intensity suggests that the dominant nonradiative process in our NCs is trapping of photogenerated holes, whose quenching effect on the PL efficiency is not counter balanced by the concomitant suppression of electron trapping.

The minor role of electron trapping over hole trapping is confirmed by the SEC measurements under positive (oxidizing) EC potentials. These conditions correspond to the progressive lowering of the Fermi level in the NCs, which activates electron traps and concomitantly suppresses hole trapping by depleting surfaces states of excess electrons.

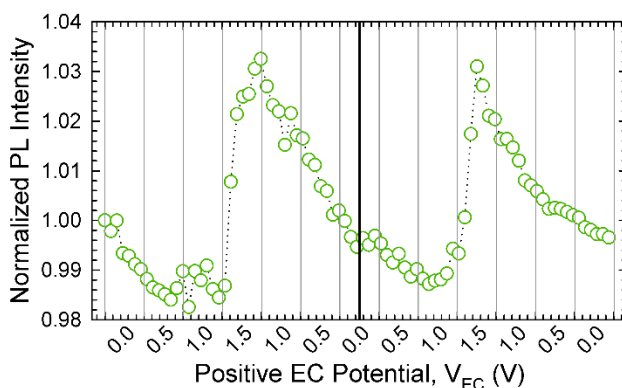


Figure 1.7. **CsPbBr₃ perovskite NCs under a positive EC potential.** Spectrally integrated PL intensity during a stepwise scan of the EC potential to positive values

(100mV steps each lasting 10s. Two potential scans are reported to show the repeatability of the measurement. The initial intensity is normalized to its value at $V_{EC} = 0$ V. All measurements are conducted using 3.1 eV excitation with fluence of 100 nJ/cm².

Figure 1.7 shows the integrated PL intensity of the same NC film as Figure 1.4b, recorded while changing the potential from $V_{EC} = 0$ V to $V_{EC} = +1.5$ V and back to zero (0.1V steps, 10 s per step). Also in this case, two consecutive cycles are performed to check the reproducibility of the SEC response. Same as for the negative potential ramps, for $V_{EC} < 1.5$ V, we observe no significant modification of the PL intensity except for a very weak (<1%) photo-bleaching. More importantly, at $V_{EC} = +1.5$ V, the trend reverses and the PL intensity increases sharply, reaching 5% enhancement with respect to its value at $V_{EC} = 0$ V. For each cycle, when sweeping the potential back to 0 V, the PL intensity returns to its initial value, indicating no permanent oxidation of the NC's surfaces. Accordingly, the PL spectrum shows no shift in energy nor the emergence of additional spectral features (Fig.2d). Therefore, similarly to the PL dimming observed under negative EC potentials, the progressive and reversible brightening under positive potential is ascribed to the EC modulation of the occupancy of surface hole traps, whose capture rate for photogenerated holes strongly outcompetes electron trapping which likely requires to overcome a larger activation energy. The same argument explains the trend for negative potentials, where filling empty defect states (inactive hole traps) with electrons markedly quenches the PL despite the fact that electron withdrawal is concomitantly reduced. Time-resolved PL traces collected for $V_{EC}=0$ V, -2V and +1.5V (Figure 1.5b) show that the modulation of the emission intensity is due modifications of the early-time PL intensity, with essentially no effect on the decay dynamics. This indicates that nonradiative hole trapping is an ultrafast process occurring prior to radiative decay, which renders a portion of NCs in the ensemble non-emissive, while the residual PL is due to the radiative decay of the sub-population of 'bright' NCs with no active hole traps. We note that the quantitative difference between the quenching and the brightening effect under negative *versus* positive EC potentials suggests that, in the absence of an EC potential, the number of active hole traps per NC is arguably small, in agreement with the defect tolerance of perovskite materials and the relatively high PL quantum yield of our NCs ($\Phi_{PL}=30\%$). Accordingly, their passivation upon lowering

the Fermi level in the NCs leads to markedly weaker enhancement of the emission efficiency with respect to the strong PL quenching experience upon their activation under reductive EC potential. In both negative and positive EC potentials scans, we notice that the PL response under increasing $|V_{EC}|$ is measurably asymmetric with respect to the trend when the potential is swept back to 0V. This effect was also observed in ZnSe and CdSe colloidal nanostructures^{25, 169} and is ascribed to very long lifetime of trapped carriers (up to tens of seconds)¹⁷⁴ with respect to the rapid capture of band edge charges in active traps resulting in the hysteresis of the PL intensity over time.

Finally, to rationalize the SEC data, we propose a model that links the emission intensity (I_{PL}) to the occupancy of intra-gap hole traps that can be activated (passivated) by raising (lowering) the Fermi level through the application of an EC potential. The scheme of the decay channels determining the emission intensity is depicted in Figure 1.3a for both $V_{EC} < 0V$ and $V_{EC} > 0V$, where trap states (TS) are positioned slightly above the Fermi level in unperturbed conditions ($V_{EC} = 0V$). The application of negative potentials gradually fills TS with electrons, activating their hole trapping capability.

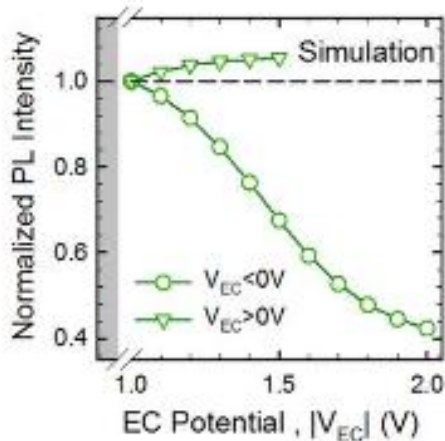


Figure 1.8. **Simulation of the optical response under negative and positive EC potential.** Simulated PL intensity vs V_{EC} for negative (circles) and positive (triangles) EC potentials. The simulation is run for $V_{EC} > 1$ to account for the potential step due to the ZnO interlayer.

On the other hand, lowering the FL at positive V_{EC} is nearly inconsequential to the PL intensity, a part for the suppression of residual hole trapping. Given the negligible effect on the emission intensity observed in the SEC experiments, in the model, we neglect electron trapping in order to keep the number of parameters reasonably low. To account for the effect of the EC potential on the occupancy of hole traps, we assume an average number of traps per NC, ρ_{TS} , and calculate the fraction of 'bright' NCs ($F_{\text{BRIGHT}} \propto I_{\text{PL}}$) as the probability of having no *active* hole traps assuming a Poisson distribution across the ensemble: $F_{\text{BRIGHT}} = e^{-\mu(V_{EC})}$. Here, the term $\mu(V_{EC}) = \rho_{TS} \cdot \frac{1}{e^{\frac{E_{TS} - (E_F - \gamma V_{EC})}{k_B T}} + 1}$ is the trap density multiplied by the trap occupation probability expressed by a Fermi-Dirac distribution where E_{TS} is the energy of the trap state and $(E_F - \gamma V_{EC})$ is the Fermi energy tuned by V_{EC} . The constant γ is an attenuation factor between the applied V_{EC} and the resulting shift of the Fermi level.

To illustrate the model, we calculate the EC response of our CsPbBr₃ NCs for a set of parameters reported in

Table 1 and considering the injection potential step introduced by the ZnO interlayer that prevents electrons to reach the NCs for $V_{EC} \leq \sim 1\text{V}$. The results of the simulations under both negative and positive V_{EC} are reported in Figure 1.8. In both cases, our semi-quantitative model reproduces the main experimental trends. Specifically, for $V_{EC} < 0\text{V}$, the progressive filling of trap states with electrons reduces the fraction of bright NCs in the ensemble, leading to 60% drop of the PL intensity.

On the other hand, the PL intensity is only slightly enhanced by the application of a positive EC potential, in agreement with the experimental data in Figure 1.7, corroborating the original scenario that in unperturbed conditions the availability of active hole traps is very small.

ρ_{TS}	1
E_F	-4.5 eV ($E_{CB}=-5.6\text{eV}$; $E_{VB}=-3.4\text{eV}$)
E_T	-4.43 eV
γ	0.13

Table 1. **Parameters used to reproduce the spectro-electrochemical trends.** We highlight that the trends in Figure 1.8 could be obtained also with other sets of γ , ρ_{TS} and E_T -values. Therefore, the parameters in

Table 1 have to be considered indicative and not univocal and serve the purpose of showing that the observed experimental response can be reproduced with the proposed model.

1.2.3 Oxygen sensing experiments

After having clarified the role of intragap defects in trapping photo-excited carriers in CsPbBr₃ perovskite NCs through SEC experiments, we now focus on the effect of the NC environment on the exciton recombination process. With this aim, we monitor the evolution of the PL intensity of a NC film deposited onto a glass substrate as a function of the O₂ pressure. In these experiments, the sample is kept in pure O₂ at P=1bar pressure for 90 seconds, after which the pressure is lowered by one order of magnitude at a time down to P=10⁻³ bar. For each step, the PL is monitored under constant excitation at 3.1 eV for 90 seconds. The ramp is then repeated while the chamber is progressively refilled with O₂ until 1 bar pressure is reestablished. The integrated PL intensity of the NC film during the pressure scan and corresponding Φ_{PL} -values are reported in Figure 1.9a, showing a step-wise PL enhancement with decreasing O₂ pressure reaching ~30% brightening at P=10⁻³ bar with respect to atmospheric conditions, with Φ_{PL} reaching ~40%. No modification of the spectral profile is observed at any pressure level (Figure 1.9b), which indicates that no permanent alteration of the NCs surfaces and/or stripping of the passivating ligands occurs during the pressure ramp. Accordingly, upon refilling the sample chamber with pure O₂, Φ_{PL} gradually recovers its initial value

at $P=1$ bar, indicating that the response is fully reversible and that the NCs are stable under continuous excitation for the whole duration of the measurement. The reproducibility of the PL response is further confirmed by data in Figure 1.10a, where we report five consecutive 90-seconds long ON/OFF pressure cycles between $P=1$ bar and $P=10^{-3}$ bar (total duration of the measurement 15 minutes).

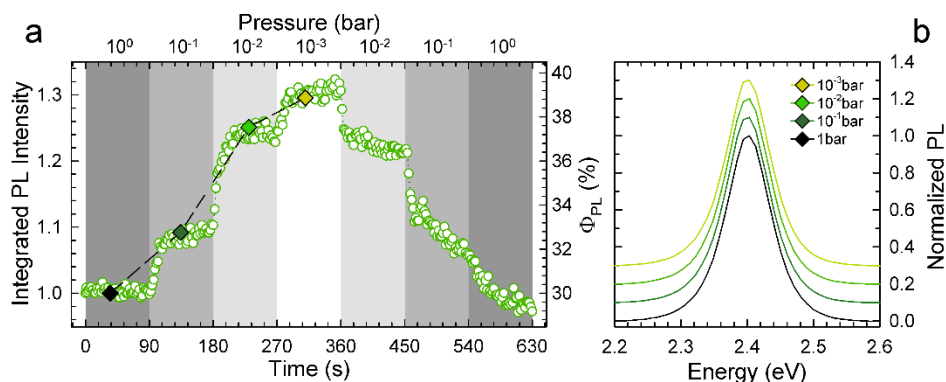


Figure 1.9. **CsPbBr₃ perovskite NCs PL under reduced oxygen pressure.** (a) Normalized spectrally integrated PL intensity and corresponding PL quantum yield, Φ_{PL} , of a CsPbBr₃ perovskite NCs film on silica during a stepwise pressure scan starting from $P=1$ bar and lowering the pressure one order of magnitude per step, down to $P=10^{-3}$ bar. The PL is monitored for 30 seconds at each pressure after which the chamber is refilled with pure O₂ following a reverse stepwise pressure ramp to $P=1$ bar. (b) Normalized PL intensity at each pressure level of Fig. 8a as indicated by the symbols. The spectra are shifted vertically for clarity. All measurements are conducted using 3.1 eV excitation with fluence of 100 nJ/cm².

The same measurement is performed also using humid air (20.5 g/kg, Figure 1.10a) showing the same PL response than pure O₂, thus confirming that the effect is due to direct interaction with O₂ with negligible role of water vapors. The long-term stability of the NCs in O₂ and 10⁻³ bar vacuum is finally assessed by data in Figure 1.10b, showing constant Φ_{PL} for one hour of continuous laser illumination at 3.1 eV. These results also corroborate our interpretation that the minor PL dimming observed in Figure 1.4b is a consequence of the electrolytic environment necessary for performing the SEC experiments. Notably, the PL response in both Figure 1.9a and Figure 1.10a follows almost instantaneously the step-like pressure change, which suggests that the increase of Φ_{PL} with decreasing O₂ pressure is due

to suppression of collisional physical interactions between the NC and oxygen molecules that, owing to their strong electron affinity, extract photogenerated electrons directly from the NC conduction band.

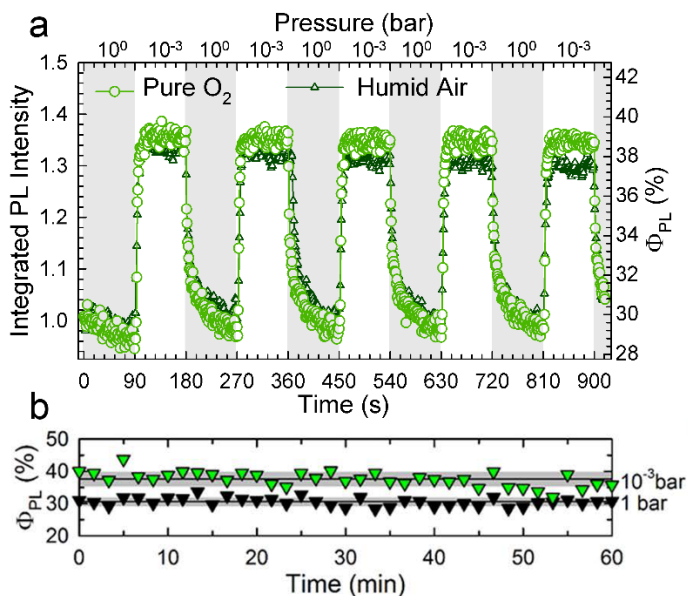


Figure 1.10. **Sensing and stability trends of CsPbBr₃ perovskite NCs.** (a) Normalized spectrally integrated PL intensity and corresponding PL quantum yield of CsPbBr₃ NCs on silica during O₂/vacuum cycles between P=1bar (highlighted with grey shades) and P=10⁻³bar. (b) Φ_{PL} during continuous excitation at 3.1 eV in 10⁻³ bar vacuum (green triangles) and in 1 bar of pure O₂. All measurements are conducted using 3.1 eV excitation with fluence of 100 nJ/cm².

A similar effect was observed in various metal chalcogenide NCs^{25, 68, 150, 175}. A schematic depiction of the interaction mechanism is drawn in Figure 1.11. In order to gain deeper insight into the time dynamics of the NC-O₂ interaction, in Figure 1.12a, we report the PL decay curves collected at each pressure step together with respective fit with double exponential functions. In agreement with the data in Figure 1.5b, for each curve, we find a fast decay component accounting for over 80% of the total signal followed by a slower decay responsible for the remaining 20%. Upon lowering the O₂ pressure, the fast portion of the PL decay dynamics

becomes progressively slower due to the suppression of nonradiative electron capture by O_2 molecules, while the long component remains largely unmodified.

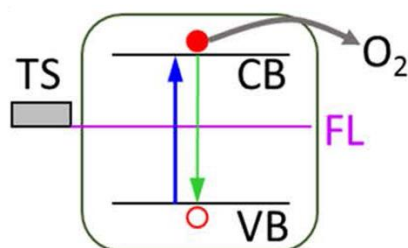


Figure 1.11. **Schematic of the O_2 -NCs interaction.** Schematic depiction of the interaction between O_2 and the NCs, showing direct extraction of photo-excited electrons from the conduction band (grey arrow) leading to quenching of the PL (green arrow), while surface defects (TS) placed close to the Fermi level (FL) in the absence of external potentials are essentially unaffected by oxygen. The excitation light is indicated with a blue arrow.

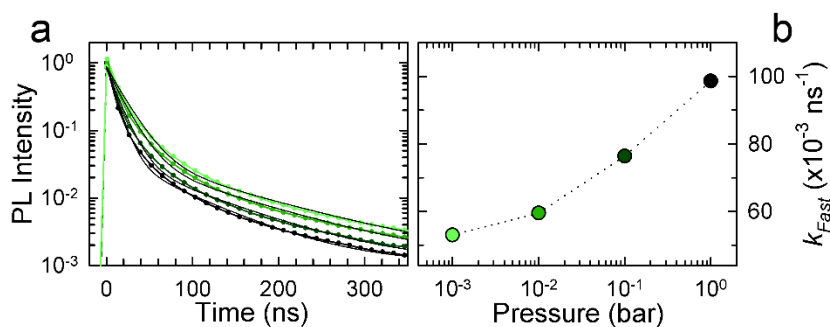


Figure 1.12. **Time-resolved analysis of a sample of $CsPbBr_3$ NCs under different pressure conditions.** (a) Normalized PL decay curves (dotted lines) corresponding to the pressure levels indicated by symbols in Figure 1.9a and respective double-exponential fitting curves (black lines). (b) decay rate of the fast component of the double-exponential dynamics of the NCs as a function of the O_2 pressure. All measurements are conducted using 3.1 eV excitation with fluence of 100 nJ/cm^2 .

Most relevant to distinguish between so-called 'static' and 'dynamic' quenching mechanisms¹⁷⁶, the early-time PL amplitude remains constant at any investigated pressure, which suggests that PL quenching by O₂ is a dynamic process that competes with radiative exciton decay on a comparable timescale, rather than a static ultrafast mechanism, which would lower the early-time PL intensity leaving the decay dynamics largely unaltered. In order to semi-quantitatively describe the observed trend, in Figure 1.12b we report the decay rate of the fast emission that accounts for the majority of the signal ($k_{\text{FAST}}=1/\tau_{\text{FAST}}$) at the various stages of the pressure ramp of Figure 1.9a. The k_{FAST} -values, obtained with no restraint of the fitting parameters, show a monotonic increase of the decay rate with increasing pressure with values scaling according to the observed difference of Φ_{PL} between the various pressure conditions (i.e. $k_{\text{FAST}}(P=1 \text{ bar})=0.99 \text{ ns}^{-1}$ is $\sim 30\%$ larger than the decay rate at $P=10^{-3} \text{ bar}$ ($k_{\text{FAST}}(P=10^{-3} \text{ bar})=0.074 \text{ ns}^{-1}$).

Finally, we point out that O₂ molecules might also adsorb onto the NC surfaces by bonding with unpaired surface electrons, leading to enhanced Φ_{PL} by suppressing their hole trapping capability, similarly to the application of a positive EC potential. This mechanism likely underpins the response to oxygen exposure of perovskite films and single crystals in refs.¹⁵⁶⁻¹⁵⁹ and determines the so-called 'reverse sensing' response of bi-dimensional CdSe colloidal nanoplatelets¹⁵⁰, whose Φ_{PL} is enhanced by adsorption of O₂, which passivates nonradiative hole traps that quench the PL in vacuum conditions. Therefore, similarly to the SEC trends, the overall PL brightening *versus* darkening response measured in oxygen sensitivity experiments provides direct insights into the competition between the two opposite effects of direct electron capture by collisional physical interactions between the NCs and O₂ molecules and their adsorption leading to passivation of unpaired surface electrons. For the perovskite NCs investigated here, the PL dimming in O₂ atmosphere indicates that direct extraction of photo-excited conduction band electrons by collisional interaction with gaseous or physically-adsorbed oxygen molecules is not counterbalanced by the passivation effect of hole traps by chemical adsorption of O₂ molecules, which is in good agreement with the weak (5%) PL brightening observed under positive EC potential (Figure 1.7) and thus independently suggests that the availability of active hole traps per NC in unperturbed conditions is likely small. We highlight that the stronger impact of hole traps on the radiative decay experienced by excitons in perovskite NCs

with respect to bulk or film perovskites, which strongly benefit from adsorption of oxidizing agents like molecular oxygen and water with respect to NCs, could result from both a larger density of defects on the surfaces of the latter, as well as from the long electron-hole diffusion length¹⁷⁷⁻¹⁷⁹ that enables photo-excited carriers to sample a large portion of the material surface and consequently be non-radiatively trapped in surface defects without their density being dramatically higher than in nanometric sized crystals.

1.3 Conclusions

In summary, we performed spectro-electrochemistry experiments and PL measurements in controlled oxygen atmosphere on CsPbBr₃ perovskite NCs to unveil the role of selective carrier trapping in structural defects, likely associated to surface states and dangling bonds, and the NC environment on the exciton recombination process. Results show that the main nonradiative channel in these NCs is capture of photo-generated holes in localized states that can be reversibly activated (passivated) upon raising (lowering) the Fermi level through the application of reductive (oxidizing) electrochemical potentials. As a result of the activation of hole traps, the PL is strongly quenched whereas their suppression leads to minor brightening, which strongly suggests that their density in unperturbed conditions is likely small. This feature has important consequences on the response of the NC's emission upon their exposure to oxygen gas that leads to strong quenching of the PL quantum efficiency due to the dominant effect of direct extraction of photo-excited electrons from the NC conduction band over the 'curing' behavior of surface hole traps responsible for the strong PL brightening registered for perovskite films and bulk crystals. This further suggests that, despite the much larger surface to volume ratio of nanocrystals with respect to bulk or film materials, electron rich surface defects are likely less abundant in the firsts, leading to an emission response dominated by direct interaction with the environment. Our results, therefore, suggest that the interaction between perovskite NCs and atmospheric agents could be detrimental to their optical properties and thus demands specific and, possibly, more effective passivation strategies for their optimization and stabilization.

Chapter 2

Reverse oxygen sensing with colloidal nanoplatelets towards highly emissive photoresponsive varnishes

This work was performed in collaboration with the Italian Institute of Technology (IIT, Genova).

Overview

Colloidal nanoplatelets combine the advantages of size-tunable electronic properties with giant oscillator strength and ultra-narrow emission spectra that make them ideal candidates for solution processed light sources and low-threshold lasers. A further application with great potential impact on life sciences, environmental monitoring, defense and aerospace engineering are solution processed analytical tools, such as luminescent sensing varnishes capable of detecting chemical agents through their reversible emission response. NPLs offer the ideal combination of high emission yield and vast reactive surfaces that are difficult to achieve using lower dimensional nanostructures. In this chapter, I combine spectroelectrochemical experiments and spectroscopic studies in a controlled atmosphere to demonstrate the 'reversed oxygen sensing' capability of CdSe NPLs, that is, the exposure to oxygen increases their luminescence efficiency, in contrast to conventional sensors that rely on photo-darkening to detect electron withdrawing agents. Spectroelectrochemical experiments allow me to directly relate the sensing response to the occupancy of surface states. Magneto-optical measurements demonstrate that, under vacuum, heterostructured NPLs stabilize in their negatively charged trion state. The high starting emission efficiency provides a possible mean to enhance the oxygen sensitivity by partially de-passivating the particle surfaces, thereby enhancing the density of unsaturated sites with a minimal cost in term of luminescence losses.

2.1 Introduction

Colloidal semiconductor nanostructures are solution-processable functional materials with great applicative potential in a variety of technologies, ranging from light-emitting diodes¹⁸⁰, photovoltaic cells¹⁸¹, and lasers^{58, 182} to luminescent markers⁶¹, plasmonics¹⁸³, single photon sources¹⁸⁴, nano-magnetic devices¹⁸⁵ and luminescent solar concentrators¹⁸⁶. The particular interest in this class of chemically synthesized systems arises from their tunable emission spectrum and high emission efficiency¹⁸⁷, as well as an easily manipulated surface chemistry and compatibility with solution-based fabrication processes. Among various types of semiconductor materials, CdSe and CdS have received particular attention over the years, which has led to the realization of a variety of zero-dimensional structures including spherical core/shell nanocrystals¹⁸⁸, axial dot-in-rods^{189, 190} and tetrapods¹⁹¹, dot-in-plates¹⁹² and dot in bulk nanocrystals^{77, 78}, as well as one-dimensional nanorods¹⁹¹, nanoribbons¹⁹³ and rod-in-rod structures¹⁹⁴.

More recently, growing attention is being dedicated to bi-dimensional nanostructures such as colloidal nanoplatelets (NPLs)⁷³. These strongly anisotropic systems, typically 1-2 nanometers thick and tens of nm in lateral dimensions, exhibit one dimensional confinement of the carrier wave-functions resulting in absorption profiles typical of quantum wells^{73, 74}, narrow emission spectra and giant oscillator strength^{74, 75}. Furthermore, NPLs possess exceptionally large exciton^{74, 182, 195} and biexciton binding^{182, 195} energy and suppressed Auger recombination^{75, 76}. Despite these remarkable optical properties, the NPLs emission efficiency, like that of zero- and one-dimensional systems, is typically limited by nonradiative carrier trapping into surface defects that becomes particularly detrimental due to their exceptionally large surface/volume ratio. Similarly to spherical or elongated CdSe structures, CdSe NPLs surfaces can be passivated with inorganic layers of CdS that feature small lattice mismatch (~4%) and lead to higher emission yields due to efficient suppression of surface trapping¹⁹⁶. Recently, NPLs with highly controlled thickness, shape and surface composition have been obtained, such as core/shell^{197, 198} and core/crown¹⁹⁹ CdSe/CdS NPLs, where a CdSe nanosheet is respectively vertically sandwiched or laterally surrounded by a CdS shell. The growth of a shell with larger band-gap

(CdS bulk $E_g=2.4$ eV) over a CdSe NPL (bulk $E_g=1.75$ eV) leads to the formation of a quasi type II junction^{200, 201} where the electron delocalizes in the Coulomb potential of the hole that remains instead confined to the CdSe core by the high valence band potential barrier, resulting in red shifted emission and longer radiative lifetimes¹⁹⁶.

Despite the tremendous advancements in NPL synthesis^{73, 197}, spectroscopy^{202, 203} and theoretical modeling^{73, 195}, a thorough comprehension of charge trapping and charging is still lacking in the literature and so are reliable guidelines for optimizing their optical performances and environmental stability through suitable surface passivation strategies. Furthermore, understanding the mechanism of surface trapping would allow us to fully exploit the reversible dimming of the photoluminescence efficiency observed for individual NPLs under vacuum²⁰³ to realize novel 'reverse luminescence sensors' that become brighter in the presence of oxygen²⁰⁴, in contrast to conventional sensors that rely on photo-darkening to detect electron withdrawing agents^{175, 205-207}. These active analytical tools are of great interest for a wide range of applications, spanning from life sciences²⁰⁷ to pollution monitoring and aerospace engineering²⁰⁸ that would strongly benefit from efficient luminescent sensing varnishes to probe variations of the oxygen level in the atmosphere. The practical realization of this device concept is however limited by the lack of dyes that exhibit the necessary balance between high luminescence efficiency, to provide detectable emission in ambient conditions, and good reactivity to ensure sufficient sensitivity to chemical agents. Reversible photo-brightening in wet gasses has been observed in spherical nanocrystals with un-passivated surfaces²⁰⁹ that, however, result in low emission quantum yield ($\sim 0.4\%$) and limited detection range ($\sim 25\%$)²¹⁰. Importantly, these systems showed reversible luminescence response to the presence/absence of water molecules but no sensitivity to dry oxygen. Colloidal QWs, with their extremely large surface-to-volume ratio and ultrafast radiative lifetimes, offer the ideal combination of high emission yield, vast reactive surfaces and, as we show below, strong sensitivity to O_2 , that make them highly suitable candidates for this technology.

Here we combine spectroelectrochemical (SEC) experiments and spectroscopic measurements in a controlled atmosphere to demonstrate the ability of NPLs to

probe oxidative species through brightening of their photoluminescence and to thoroughly investigate the roles of trapping and charging on their photophysics. In order to evaluate the effects of heterostructuring in the trapping behavior, we performed side-by-side experiments on both core-only CdSe and core/shell CdSe/CdS NPLs. O₂/vacuum cycles demonstrate the reproducibility of the sensing response for both classes of NPLs. Importantly, time-resolved PL experiments in a controlled atmosphere, corroborated by circularly-polarized magneto PL measurements at 2.5 K indicate that, similarly to spherical core/shell nanocrystals, hetero-NPLs stabilize in their negatively charged state under vacuum. Application of an electrochemical potential allows us to recreate the effect of oxidative or reducing environments on the NPL's PL in a highly controlled fashion and thereby to relate the observed sensing behaviors to changes in the occupancy of surface traps. Remarkably, by lowering the Fermi energy under positive potentials, we observe brightening of the PL of core-only NPLs and strong dimming of their emission when the Fermi level is raised at negative potentials, which confirms the dominant role of hole trapping over electron trapping in the quenching mechanism. In contrast, core/shell NPLs undergo luminescence quenching in both oxidative and reducing conditions. This behavior is ascribed to dynamic competition between electron and hole trapping resulting from the combined effect of reduced sensitivity of core-localized holes to surface defects and to recovered competitiveness of electron trapping over radiative recombination that, in quasi-type II heterojunctions, is slow due to reduced electron-hole overlap²⁹. In order to rationalize the SEC observations in terms of competition between the involved recombination channels, we develop a dynamic model that links the occupancy of hole and electron traps to the emission efficiency for both core-only and core/shell NPLs. Importantly, using core-only CdSe NPLs, we achieve a dynamic sensing range of 90% between atmospheric and 0.5 mbar vacuum condition with a remarkable initial emission quantum yield of ~35%, which demonstrates the suitability of this class of nanostructures for the realization of efficient and sensible luminescent oxygen sensing varnishes.

2.2 Results and Discussion

2.2.1 *Synthesis and optical properties of colloidal nanoplatelets*

The CdSe NPLs used in the present study have been synthesized using the synthetic route introduced in ref.¹⁸², which was based on the procedure described in ref.⁷³, by Dr Christodoulou from Prof. Moreels' group at the Italian Institute of Technology (IIT, Genova). Because of the high surface-to-volume ratio, considerable attention was paid to the purification processes, which was executed without non-solvents such as ethanol or methanol, in order to avoid a reduction of the PL quantum efficiency. The CdSe NPLs are about 2 nm thick, equivalent to ~5 monolayers of CdSe, with average lateral dimensions of 8.8 nm x 36.5 nm (standard deviations of 0.94 nm and 2.3 nm, resp.) as shown in the transmission electron microscope images in Figure 2.1a, performed after the synthesis by Dr Christodoulou and Prof. Moreels at the IIT in Genova. To obtain CdSe/CdS core/shell hetero-NPLs, the cores were over coated on each side with three monolayers of CdS following the layer-by-layer procedure developed by Ithurria and Talapin in ref.¹⁹⁷. The total thickness of core/shell systems is about 4 nm and lateral dimensions are 13.1 nm x 40.7 nm (standard deviation of 1.3 nm x 1.9 nm) (Figure 2.1b). The typical band structure of a CdSe core over coated with a CdS shell is depicted in Figure 2.1c, showing the ~450-650 meV offset between the valence band energies that leads to strong localization of the hole wave function in the core region. In contrast, the smaller 100-300 meV conduction band offset between CdSe and CdS (the exact values are still disputed)²¹¹, results in the partial delocalization of the electron wave function. Figure 2.1d reports the optical absorption (dashed lines) and photoluminescence spectra (PL, solid lines) of CdSe NPLs and respective core/shell heterostructures under continuous wave excitation at 3.1 eV. The absorption spectrum of core-only NPLs shows the characteristic narrow peaks associated with optical transitions of heavy- and light-holes at 2.43 eV and 2.57 eV, respectively, and to transition from the spin-orbit split-off sub-band to the conduction band at 2.93 eV. The PL spectrum is peaked at 2.41 eV and is Stokes shifted by ~20 meV from the heavy hole absorption feature. Core/shell CdSe/CdS NPLs show broader and red-shifted absorption and emission spectra,

as expected from reduced quantum confinement resulting from partial delocalization of the electron wave function over the shell region^{76, 196}.

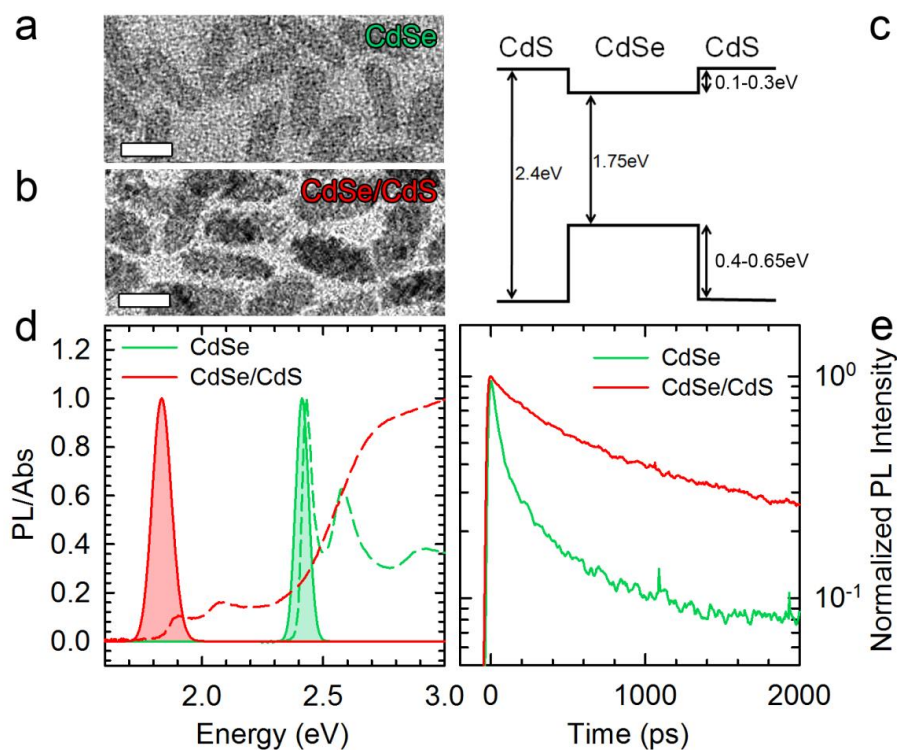


Figure 2.1. **Structure and optical properties of CdSe and CdSe/CdS NPLs.** Transmission electron micrographs of (a) core-only CdSe and (b) core-shell CdSe/CdS NPLs (shell thickness $H=0.95$ nm corresponding to about 3 CdS monolayers). Scale bars correspond to 25 nm. (c) A band alignment diagram of bulk CdSe and CdS. (d) Optical absorption (dashed lines) and normalized photoluminescence (solid lines, shaded in color) spectra of a hexane solution of CdSe (green lines) and CdSe/CdS (red lines) NPLs (excitation at 405 nm). (e) PL decay of core-only (green line) and core-shell (red line) NPLs recorded with a streak camera using 3.1 eV excitation.

The PL decay curves are shown in Figure 2.1e. In agreement with previous observations, NPLs ensemble as well as individual particles²⁰³ exhibit sub-nanosecond PL lifetimes⁷⁴ and non-exponential decay dynamics at room

temperature. Similar to spherical core/shell nanocrystals²¹¹ and axial CdSe/CdS heterostructures¹⁸⁹, reduced overlap between electron and hole wave function leads to an extended radiative PL lifetime for hetero-NPLs that, despite that, exhibit higher PL quantum yield (Φ_{PL}) with respect to core-only NPLs ($\Phi_{\text{PL}} \sim 60\%$ vs. $\Phi_{\text{PL}} \sim 35\%$ in solid film) thanks to reduced charge trapping in surface defects¹⁹⁶.

2.2.2 Oxygen sensing experiments

To investigate the effect of oxidative environments on the luminescence properties of NPLs and to demonstrate their reversed oxygen sensing capability, we monitored the evolution of the PL upon lowering the O_2 pressure in the sample chamber from atmospheric pressure to 10^{-4} bar (Figure 2.3a). Interestingly, both systems undergo significant PL quenching with decreasing pressure, thus confirming the surface passivating role of oxygen, whose removal progressively activates surface quenching sites. The nature of the defects responsible for quenching is provided by the comparison between core-only and core/shell materials, the first showing a much stronger dimming ($\sim 90\%$) than the latter ($\sim 55\%$ with respect to the initial value in O_2). In both core/shell and core-only NPLs, the electron wave function is expected to explore the surfaces essentially equally, given the ca. 1 nm thickness of the CdS shell (3ML of CdS, Figure 2.1b). Therefore, electron trapping alone cannot be held accountable for the observed different sensitivity to surface chemistry. The strong difference between the two samples lies instead in the accessibility of surface traps for core-localized holes, that is drastically reduced in CdSe/CdS NPLs. The observed stronger quenching for core-only materials therefore points to a key role of hole trapping in the quenching mechanism and outlines the ability of oxygen to saturate excess electrons on the NPL's surfaces. This picture is further confirmed by oxygen sensing measurements on core/shell CQWs with thinner shell ($h=0.32$ nm, corresponding to approximately 1 monolayer of CdS) that shows intermediate behavior ($\sim 65\%$ PL quenching) between core-only and core/shell CQWs with $h=0.95$ nm (Figure 2.2a-c). Importantly, no shift of the PL spectrum of both core-only and core/shell CQWs is observed during the pressure ramp (Figure 2.2a-c), which indicates that the observed trends are due to activation/passivation of

surface traps and not to oxidation/reduction of the CQW surfaces, as instead observed for spherical nanocrystals exposed to humid air¹⁷⁵.

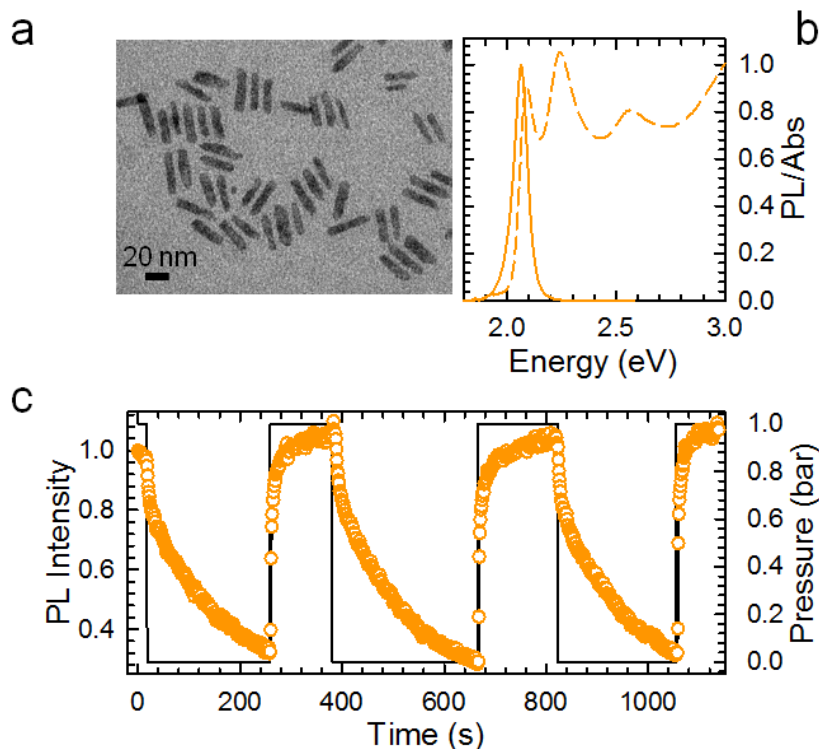


Figure 2.2. **Structural and optical properties of CdSe/1CdS CQWs and oxygen sensing ramp.** (a) Transmission electron micrographs of core/shell CdSe/1CdS CQWs, consisting of 2 nm thick CdSe core over-coated with 1 monolayer of CdS on each side ($h=0.32$ nm). (b) Optical absorption (dashed line) and photoluminescence (solid line) spectra of an hexane solution of core/shell CQWs under 3.1 eV excitation. (c) Integrated PL intensity of CdSe/1CdS CQWs during 'ON/OFF' O₂/vacuum cycles, starting from atmospheric pressure (1 bar) down to 10⁻⁴ bar. The pressure is shown as a black solid line. The PL intensity shows a ~65% dimming with respect to the initial values in O₂ and fully recovers after each cycle. Three cycles are reported to highlight the repeatability of the observed trend.

Interestingly, we notice that the PL drop occurs in two distinct time ranges, one instantaneous with the O₂ pressure change, leading to ~60% and ~15%

dimming for core-only and core/shell NPLs respectively, followed by a slow gradual decrease in efficiency at constant pressure ($\sim 10^{-4}$ bar) which accounts for the residual PL loss (semi-filled symbols in Figure 2.3a). To better understand this effect, we monitored the PL of both NPLs during stepwise pressure ramps.

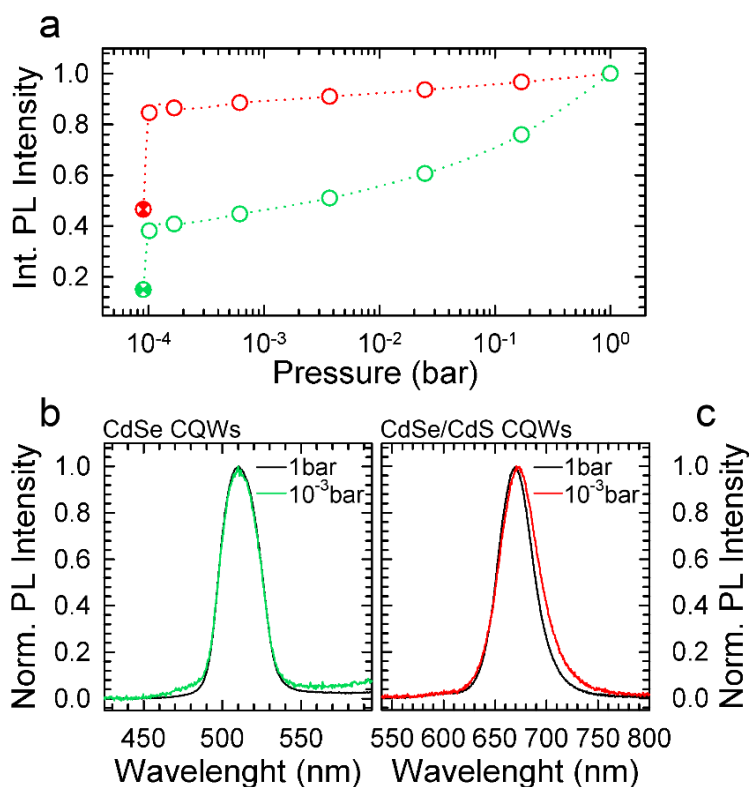


Figure 2.3. **CdSe and CdSe/CdS NPLs PL Intensity under increasing oxygen pressure.** (a) Integrated PL intensity of core-only (green circles) and core-shell (red circles) CdSe/CdS NPLs as a function of the chamber pressure (logarithmic scale). (b) Normalized PL spectra of (a) core-only (b) and core-shell NPLs (shell thickness $h=0.95$ nm) at 1 bar (black solid line) and 10^{-4} bar (green and red line, respectively). No significant shift of the PL spectra is observed, which indicates that the observed trends are essentially due to activation/passivation of surface traps and not to oxidation/reduction of the NPLs surface. All spectra are measured at room temperature under 3.1 eV excitation.(c).

The data reported in Figure 2.4a show similar phenomenology for core-only and core/shell NPLs (although more pronounced for core-only systems for the reasons explained above): at low vacuum levels ($P \sim 50\text{--}5$ mbar), the PL intensity correlates instantaneously with the chamber pressure, with an initial rapid drop concomitant to evacuation, followed by a plateau at constant pressure. On the other hand, at higher vacuum levels ($P < 0.5$ mbar), the dimming is more pronounced and proceeds in time even after the chamber pressure has reached full saturation. These observations point to the coexistence of two quenching regimes that reciprocally dominate the sensing behavior in different vacuum conditions. The first is responsible for the step-wise response to the chamber pressure and is ascribed to the rapid extraction of O_2 molecules weakly bound to the NPL film that passivate surface sites. The second leads instead to the slow progressive dimming in high vacuum conditions and is most likely due to the gradual desorption of adsorbates that require a larger driving force to detach from the NPLs surfaces.

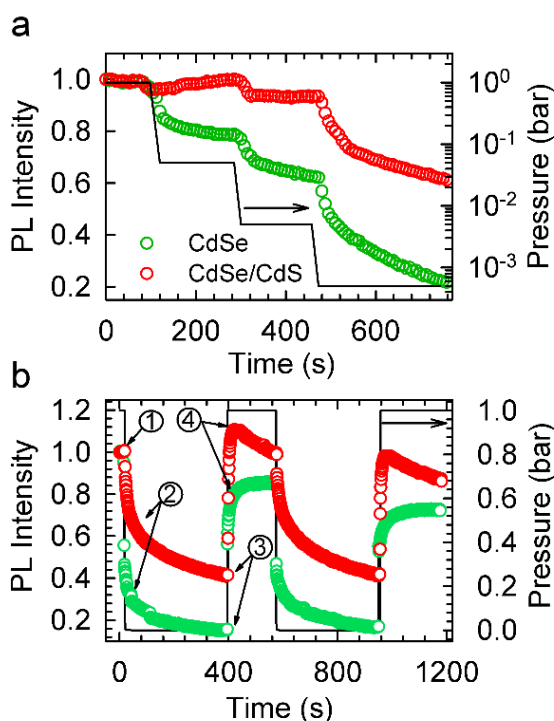


Figure 2.4. **CdSe and CdSe/CdS NPLs PL Intensity under changing oxygen pressure.** (a) Integrated PL intensity of CdSe (green) and CdSe/CdS (red) NPLs during a stepwise pressure scan. The pressure (black line, logarithmic scale) is reduced rapidly and then maintained constant for about 200 s while the PL transient is simultaneously monitored. (b) Integrated PL intensity of CdSe (green) and CdSe/CdS (red) NPLs during 'ON/OFF' O_2 /vacuum cycles starting from atmospheric pressure (1 bar) down to 10^{-4} bar. The pressure during the scan is shown as a black line. All measurements are performed at room temperature using 3.1 eV excitation.

This interpretation is supported by the ON/OFF pressure cycles reported in Figure 2.4b that also demonstrate the reproducibility of the sensing response. In these experiments, the sample chamber was rapidly evacuated from atmospheric pressure (1 bar in O_2) to $\sim 10^{-4}$ bar, while simultaneously monitoring the PL over time. Once the PL intensity had reached a plateau, the sample chamber was instantaneously filled with O_2 , so as to reestablish the initial pressure. Also in this

case, the PL was monitored until saturation before starting the successive cycle. Once again, we observe the rapid quenching for both core only and core/shell NPLs in the initial few seconds of each cycle, concurrently of the removal of about 99.99% of O₂ from the sample chamber.

Successively, the PL quenching proceeds slower while the pressure remains unchanged. Interestingly, pumping O₂ back in the chamber results in a symmetric trend: initially, the PL brightens rapidly, due to largely increased availability of gaseous molecules and proceeds slowly at atmospheric pressure as residual reactive defects are gradually saturated. The same behavior is observed for several consecutive cycles confirming the reproducibility of the sensing response and ensuring that the capping ligands are preserved. Detailed characterization of the sensing response including extended scans of over ten consecutive cycles, batch-to-batch reproducibility and stability tests are reported in Figure 2.5a-c, Figure 2.6 and Figure 2.7a-d, highlighting the reproducibility of the luminescence sensing response.

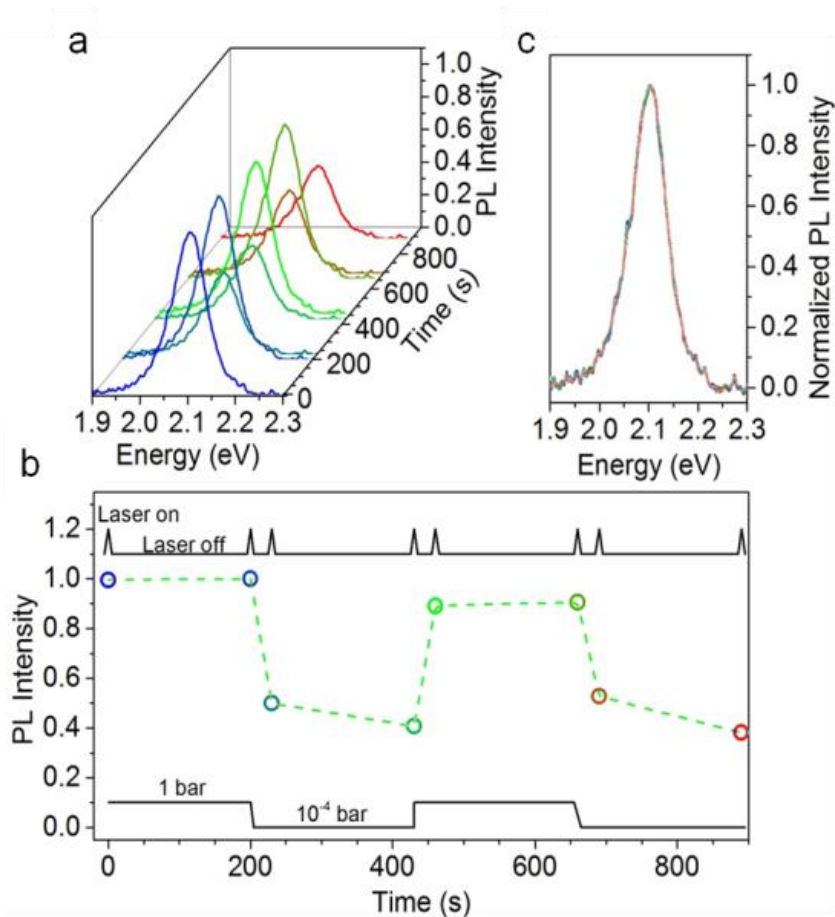


Figure 2.5. **Effect of illumination on the sensing response of CdSe CQWs.** (a) Photoluminescence spectra and (b) integrated PL intensity of CdSe CQWs during ON/OFF O_2 /vacuum cycles. The sample is kept in darkness except during the measurements of the emission spectrum when it is briefly illuminated (accumulation time 1 second). The PL is recorded in key conditions: in oxygen, just after evacuation, after 200 second at 10^{-4} bar, immediately after refilling with O_2 and after 200 s at 1 bar O_2 pressure. The scan is repeated twice to check the reproducibility of the response. The results show a similar behaviour to that observed under continuous illuminations, as shown in Figure 2.4 in the main text. This indicates that illumination does not significantly affect the quenching dynamics. (c) Normalized PL spectra shown in 'a'. No shift of the PL is observed in the different pressure conditions. The same colour scheme applies throughout the

figure.

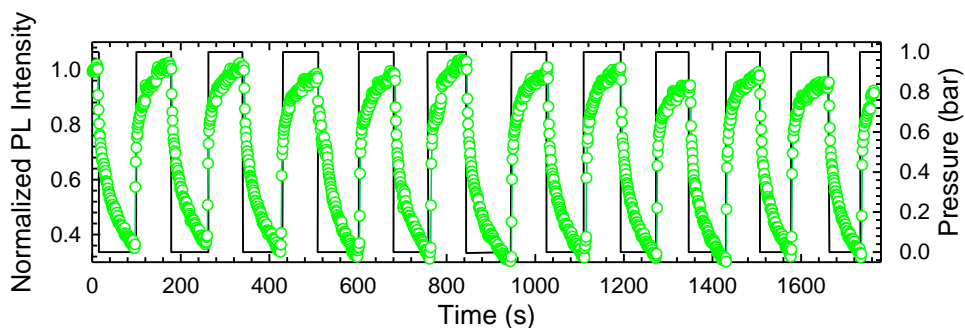


Figure 2.6. **CdSe NPLs under on/off oxygen pressure cycling.** Extended O_2 sensing cycling using CdSe NPLs. Integrated PL intensity of CdSe NPLs during 'ON/OFF' O_2 /vacuum cycles starting from atmospheric pressure (1 bar) down to 10^{-4} bar. The pressure during the scan is shown as a black line. All measurements are performed at room temperature using 3.1 eV excitation. The data show full repeatability of the sensing response and complete recovery of the initial PL intensity for over ten consecutive O_2 /vacuum ramps.

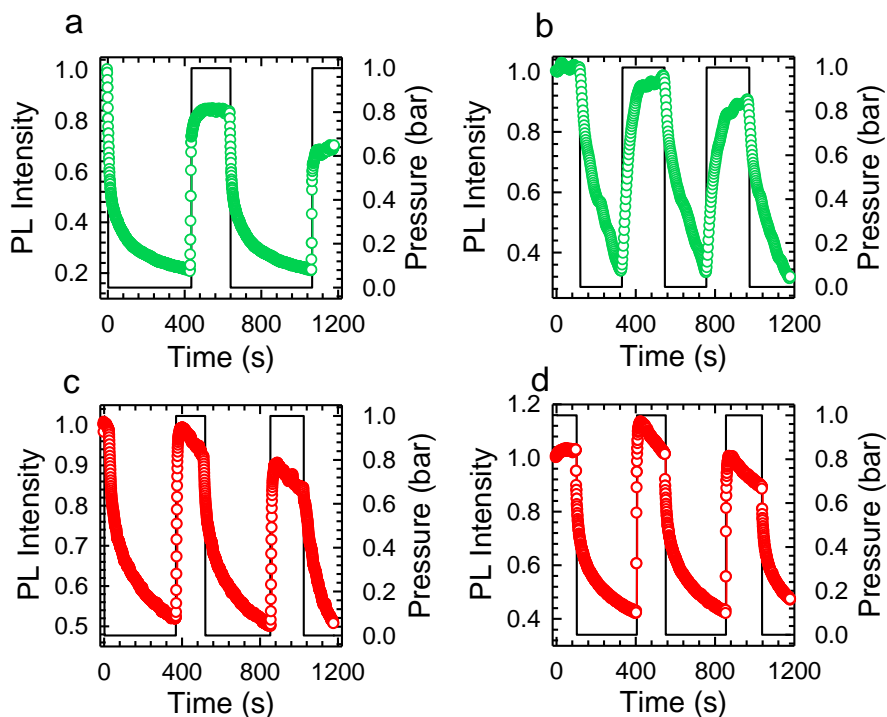


Figure 2.7. **Reproducibility of the O₂ sensing response for different batches of CdSe and CdSe/CdS core/shell NPLs.** Integrated PL intensity of CdSe NPLs during 'ON/OFF' O₂/vacuum cycles, starting from 1 bar down to 10⁻⁴ bar. The pressure during the scan is shown as a black line. Data in (a) refer to a new film cast from the same batch studied in the main text that was synthesized about one year ago. The CdSe NPLs shown in (b) are from a new batch now synthesized solely to check the batch-to-batch reproducibility of the sensing response. Integrated PL intensity of CdSe/CdS NPLs ($h=0.95$ nm) during 'ON/OFF' O₂/vacuum cycles starting from atmospheric pressure (1 bar) down to 10⁻⁴ bar. Data in (c) refer to a new film cast from the same batch studied in the main text that was synthesized about one year ago. The CdSe NPLs shown in (d) are from a new batch synthesized now solely to check the batch-to-batch reproducibility of the sensing response. The results show the reproducibility of the sensing behavior of different batches, which is also well maintained over shelf time up to one year after the synthesis. All measurements are performed at room temperature using 3.1 eV excitation.

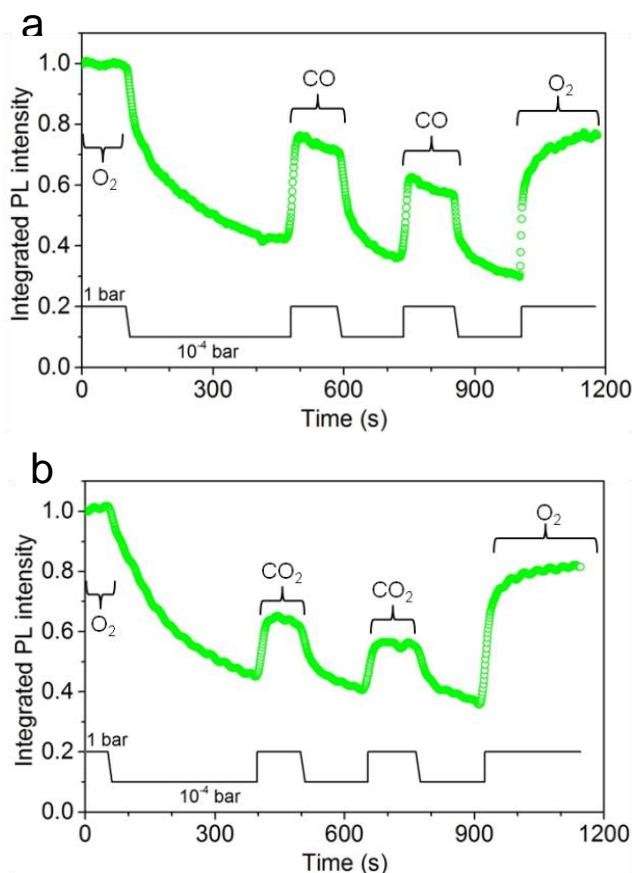


Figure 2.8. **Sensing response of CdSe NPLs to carbon monoxide and carbon dioxide.** (a) Integrated PL intensity of CdSe NPLs during 'ON/OFF' gas/vacuum cycles. The scan starts from 1 bar in O₂ from where the chamber is evacuated to 10^{-4} bar. After about 400 seconds, the chamber is filled with a CO/Ar mixture (500 ppm of CO in argon) (1 bar). After about 100 seconds the chamber is evacuated again to 10^{-4} bar. The scan is repeated twice to check the reproducibility of the response, after which the chamber is filled with O₂ (1 bar). The data show the dimming of the PL upon lowering the chamber pressure. Interestingly, the presence of CO leads to partial recovery of the PL intensity indicating weak sensitivity of the NPLs to the gas. The PL intensity is almost fully recovered once the chamber is refilled with O₂. (b) Same experiment as in 'a' but using CO₂ gas. The pressure during the scan in both panels is shown as a black line. All measurements are performed at room temperature under 3.1 eV excitation.

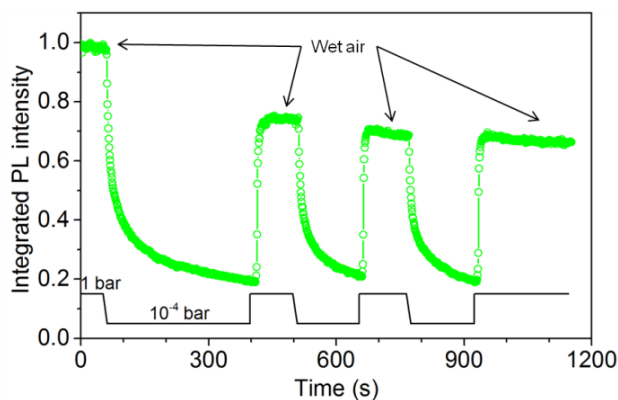


Figure 2.9. **Effect of humidity on the sensing response of CdSe NPLs to oxygen.** Integrated PL intensity of CdSe NPLs during 'ON/OFF' air/vacuum cycles starting from atmospheric pressure (1 bar) down to 10^{-4} bar. The absolute humidity is 20.5 g/kg, corresponding to common ambient conditions in which sensing varnishes could be employed (i.e. about 85% humidity at room temperature). The pressure during the scan is shown as a black line. The measurement was performed at room temperature using 3.1 eV excitation. The data show repeatability of the sensing response with a weak effect of humidity on the recovery of the initial PL intensity.

It is worth noting that refilling the sample chamber with nitrogen leads to no recovery of the PL intensity, which further confirms the essential role of oxygen, and not of the pressure itself, in passivating trapping sites.

To test the sensitivity of NPLs to other gaseous species, we performed ON/OFF pressure cycles using both carbon dioxide and carbon monoxide/argon mixture (Figure 2.8).

NPLs show reversible photo-brightening also in the presence of CO and CO₂ although to a lesser degree with respect to oxygen, which might further extend their potential use in environmental gas sensors. Importantly, the sensing response is reproducible also in the presence of humidity (Figure 2.9), thus making these systems particularly suitable for gas flow sensing in ambient conditions.

2.2.3 Time-resolved spectroscopy of colloidal nanoplatelets

In order to gain deeper insight into the quenching mechanism in different pressure conditions, we measured the PL decay dynamics of both samples in key steps of an ON/OFF pressure cycle as indicated by numbers in Figure 2.4b, namely: Step 1, the initial condition of atmospheric pressure; Step 2, the stage at which the chamber pressure is decreasing to $\sim 10^{-4}$ bar; Step 3, the end of the asymptotic PL dimming and Step 4, the maximum of the PL signal after recovery. The PL decay curves of core-only and core/shell NPLs are reported in Figure 2.10a and Figure 2.10b, respectively.

In any O_2 pressure condition, both systems show double exponential decay curves with a fast initial portion followed by a slower decay (respective lifetimes τ_{FAST} and τ_{SLOW}) that accounts for $\sim 70\%$ of the total luminescence of CdSe NPLs and for over 90% of the CdSe/CdS NPLs emission. This suggests that both ensembles consist mainly of two sub-populations of NPLs, one decaying primarily radiatively and the other one being dominated by non-radiative exciton relaxation. Specifically, we ascribe the long-lived component to radiative recombination of the sub-population of NPLs with suppressed surface trapping, that is larger in the CdSe/CdS NPL sample thanks to the passivation effect of the wide band gap shell, as also confirmed by the higher PL quantum yield with respect to the core-only material (60% vs 35%). On the other hand, the fast decay portion is assigned to trap-assisted recombination of the fraction of NPLs whose surface defects are not fully passivated by either the organic ligands or by O_2 and thus provide an additional efficient nonradiative recombination channel.

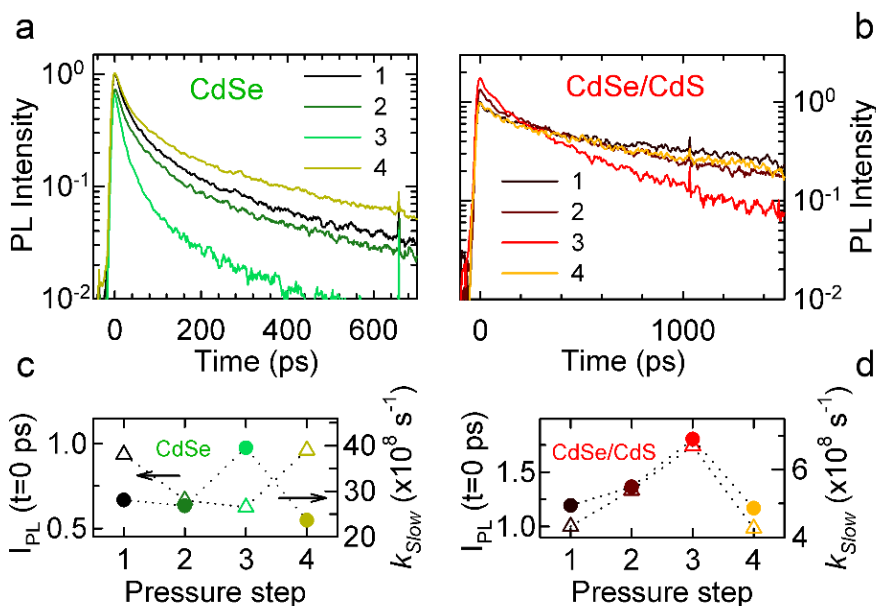


Figure 2.10. **CdSe and CdSe/CdS NPLS time-resolved PL intensity under different pressure conditions.** PL decay curves of (a) core only and (b) core/shell NPLs measured at the respective steps of the O_2 /vacuum cycles in 'c' (highlighted with sequential numbers). Decay rate of the slow component of the bi-exponential dynamics (triangles) and initial PL intensity, $I_{PL}(t=0 \text{ ps})$ (triangles) for both (c) core only and (d) core/shell NPLs. The same trends are observed for the fast decay contribution. All measurements are performed at room temperature using 3.1 eV excitation.

In Figure 2.10c,d we report the decay rate of the long-lived emission that accounts for the majority of the signal ($k_{SLOW}=1/\tau_{SLOW}$) at the various stages of the pressure ramp of Figure 2.4b, together with the zero-delay PL intensity values ($I_{PL}^{t=0}$) indicating the initial excited state population for both material systems. Although the quantitative description of the luminescence response is beyond the scope of this work, monitoring the evolution of these two parameters in the absence/presence of a specific analyte is instructive to distinguish between so-called 'static' and 'dynamic' quenching mechanisms¹⁷⁶. Specifically, a quenching process is typically considered as 'static' when it occurs on a timescale significantly faster than radiative recombination and thus lowers $I_{PL}^{t=0}$ without modifying the

decay kinetics. In contrast, a dynamic quenching process takes place concurrently to emission, resulting in accelerated decay rate, while $I_{\text{PL}}^{t=0}$ remains largely constant¹⁷⁶.

With this in mind, we first examine the behavior of core-only CdSe NPLs. Upon evacuating the sample chamber from atmospheric pressure to 10^{-4} bar (Step 2), we observe about a 30% reduction of $I_{\text{PL}}^{t=0}$ while k_{SLOW} is essentially unaffected (Figure 2.10). In direct opposition, at Step 3, the decay rate almost doubles its value while $I_{\text{PL}}^{t=0}$ remains unchanged. The same trend is observed for the fast radiative rate, k_{FAST} . This behavior supports the picture of two coexisting quenching processes: a static quenching mechanism that dominates at higher pressures and extracts photogenerated carriers on a time scale faster than radiative decay¹⁷⁶ and a slow dynamic quenching regime where gas desorption activates less efficient surface traps and thereby modifies the PL kinetics without affecting the initial excited-state population. Finally, upon pumping O_2 back in the sample chamber, the initial decay profile is reestablished (point 4). Single particle PL sensing measurements performed for a set of 30 NPLs confirm the distribution of the sensing response throughout the ensemble (Figure 2.11a-d). Specifically, about 20% of the investigated NPLs show strong quenching ($\geq 90\%$ of the initial PL intensity), 17% undergo weak dimming of their emission efficiency ($\leq 40\%$), while the remaining 60% show intermediate sensitivity. Importantly, the sensing response is independent on the initial PL intensity, as highlighted in the correlation plot of the PL quenching vs. initial PL intensity reported in Figure 2.11e.

Analysis of the time-resolved PL measurements reveals a fundamentally different behavior for heterostructured NPLs with respect to core-only materials (Figure 2.10b-d). Upon proceeding from Step 1 to 2 to 3 in the pressure ramp, the decay rate gradually grows, accompanied by an increase of $I_{\text{PL}}^{t=0}$, which implies that more photons are initially emitted at reduced pressure.

Concomitantly, however, the PL quantum yield drops (Figure 2.4b) indicating that the effect cannot be due to suppressed ultrafast trapping. These spectroscopic signatures are instead consistent with the recombination of charged excitons (trions), bound states composed of two carriers Coulombically coupled to the same carrier of the opposing sign.

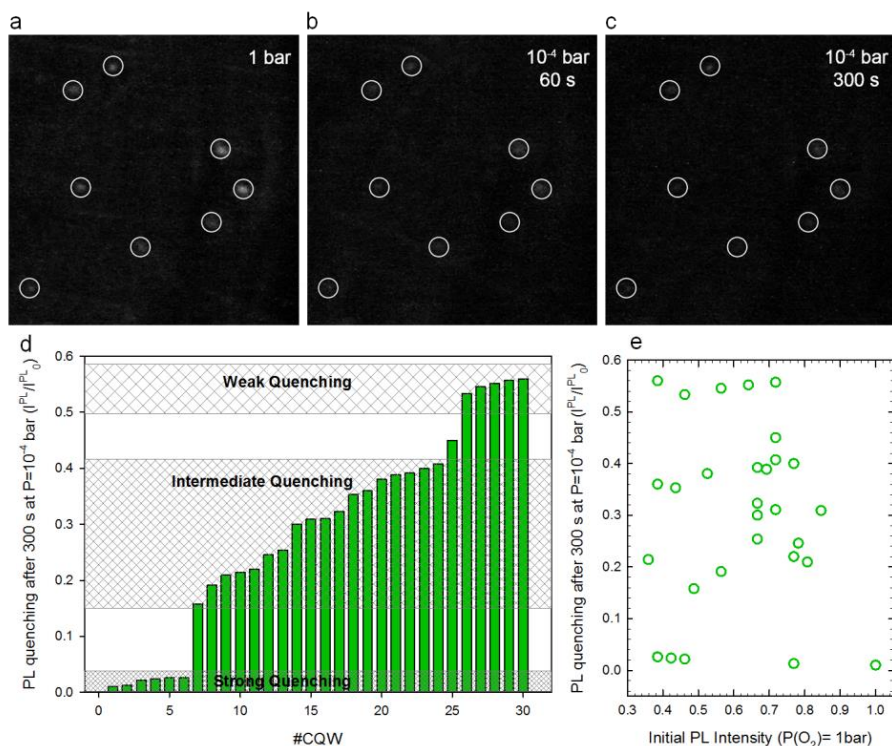


Figure 2.11. **Single particle investigation of the sensing response of CdSe NPLs.** Photographs of representative individual NPLs at (a) 1 bar oxygen pressure, (b) 60 seconds and (c) 300 seconds after evacuation at 10^{-4} bar, showing the progressive dimming of the emission intensity upon lowering the chamber pressure and prolonged exposure to vacuum. Individual particles are highlighted with circles. (d) PL quenching as defined as the ratio between the initial PL intensity and the intensity after 300 seconds at 10^{-4} bar for 30 individual NPLs. The histogram highlights three subpopulations showing strong, intermediate and weak quenching upon lowering the O_2 pressure. Importantly, the sensing response is independent on the initial PL intensity, as shown in the correlation plot of the PL quenching vs. initial PL intensity in (e).

In 0D quantum dots this typically results in doubled radiative decay rate and larger initial PL intensity with respect to neutral excitons^{212, 213}. Negative trion emission under vacuum has been recently observed in single particle experiments of so-called giant core/shell CdSe/CdS nanocrystals, which show blinking-free

trion emission with $\sim 100\%$ quantum yield at room temperature²¹⁴ and circularly polarized PL under magnetic fields at 4K, as a result of unbalanced spin population of the Zeeman-split trion sublevels¹⁶¹. In our case, efficient trion emission in vacuum could partially compensate for the activation of surface traps and thus contribute to the reduced PL sensitivity to the chemical environment of hetero-NPLs with respect to core-only materials.

2.2.4 Magneto-optical properties of colloidal nanoplatelets

In order to unambiguously ascribe the behavior of core/shell NPLs to trion emission and to investigate whether under vacuum our systems charge with an excess electron like thick-shell hetero-nanocrystals, we performed circular-polarization-resolved PL experiments at cryogenic temperatures under high magnetic fields (Figure 2.12). In these experiments, the sample is mounted in the variable temperature insert of a split-coil cryo-magnet with direct optical access and the circularly polarized PL is selected using a quarter-wave plate coupled to a linear polarizer. The degree of circular polarization (P_c) is defined as: $P_c = [\sigma^+ - \sigma^-] / [\sigma^+ + \sigma^-]$, where σ^+ and σ^- are the intensities of the right-handed (clockwise) and left-handed (counter-clockwise) circular polarized emission spectra. The sign of P_c is directly determined by the sign of the excess charge: a negative P_c corresponds to NPLs charged with an excess electron, while a positive value is observed for the decay of positive trions. The polarized emission spectra of CdSe/CdS NPLs at 2.5K are shown in Figure 2.12 together with P_c as a function of the magnetic field. Similarly to giant core/shell nanocrystals, core/shell NPLs exhibit negative P_c which, together with the PL dynamics in Figure 2.10b, indicate that under vacuum they are in a negatively charged state. On the other hand, the same measurements performed on core-only CdSe NPLs show no detectable circular polarization, which indicates that the ensemble is in neutral state, as reported in Figure 2.13.

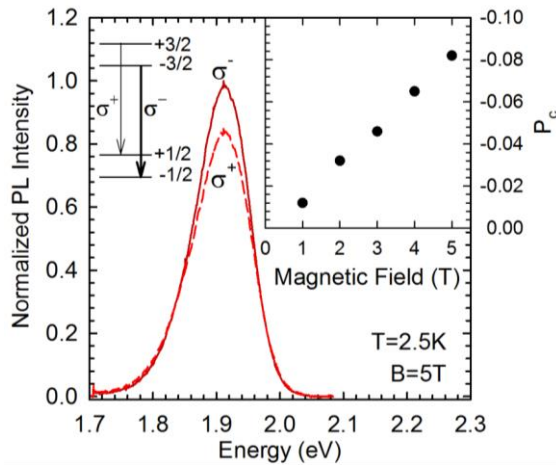


Figure 2.12. **Magneto optics of negatively charged core/shell NPLs.** Circular polarization-resolved PL spectra of CdSe/CdS NPLs at magnetic field of $B=5$ T and $T=2.5$ K measured using 3.1 eV excitation. The clockwise (σ^+) and counter-clockwise (σ^-) emissions are reported in dashed and solid lines, respectively. Inset: Magnetic field dependence of circular polarization degree (P_c) and scheme of the spin structure and optical transitions for negative trions in external magnetic fields.

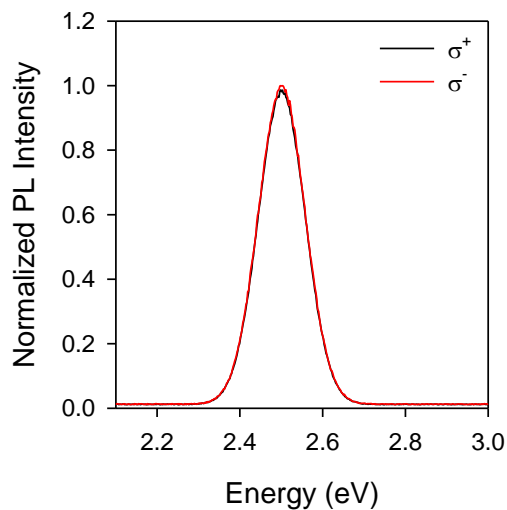


Figure 2.13. **Circular polarization-resolved PL spectra of CdSe CQWs.** Circular polarization-resolved PL spectra of CdSe CQWs at magnetic field of $B=5$

T and $T=2.5\text{K}$ measured using 3.1 eV excitation. The clockwise (σ^+) and counter-clockwise (σ^-) emission spectra are essentially identical and are reported in black and red lines, respectively.

2.2.5 Spectro-electrochemistry experiments

To further confirm our original assessment of the central role of hole trapping in the photophysics of NPLs and to relate the observed quenching trends to the population of surface defects, we conducted SEC measurements. SEC has been recently used by several groups for studying the mechanisms of luminescence blinking^{212, 215, 216}, charging²¹⁷, and nanocrystal doping^{169, 218} as well as to demonstrate the ratiometric sensing capability of multi-color emitting heterostructures⁷⁹. To date, no SEC study of bi-dimensional colloidal quantum structures is available in the literature.

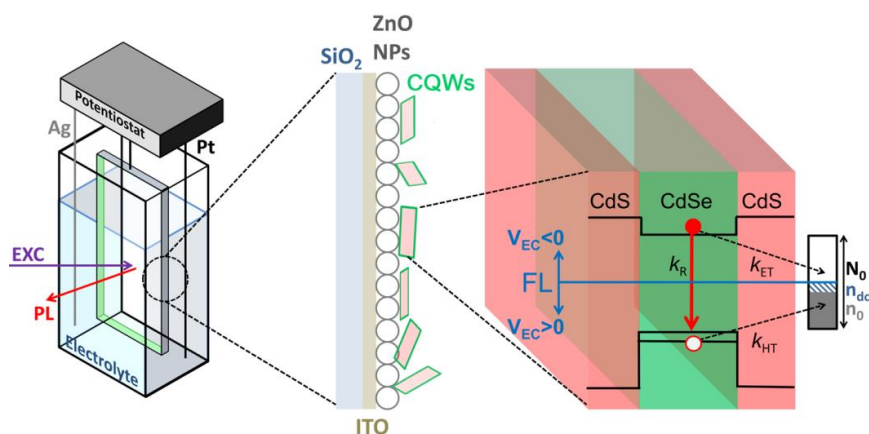


Figure 2.14. **Spectro-electrochemistry measurements on NPLs.** Schematics of the SEC setup: The electrochemical cell with 0.1 M TBAClO₄ in propylene carbonate as an electrolyte and a working electrode comprising an ITO-coated glass covered with a layer of ZnO nanoparticles (NPs) and NPLs on the top of the structure. A diagram illustrating the model used to describe the effect of the electrochemical potential on the PL intensity via filling/emptying of trap bands at the surface of the NPLs in response to changes in the position of the Fermi level (FL; blue line). The defect band at the NPL surface is shown on the right of the NPL.

The custom experimental setup used for these experiments is depicted in Figure 2.14. We start by recreating the effects of the removal of oxygen studied in the pressure-controlled experiments, by applying a negative electrochemical potential. In this condition, corresponding to raising the Fermi energy in the NPLs, surface defects are gradually filled with electrons, which activates their hole trapping capability. Simultaneously, intragap electron traps are progressively passivated. The PL intensity is thus determined by the competition between the quenching effect of hole withdrawal and the brightening effect of suppressed electron trapping.

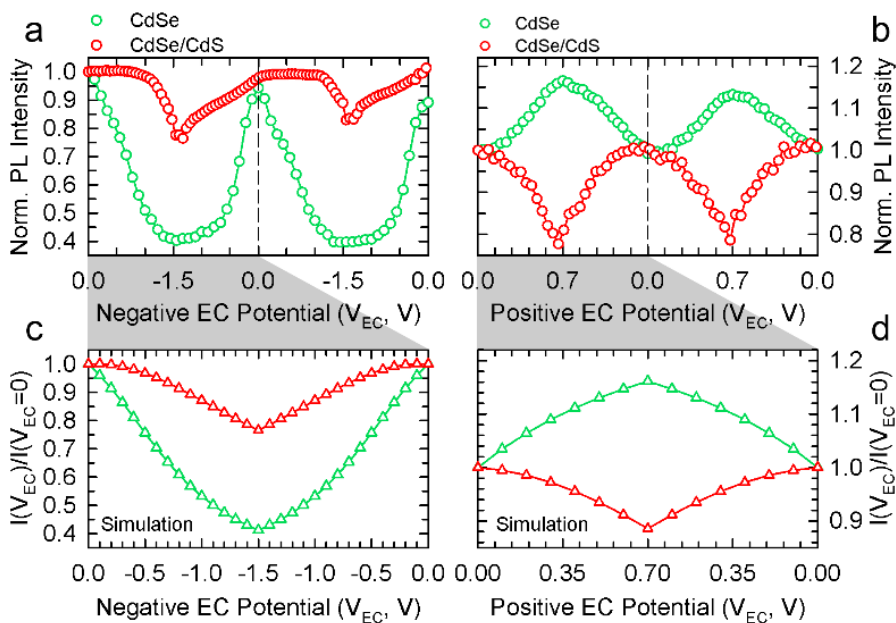


Figure 2.15. **Comparison between measurements and modeling of the PL intensity of CdSe and CdSe/CdS NPLs under negative and positive EC potential.** (a) Integrated PL intensity of CdSe NPLs (green circles) and core-shell (red circles) CdSe/CdS NPLs during a stepwise scan of the electrochemical potential to negative values ($V_{EC} < 0$). (b) Stepwise voltage scan for a positive electrochemical potential (from $V_{EC}=0V$ to $+0.7 V$). Two potential cycles are reported to show the repeatability of the process. (c) Filling the defect band with electrons (enhancing FL) under negative potential suppresses electron trapping but activates hole trapping leading to PL quenching of both core-only and

core/shell NPLs. (d) Depleting electrons from the defect band under positive potential enhances electron trapping but suppresses hole trapping resulting in enhanced PL from CdSe NPLs, whose dominant nonradiative channel is hole capture (capture rate k_{HT}). In contrast, core/shell CdSe/CdS NPLs undergo dimming of the PL efficiency due to activated electron trapping (k_{ET}).

In Figure 2.15a we monitor the evolution of the PL of both core-only and core/shell NPLs in a cyclic stepwise scan from $V_{EC} = 0V$ to $V_{EC} = -1.5V$ and back to 0 V. In agreement with the pressure ramps in Figure 2.4, upon increasing the negative potential, we observe strong PL quenching for core-only NPLs (~60% reduction), while the core/shell analogues are only weakly affected (20%). Interestingly, these reductions correspond to the PL drops observed during the initial step (Step 1 to Step 2) of the pressure ramp in Figure 2.4b, indicating that the electrochemical potential affects primarily the surface sites that respond instantaneously to the variation of the chamber pressure.

Next, we analyze the effect of a positive EC potential, which corresponds to lowering the Fermi energy in the NPLs (Figure 2.15b). This allows us to artificially expose our materials to an excess of electron poor agents with respect to the atmospheric condition and thereby to monitor the PL response to an even more severe oxidative environment. The data show a remarkable anti-correlation between the PL response of core-only and core/shell NPLs, with the first undergoing a progressive brightening of the PL intensity (~20% increase) while the latter are concomitantly quenched by a comparable degree. Once again, the increase of PL quantum yield of core-only NPLs under oxidative electrochemical potential can be explained in terms of suppressed hole trapping that dominates over the simultaneous activation of electron traps. The opposite effect describes instead the trend of core/shell NPLs, for which activated electron trapping is the dominant effect, similar to recent observations for CdSe/CdS dot-in-bulk nanocrystals⁷⁹. Taken together, these observations confirm our original assessment that nonradiative recombination in core-only NPLs is dominated by trapping of holes that is suppressed in oxidative environments while core/shell systems are mostly affected by electron traps. In both polarities, when returning back to zero potential, we observe reversible evolution of the two PL signals to their original intensity, indicating that potential sweeps do not cause any

permanent chemical degradation of the NPLs. Similar to that observed in the pressure scans, the normalized PL spectra (reported in Figure 2.16a,b for negative EC potential scan and Figure 2.16c-d for positive EC potentials) show no measurable shift under neither positive or negative EC potential, which confirms that the PL intensity trends are due to changes in the occupancy of surface sites and not to oxidation/reduction of the NPLs.

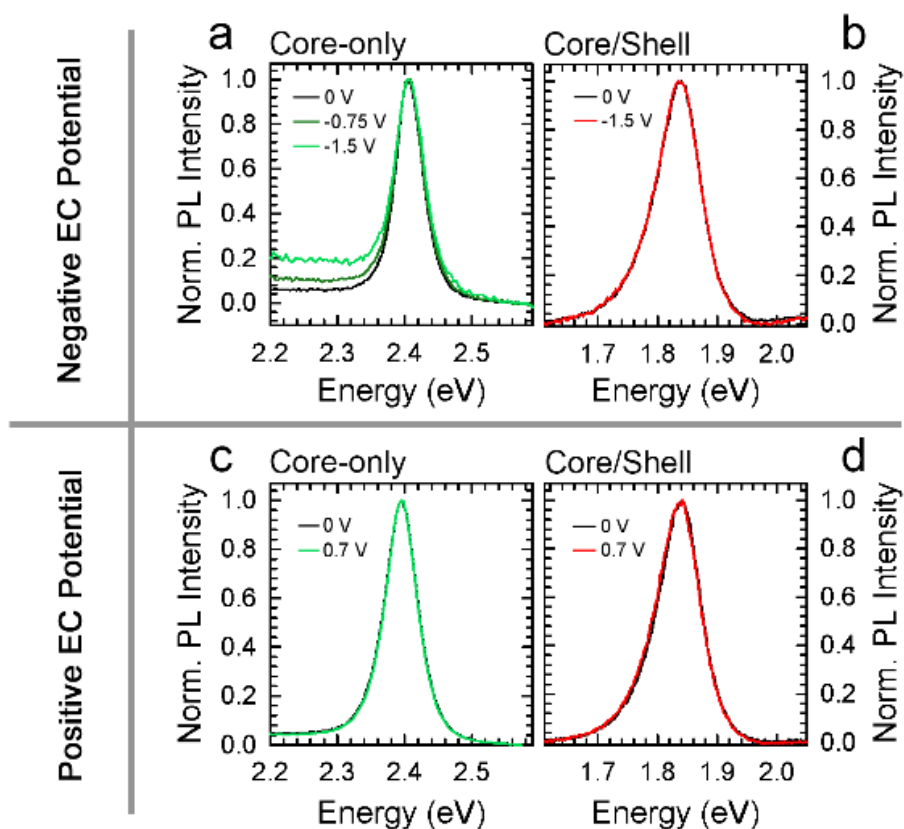


Figure 2.16. **Comparison of PL spectra of CdSe and CdSe/CdS NPLs under different EC potentials.** Normalized PL spectra at (a) 0 V, -0.75 V and -1.5 V for CdSe NPLs and (b) 0 V and -1.5 V for CdSe/CdS NPLs. Normalized PL spectra at (c) 0 V and +0.7 V for CdSe NPLs and (d) 0 V and +0.7 V for CdSe/CdS. No shift of the PL spectra is observed during the SEC scan, indicating that the PL intensity trends are due to activation/passivation of surface traps and not to permanent oxidation/reduction of the NPLs surfaces.

2.2.6 Kinetic model of surface trapping in colloidal nanoplatelets

To rationalize the SEC data, we propose a kinetic model that links the PL efficiency to the occupancy of surface traps that can be activated/deactivated by raising or lowering the electrochemical potential. The scheme of the photophysical processes occurring in the sample during the SEC measurements is depicted in Figure 2.14. Upon photoexcitation, electron-hole pairs can recombine radiatively with rate k_{rad} , or non-radiatively in surface defects. To account for the electron and hole traps, we introduce an electron trapping channel for electrons with rate k_{ET} , and a hole trapping channel with rate k_{HT} . We further assume that electron- and hole-trap sites are continuously distributed in energy across the NPL ensemble forming a “trap band” and only unoccupied sites can trap electrons while only occupied sites can trap holes. At zero EC potential, we consider the Fermi level to be at the center of the energy gap of the CdSe core, which defines the initial occupancy of trap bands (Figure 2.14). The application of a negative (positive) EC potential raises (lowers) the Fermi energy determining a variation of the trap occupancy. On the basis of these assumptions, we formulate a set of four rate equations for the population of photoexcited charges (conduction band electrons, n , valence band holes, p) and trapped carriers (n_T and p_T , for trapped electrons and holes respectively), and compute the evolution of the PL under oxidative or reductive potentials for a set of experimental parameters that are typical of samples studied in the present work (see the next section for details and model parameters). The results of the simulation under negative and positive electrochemical potentials are reported in Figure 2.15c and Figure 2.15d, respectively. This simple model reproduces the main experimental trends with core-only CdSe NPLs undergoing a progressive brightening at increasing positive potential as a result of suppressed hole trapping, whose rate strongly outcompetes electron trapping ($k_{\text{HT}} \gg k_{\text{ET}}$) in agreement with the time-resolved data in Figure 2.10a. The same argument explains the trend for negative potentials, where filling empty hole traps with electrons dramatically quenches the PL despite the fact that electron withdrawal is concomitantly reduced. Core/shell NPLs exhibit slower PL decay with respect to core-only systems ($k_{\text{rad}} \sim 4 \times 10^8 \text{s}^{-1}$ vs $k_{\text{rad}} \sim 3 \times 10^9 \text{s}^{-1}$ for core/shell and core-only, respectively). This results in electron trapping becoming competitive with radiative decay. Simultaneously, the core-shell motif

suppresses hole trapping and thereby leads to overall increased resilience of the emission yield to the electrochemical environment.

2.2.7 Rate equations

Here, we report the rate equations that describe the model depicted in Figure 2.14 and Figure 2.15.

We denote the populations of electrons in the conduction band as n , holes in the valence band as p , and trapped electron (holes) at defect sites as n_T (p_T). The excitation rate is kept constant to an arbitrary value. To express the variation of trap population with the EC potential, V_{EC} , we introduce a proportionality constant k ($[1/V]$) which allows us to express the relative trap occupancies in the units of voltage. We thus describe the number of empty electron traps as $\tilde{N} - \tilde{n}_0 + V_{EC}$, where $\tilde{N}_0 = N_0/k$ is the effective width of the defect band and N_0 is the number of traps per individual NS. $\tilde{n}_0 = n_0/k$ is the initial occupancy of the defect band at $V_{EC} = 0$ V, and n_0 is the number of occupied traps per individual NS in the absence of photoexcitation. The positive sign of V_{EC} accounts for the fact that negative EC potentials raise the Fermi level thereby reducing the number of empty electron traps. Similarly, we describe the number of active hole traps as $\tilde{n}_0 - V_{EC}$.

For both systems, we consider exclusively the long-lived portion of the NPL ensemble as it is responsible for the majority of the luminescence signal. The detrapping rate k_{DT} has been chosen slow enough so as to not interfere with the charge extraction processes yet non-zero so as to describe a closed system. This is in agreement with recent observations that detrapping in spherical nanocrystals can take up to several minutes²¹⁹. For core-only NPLs, the hole trapping rate has been chosen to be much larger than the radiative rate, in agreement with the ultrafast 'static' quenching observed in the time resolved PL measurements. Electron trapping rate is instead negligible. The rates for the core/shell NPLs reflect the balance between the radiative recombination channel and the competitive nonradiative relaxation pathways that indeed lead to symmetric quenching effect under positive and negative electrochemical potentials.

Once the steady state populations are obtained, we calculate the dependences of the emission intensity on V_{EC} from $k_{rad} \cdot n \cdot p$ and show them in Figure 2.15c-d as a function of the EC potential and compute the PL intensity as $I_{PL} = n \cdot p \cdot k_{rad}$.

Within this assumption, we can write the following rate equations for n , p , n_T and p_T as a function of the EV potential:

$$dn/dt = k_{ex} - k_{rad} \cdot p \cdot n - k_{ET} \cdot n \cdot (\tilde{N}_0 - \tilde{n}_0 + V_{EC} + p_T) - k_{DT} \cdot n \cdot p_T; \quad (1)$$

$$dp/dt = k_{ex} - k_{rad} \cdot p \cdot n - k_{HT} \cdot p \cdot (\tilde{n}_0 - V_{EC} + n_T) - k_{DT} \cdot n_T \cdot p; \quad (2)$$

$$dn_T/dt = k_{ET} \cdot n \cdot (\tilde{N}_0 - \tilde{n}_0 + V_{EC} + p_T) - k_{DT} \cdot n_T \cdot p; \quad (3)$$

$$dp_T/dt = k_{HT} \cdot p \cdot (\tilde{n}_0 - V_{EC} + n_T) - k_{DT} \cdot n \cdot p_T; \quad (4)$$

where the occupancies of the electron and hole states are related by the condition of charge neutrality: $n + n_T = p + p_T$. The numerical solution of the system of the rate equations is performed in the steady state regime (time derivatives equal to zero) using the values for the rates inferred from the measurements (see

Table 2 below) or, when not directly accessible, chosen accordingly to the observed phenomenology in order to qualitatively reproduce the main experimental trends.

	CdSe NPLs	CdSe/CdS NPLs
k_{rad}	3 ns ⁻¹	0.4 ns ⁻¹
k_{ET}	0.2 ns ⁻¹	0.5 ns ⁻¹
k_{HT}	30 ns ⁻¹	0.3 ns ⁻¹
k_{DT}	0.2 ns ⁻¹	0.2 ns ⁻¹
\tilde{N}_0	0.15 V	0.01V
\tilde{n}_0	0.05 V	0.05 V
k	10 V ⁻¹	10 V ⁻¹

Table 2. Rates values and parameters used in the numerical solution of the system of rate equations.

2.2.8 Demonstration of NPL-based 'reverse sensing' varnishes

The whole body of experimental results presented above indicates that colloidal NPLs are suitable materials for application in oxygen-sensitive coatings able to detect the presence of O_2 through reversible brightening of their PL. To provide a final proof of their potential, in Figure 2.17a,b we report the photographs of a CdSe NPLs film under UV illumination in O_2 and in vacuum, once again highlighting the remarkable difference between the emission intensity in the two conditions.

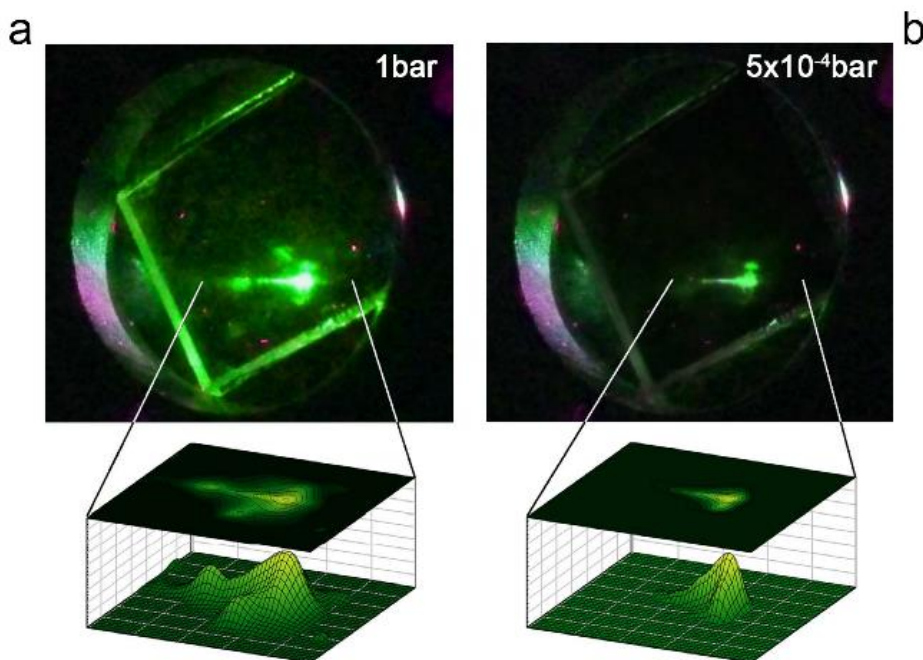


Figure 2.17. Photographs of a sample of NPLs for reverse oxygen sensing luminescent varnishes. Photographs and 3D surface intensity plots of a film of CdSe NPLs at (a) 1 bar O_2 pressure and (b) 5×10^{-4} bar vacuum under 3.1 eV excitation, showing the about one order of magnitude stronger luminescence in atmospheric conditions with respect to vacuum.

We stress that such sensing range is achieved using an efficient emitter with over 30% PL quantum yield in film form and for pressure variations around atmospheric values. This makes these novel two-dimensional colloidal structures particularly suitable for application as luminescent air sensing varnishes for applications including air flow studies in aerodynamic research (wind tunnel model) that currently rely on smoke, viscous fluids or evaporating suspensions for revealing transitions from laminar to turbulent flow as well as flow separation on airplane or car body parts. Furthermore, their high starting emission efficiency provides a possible means to further enhance the environmental sensitivity by partially de-passivating the surfaces of the NPLs and thereby to enhance the density of available surface sites with a minimal cost in term of luminescence losses.

2.3 Conclusions

In conclusion, we investigated the processes of charging and trapping in colloidal nanoplatelets by means of spectroelectrochemical methods and time resolved spectroscopy in a controlled atmosphere. The data demonstrates the brightening effect of oxygen on the emission of NPLs whose efficiency is mainly determined by hole trapping in surface defects. Spectroelectrochemical experiments reproduce well the observed environmental effects and further confirm the improved optical stability of heterostructured NPLs. The O₂ sensing process is reversible and could be used to realize novel 'reversed' analytical sensors capable of generating an enhanced light signal when exposed to harsh environments, with potential impact in aerospace planning, environmental sensing and smart building.

Chapter 3

Single-particle ratiometric pressure sensitive paints based on 'double-sensor' colloidal nanocrystals

This work was performed in collaboration with the Los Alamos National Laboratory (LANL, Los Alamos, New Mexico, USA).

Overview

Ratiometric pressure sensitive paints (*r*-PSPs) are all-optical probes for monitoring oxygen flows in the vicinity of complex or miniaturized surfaces. They typically consist of a porous binder embedding mixtures of a reference and a sensor chromophore exhibiting oxygen-insensitive and oxygen-responsive luminescence, respectively. In this chapter, I realize the first example of an *r*-PSP based on a single two-colour emitter that removes limitations of *r*-PSPs based on chromophore mixtures such as different temperature dependencies of the two chromophores, cross-readout between the reference and sensor signals and phase segregation. In this paradigm-changing approach, I utilize a novel 'double-sensor' *r*-PSP that features two spectrally-separated emission bands with opposite responses to the O₂ pressure, which boosts the sensitivity with respect to traditional reference-sensor pairs. Specifically, I use two-colour-emitting CdSe/CdS core/shell nanocrystals, exhibiting red and green emission bands from their core and shell states whose intensities are respectively enhanced and quenched in response to the oxygen partial pressure. This leads to strong and reversible ratiometric response at the single particle level and over 100% enhancement in the pressure sensitivity. These proof-of-concept *r*-PSPs further exhibit suppressed cross-readout thanks to zero spectral overlap between the core and shell luminescence and temperature independent ratiometric response between 0°C and 70°C.

3.1 Introduction

Pressure sensitive paints (PSPs) are effective, non-intrusive tools capable of mapping gas flows near complex surfaces and reporting on the concentration of oxygen in gas mixtures through remote optical detection. The foremost use of PSPs is in aerospace engineering, with applications ranging from aerodynamic tests of aircraft prototypes^{28, 220} to fundamental studies in acoustics⁴³, shock-wave propagation and transonic buffeting effects²⁷ (see Figure 3.1a,b). PSPs are also widely used in the design of complex fluidic and microfluidic systems²²¹, including supersonic micronozzles²²², microfluidic oscillators²²¹, microchannels¹⁶⁷, and in studies of pressure, heat-transfer and shear stress in micromechanical devices²²³ (Figure 3.1a,b). Furthermore, PSPs are employed in environmental monitoring²²⁴, marine research²²⁵, the food packaging industry²²⁶, medicine²²⁷ and biology²²⁸, and are particularly effective to detect a few order of magnitude of pressure variations, unlike conventional oxygen optical sensors that are able to probe minimal quantities of analyte in gas mixtures and are completely quenched in atmospheric conditions. Traditional PSPs consist of an oxygen sensitive organic chromophore dispersed in a porous organic⁴⁵ or inorganic^{43, 229} matrix (commonly referred to as a 'binder'). When exposed to O₂, the luminescence of the chromophore is quenched proportionally to the oxygen partial pressure, thus allowing for real-time pressure monitoring²³⁰. The all-optical working mechanism of PSPs makes these devices substantially simpler than conventional piezoresistive²³¹ or MEMS-based transducers²³² that require the integration of the sensors and the wiring on the investigated surfaces, which hinders their application in the case of moving or miniaturized parts²³². In addition, traditional non-optical sensors yield point-like pressure measurements, whilst PSPs allow one to map the gas flow with high spatial resolution on extended or complex surfaces with a single optical scan^{26, 43}. This largely simplifies the data processing, which is particularly challenging in the case of turbulent or supersonic gas flows²³³.

State-of-the-art organic PSP chromophores, such as metal porphyrins⁴⁶, pyrenes⁴⁹, and Ru(II) or Pt(II) complexes²³⁴, have good oxygen sensitivity but suffer from limited thermal²³⁵ and photochemical²³⁶ stability. The interaction with O₂, which generates singlet oxygen radicals, accelerates photodegradation under UV

illumination^{26, 233}, leading to luminescence drops ranging from 1%/hour (refs.^{26, 28}) up to 15%/hour (refs.³⁰). In addition, the temperature-dependence of the luminescence efficiency, typical of organic chromophores, introduces bias errors to the pressure data collected on different model parts and, therefore, requires continuous monitoring of the surface temperature and specific calibration protocols^{27, 28, 43, 237}. Mixtures of O₂-sensitive and temperature-sensitive chromophores, operating as pressure and temperature references for the other emitter, have been proposed to address this problem^{238, 239}. These PSPs require, however, effective encapsulation of the temperature sensor in oxygen-impermeable polymers to avoid cross-sensitivity issues.^{43, 240}

Colloidal semiconductor nanocrystals (NCs) have been recently proposed as potential alternative sensing materials for PSPs. NCs combine high emission efficiency⁵⁷⁻⁵⁹ and size-tunable electronic properties^{55, 180} with enhanced stability and exceptionally large surface-to-volume ratios^{24, 60}. Similarly to organic chromophores, O₂ sensing with NCs relies on quenching of the luminescence intensity under O₂ flow, mostly due to ultrafast extraction of surface and photogenerated electrons by oxygen¹⁴⁹. From the physical perspective, the extraction of electrons from the NCs by exposing them to O₂ replicates the effect of lowering the Fermi level by applying a positive (oxidative) potential in electrochemical measurements. In direct analogy, the removal of oxygen from the NC surroundings resembles the effect of raising the Fermi level under negative (reducing) electrochemical potentials^{77, 169, 212}. An advantageous feature of NCs from the standpoint of potential PSP applications is that the coupling of photogenerated carriers with phonons in these systems is much weaker than in organic chromophores², which results in a smaller variation of the emission quantum yield in the temperature range typically explored in PSP studies (10-40 °C)^{27, 43, 237, 239}. Examples of O₂-responsive NCs include CdSe¹⁷⁵, CdTe²⁰⁶, and CdSe/ZnS core/shell systems⁶⁹. These structures have been utilized for humidity detection and dry gas sensing, as well as biological sensing applications²⁴¹. As distinct from organic chromophores, the use of NCs as PSPs emitters potentially eliminates the need for the binder, as NCs can be deposited directly onto tested surfaces (Figure 3.1a). This is particularly advantageous for high frequency sensing²⁷, since the rate-determining process in the sensing response is typically

the permeation of a gas into the binder²⁸, which protracts the response time from a few microseconds with porous matrices²⁷ to tens of seconds for traditional polymeric binders⁵².

A common experimental difficulty of radiometric luminescence mapping using organic chromophores or conventional NC-based PSPs is that they require accurate quantitative measurements of the emission intensity across extended or complex surfaces under oxygen flow and UV irradiation. For this reason, wind tunnel aerodynamic tests are typically performed by comparing the results of 'wind-on' and 'wind-off' measurements in order to account for the experimental geometry, model misplacements^{28, 149, 233}, non-uniform distribution of the chromophore in the binder and an uneven thickness of the binder layer across the model surface^{233, 237, 242}.

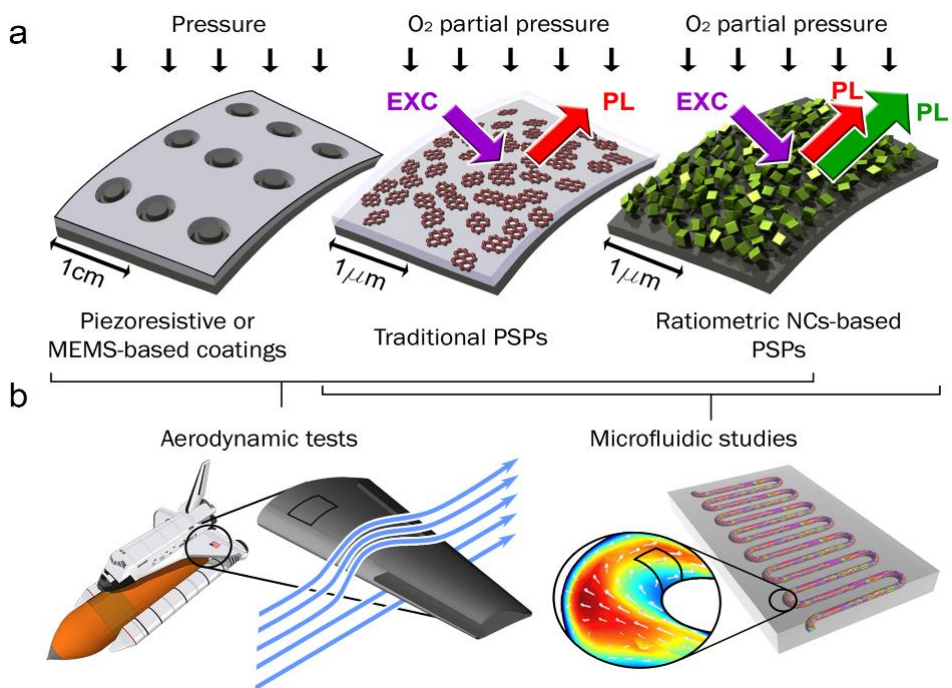


Figure 3.1. **Working principles of single- and double-sensor ratiometric PSPs.** a) Illustration of different technologies for pressure detection: (left)

traditional MEMS-based transducers, (center) traditional organic chromophore-based PSPs, and (right) DiB NC-based ratiometric PSPs. b) All of the pressure sensors from Figure 3.1a can be used in (left) aerodynamic tests on model surfaces, whereas (right) microfluidic systems can be investigated only by means of PSPs.

Some of these issues have been addressed through the use of so-called ratiometric PSPs (*r*-PSP) that exploit the different sensitivity to O₂ of two (or more) chromophores to detect and quantify local pressure variations. A conventional *r*-PSP consists of an O₂-insensitive chromophore (the 'reference') acting as an internal reference standard for the luminescence intensity of an O₂-responsive emitter (the 'sensor'), as depicted in Figure 3.2a.

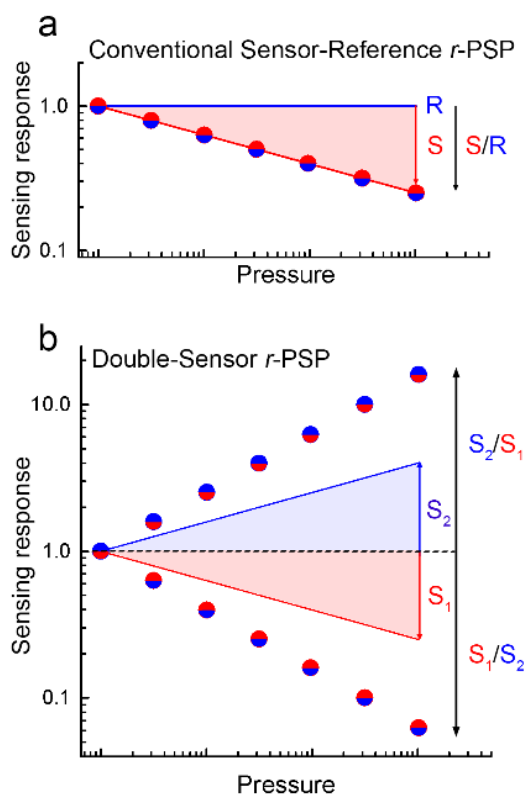


Figure 3.2. **Comparison between conventional and double sensor ratiometric PSPs.** (a) Representative plots of the ratiometric response of a conventional *r*-PSP featuring an inert (pressure-insensitive) reference (R, blue line) and an O₂ sensitive emitter (S, blue line). The ratiometric response (circles) is determined by the sensitivity of the sensor. (b) Ratiometric response of a double-sensor *r*-PSPs consisting of two O₂ sensing emitters (S₁ and S₂) with opposite luminescence responses. In this case, the ratiometric response (circles) can be expressed as S₁/S₂ or S₂/S₁; in either case, it is strongly amplified with respect to the sensitivity of the individual sensor species.

Examples of reported two-component *r*-PSPs include mixtures of organic dyes²³³ and dye-polymer conjugates³⁴ as well as organic/inorganic hybrid systems such as binary blends of dyes and NCs^{229, 233}, NC-polymer nanocomposites^{229, 243} and dye-functionalized NCs²⁴⁴. Although these systems virtually remove the need for

the wind-off/wind-on calibration, their use is still associated with several experimental difficulties arising from *i*) the different temperature dependence of the two chromophores^{233, 245}, *ii*) cross-read out errors due to the spectral overlap between the emission bands of the reference and the sensor²⁴⁶ and *iii*) spatial inaccuracy due to inhomogeneous distribution of the emitters on the model surfaces or in the binder²⁴⁶, whose effects are aggravated by intermolecular interactions leading to exciton migration processes^{34, 149}.

Here we demonstrate that all of these limitations can be alleviated using *r*-PSPs based on a single dual-colour emitter that features intrinsic ratiometric response at the single particle level, suppressed cross-readout due to a zero overlap between the luminescence spectra of the two emissive states, a dynamic range of ratiometric O₂-pressure sensing of three orders of magnitude, and the temperature-independent ratiometric response between 0°C and 70°C. To date, the only example of a single emitter showing ratiometric oxygen response is represented by fluorescent/phosphorescent macromolecules^{149, 247} proposed for tumor hypoxia diagnostics. An important advantage of our new approach is that it is based not on an inert (pressure-insensitive) reference, but instead combines two pressure-sensitive states in a single emitter and that these states exhibit opposite luminescence responses to changes in the oxygen pressure. In these 'double-sensor' systems, one emission channel is quenched, whilst the other is concomitantly enhanced by the presence of O₂, similarly to the so-called 'reverse sensing' behaviour recently found in CdSe colloidal nanoplatelets²⁴. Figure 3.2a,b schematically compare the luminescence-vs.-pressure dependence of a conventional reference-sensor pair (R and S, respectively) and that of a double-sensor *r*-PSP (respectively S₁ and S₂). Importantly, whilst the response of a conventional *r*-PSP featuring an inert reference is given solely by the sensor that determines the maximum ratiometric O₂-sensitivity of the blend (S/R in Figure 3.2a), replacing the inert reference with a 'reverse' O₂ sensor exhibiting enhanced luminescence when exposed to O₂ (S₂ in Figure 3.2b), leads to strongly amplified ratiometric sensitivity. We note that in the presence of two sensing species, the ratiometric response can be conveniently chosen (S₁/S₂ vs. S₂/S₁) in order to better suit the experimental conditions, whilst ensuring in both cases enhanced sensitivity with respect to the conventional reference/sensor system.

Our 'double-sensor', single-emitter *r*-PSP uses CdSe/CdS dot-in-bulk (DiB) NCs that consist of a small CdSe core overcoated with an ultra-thick CdS shell^{77, 78}. Owing to their peculiar internal structure, DiB NCs are capable of simultaneously sustaining core and shell excitons, whose radiative recombination leads to two-colour (red and green) luminescence under both low-fluence continuous wave (cw) optical excitation⁷⁸ and electrical injection⁷⁷. Two essential structural features of these NCs are an abrupt core/shell confinement potential and an engineered polytypic interphase of zincblende CdS separating the zincblende CdSe core from the thick wurtzite CdS shell. This peculiar structure of the core-shell interface slows down relaxation of shell-localized holes into core states, which leads to the development of efficient shell emission observed simultaneously with emission from the core²⁴⁸. Importantly for *r*-PSP applications, the shell excitons are exposed to NC surface species, and their luminescence is highly sensitive to nonradiative electron transfer to surface defects or molecular acceptors (in our case oxygen) adsorbed onto the NC surface that lead to luminescence quenching⁷⁹. In stark contrast, the emission arising from core-localized excitons is enhanced by exposure to O₂ as the removal of extra electrons generated by photocharging would quench nonradiative Auger recombination.⁷⁹ As a result of these effects, the two emission channels of the DiB NCs follow opposite trends with increasing/decreasing O₂ partial pressure, which allows us to realize the double-sensor ratiometric response regime using a single emitter.

3.2 Results and Discussion

3.2.1 ***Optical properties and temperature sensitivity of DiB-NCs***

The CdSe/CdS DiB NCs used in this study have been synthesized following the procedure reported in ref.⁷⁹ by Dr Bae from Prof. Klimov's group at the Chemistry Department of the Los Alamos National Laboratory (LANL, Los Alamos, New

Mexico, USA). Representative TEM images (also provided by Dr Bae and Professor Klimov) of the NCs and a statistical analysis of their dimension are reported in

Figure 3.3a,b.

Figure 3.3. **TEM and statistical analysis of a sample of DiB NCs.** (a) Transmission electron microscopy (TEM) image of an ensemble of CdSe/CdS Dot-in-Bulk (DiB) NCs. The inset is a TEM image of a single NC (scale bar is 5 nm). (b) Statistical analysis of the size of 300 DiB NCs from the TEM images using the short axis. The average size is 22 ± 2 nm (red lines).

A representative optical absorption and photoluminescence (PL) spectra of the DiB-NCs with core radius $R=1.5$ nm and shell thickness $H=8.5$ nm under cw excitation at 400 nm are reported in Figure 3.4a.

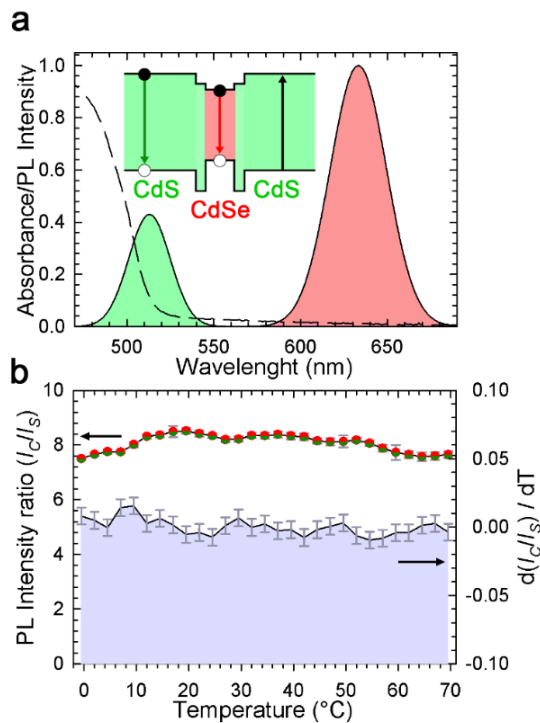


Figure 3.4. **Optical properties and temperature sensitivity of DiB NCs.** a) Optical absorption (dashed line) and normalized photoluminescence spectrum of a hexane solution of CdSe/CdS DiB NCs with the 1.5-nm core radius and the 8.5-nm shell thickness. Core and shell emission bands are highlighted by red and green shading, respectively. Inset: An approximate band diagram of CdSe/CdS DiB NCs, featuring an interfacial zincblende CdS layer that separates a zincblende CdSe core from a wurtzite CdS shell. b) Temperature dependence of the ratio between the core and the shell integrated PL intensities (I_C/I_S , red/green symbols) and the first derivative of the (I_C/I_S)-vs.-T dependence. All measurements were performed using the $15 \mu\text{J}/\text{cm}^2$ excitation fluence and the excitation wavelength of 400 nm.

The absorption spectrum shows a steep edge at ~ 500 nm due to absorption by the thick CdS shell whose volume is ~ 300 times larger than that of the CdS core. The PL spectrum consists of two well-separated emission peaks located at 632 nm and 512 nm. The 632-nm band is due to recombination of core excitons

characterized by the decay rate $R_{co}=5.5 \times 10^6 \text{ s}^{-1}$ (Figure 3.5a). The 512-nm peak arises from radiative decay of shell excitons which has the rate $R_{sh}=5 \times 10^9 \text{ s}^{-1}$ (as in Figure 3.5b).

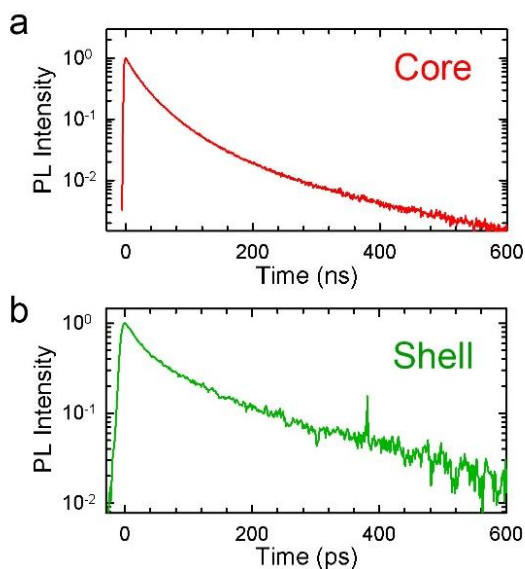


Figure 3.5. **Time resolved photoluminescence of DiB NCs.** Photoluminescence decay of (a) core and (b) shell emission of DiB NCs in hexane solution under 3.1 eV pulsed excitation.

As was established previously⁷⁸, electrostatic repulsion between the core- and shell-localized holes leads to a dynamic Coulomb blockade of the core states; as a result, the intensity of the shell PL exhibits complex dependence on excitation fluence (Figure 3.6). On the other hand, the core PL shows a more common pump-intensity dependence; it first grows linearly with pump power, and then saturates at high NC occupancies. The details of pump-power dependence of core- and shell PL bands, however, are inconsequential from the standpoint of ratiometric sensing, as pressure measurements usually utilize low-intensity excitation when both emission bands scale linearly with excitation fluence as illustrated in Figure

3.6 (highlighted in grey) for the pump-intensity change by more than two orders of magnitude.

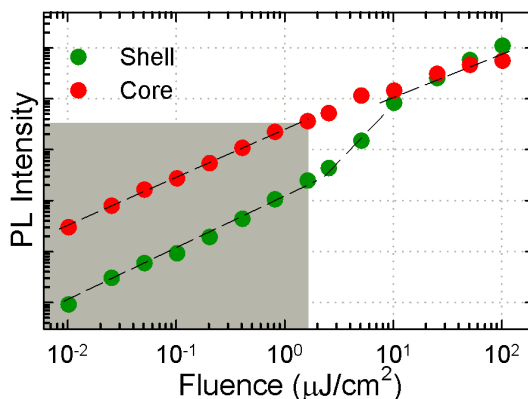


Figure 3.6. **Excitation fluence dependence of DiB NCs dual emission intensity.** Integrated PL intensity of core (red dots) and shell (green dots) emissions as a function of increasing 3.1 eV pulsed excitation fluence, plotted on a log-log scale. The grey shading highlights the excitation fluence range in which both the core and the shell emissions show linear trends.

Micro-scale pressure studies are affected by the exact type of PL pump-intensity-dependence to an even lesser degree, as they are typically performed at fixed excitation powers using focused light with a spot area comparable to the sample size. Most importantly for ratiometric sensing, both the core and the shell emission intensities (I_c , I_s) show nearly identical trends across a wide range of temperatures (0-70°C), which covers a typical range of temperature variation for many PSPs applications (10-50 °C, refs.^{43, 239}). This results in the remarkable temperature stability of the ratiometric response of DiB NCs, which in Figure 3.4b is evaluated in terms of the variation of the I_c/I_s ratio as a function of temperature. The same figure also reports the first derivative of the luminescence ratio, $d(I_c/I_s)/dT$, which emphasizes the absence of variations or drops in the ratiometric response over the whole range of investigated temperatures. We can quantify the temperature sensitivity (ST) of the DiB NCs through the expression ST

= - $[I_C(T_2)/I_S(T_2) - I_C(T_1)/I_S(T_1)] / (T_2 - T_1)$, where $I_{C,S}(T_1)$ and $I_{C,S}(T_2)$ are the intensities of the core and shell emission measured at the two extremes of the temperature range²⁸. By considering the temperature range, $T_1=0^\circ\text{C}$ and $T_2=70^\circ\text{C}$, we obtain the remarkably low value of ST of only 0.01%/°C; this is significantly lower than for the state-of-the-art two-components *r*-PSPs, which exhibit ST of 0.05 - 1.5%/°C.²⁸ We note, however, that the temperature trend of I_C/I_S is not monotonic, as commonly observed in traditional *r*-PSPs²³³, but shows a slight increase from 0°C to 20°C, followed by a weak drop with increasing temperature. In order to account for this trend, we have derived the maximum temperature sensitivity, ST_M , by considering the difference between the maximum and the minimum I_C/I_S -values divided by the temperature difference across the entire range of studied T. From this analysis, we obtain $ST_M=0.05\%/^\circ\text{C}$, which is still comparable to top-performing *r*-PSPs.

3.2.2 Ratiometric oxygen sensing using DiB NCs

We proceed with demonstrating the ratiometric O₂ sensing ability of DiB NCs by monitoring the evolution of their PL spectrum during stepwise pressure ramps from P=1 to 10⁻³ bar. In these experiments, a sub-monolayer film of DiB-NCs with core radius R=1.5 nm and shell thickness H=8.5 nm is dip-casted onto a glass substrate, which allows for homogenous coverage of the surface as shown in Figure 3.7a,b.

The luminescence of the sample is excited by 400 nm light and continuously collected with a CCD camera, while the sample chamber, originally filled with O₂, is progressively evacuated through rapid pressure steps. For each step, the pressure is lowered by a factor of ten and maintained constant for 90 seconds. After the final step at 10⁻³ bar, the chamber was refilled step-wise with O₂ following the same procedure. Since the O₂ concentration is proportional to the total pressure, these measurements directly yield ratiometric estimations of the pressure on the sample surface similarly to what is typically achieved with PSPs. As evident from the PL spectra in Figure 1.9a, the core and shell PL intensities demonstrate the opposite trend in response to changes in the chamber pressure. Specifically, the core PL undergoes progressive dimming upon evacuation, while the shell emission increases and becomes dominant at P=10⁻³ bar. Importantly,

refilling the sample chamber with nitrogen does not lead to recovery of the PL intensity, which confirms the essential role of oxygen in the sensing response.

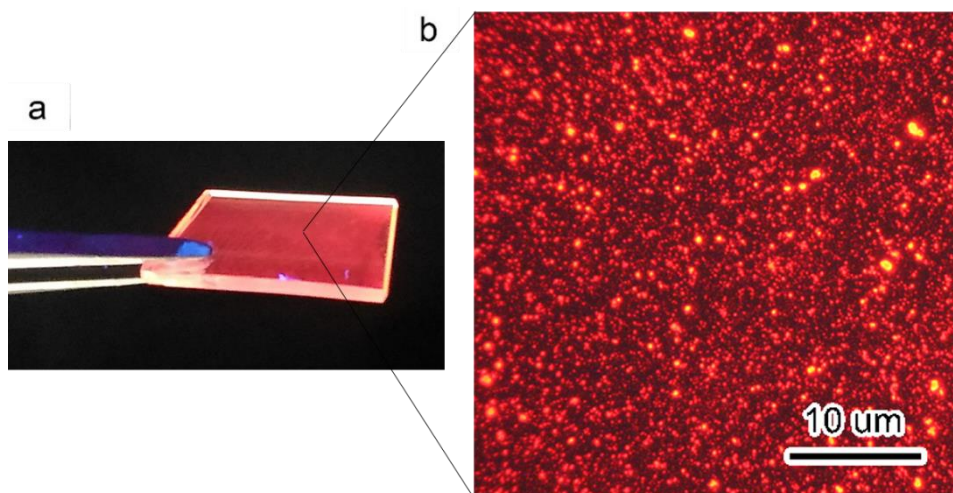


Figure 3.7. **Photographs of the DiB NCs sample.** (a) Photograph of the film of 1.5/8.5 CdSe/CdS DiB NCs used in our O_2 -sensing experiments under UV lamp illumination and (b) its image acquired with an optical microscope using a 20x objective with 0.40 NA under 3.1 eV excitation. The coverage of the substrate is 75%.

The observed difference between the O_2 response of the core and the shell PL can be rationalized by considering the electron withdrawing nature of molecular oxygen, which, in the ground state, is a diradical triplet with strong electron acceptor character. As a result, O_2 is capable of efficiently extracting electrons from both the quantized states¹⁴⁸ of the NCs and electron-rich surface defects that thereby become capable of trapping photogenerated electrons from the NC conduction band²⁴. Similarly to the effect of raising the NC Fermi level obtained by either applying a negative electrochemical potential or direct electric bias in light-emitting diodes^{77, 79}, the removal of oxygen progressively suppresses electron trapping, leading to the observed strong enhancement of the green luminescence due to increased radiative recombination efficiency of shell excitons. On the other hand, as observed previously^{161, 214} and confirmed by our time-resolved PL measurements in controlled atmosphere (see a detailed discussion

later in this work), the dimming of the core PL is associated with nonradiative Auger recombination of negatively charged core excitons (negative trions), which are formed due to accumulation of excess electrons in the NCs in the absence of electron withdrawing O_2 molecules. A similar effect has recently been observed with other CdSe/CdS heterostructures including thick-shell NCs^{161, 214} and colloidal nanoplatelets²⁴.

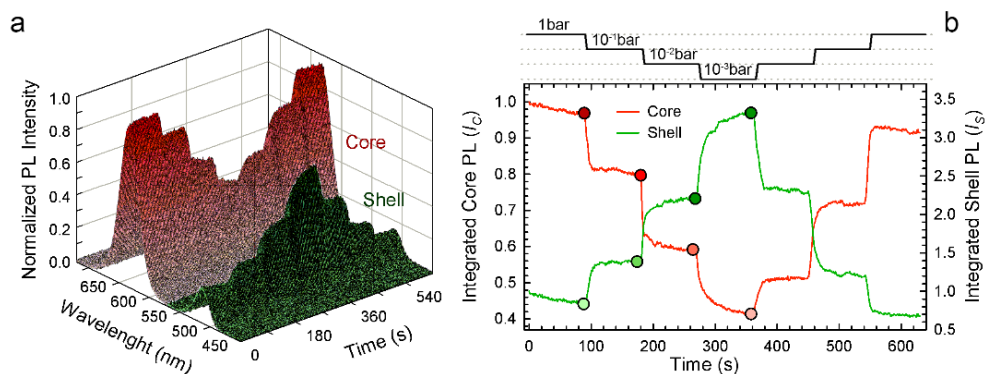


Figure 3.8. **Ratiometric oxygen sensing experiments with DiB NCs.** (a) A series of PL spectra (1 s acquisition time per frame, 90 s steps) during a stepwise pressure scan. The pressure is reduced rapidly and kept constant for 90 s, starting from atmospheric pressure ($P=1$ bar) to 10^{-1} , 10^{-2} and 10^{-3} bar, after which the sample chamber is stepwise refilled up to the initial pressure level of $P=1$ bar. (b) Integrated PL intensity of the core (I_C , red line) and the shell (I_S , green line) PL extracted from the stepwise pressure scan in 'a'. Both trends are normalized to the initial PL intensity values at $P=1$ bar.

In order to quantify the ratiometric luminescence response of DiB NCs, in Figure 3.8b we report the integrated core and shell PL intensity extracted from Figure 3.8a, both normalized to their initial value at $P=1$ bar. Each step-like variation of the O_2 pressure leads to a concomitant modulation of both emission bands. Specifically, lowering the pressure from 1 bar to 10^{-3} bar results in $\sim 60\%$ dimming of I_C and over 300% increase of I_S . Upon ramping the O_2 pressure back up to 1 bar, both the core and the shell emission bands fully recover their original intensities.

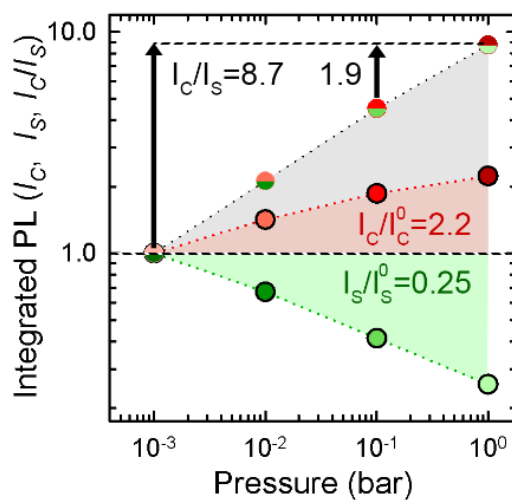


Figure 3.9. **Ratiometric oxygen sensing analysis of DiB NCs.** The I_C and I_S values (red and green dots, respectively) and the I_C/I_S ratio (red/green dots) as a function of increasing pressure (logarithmic scale). All trends are normalized to their respective value at atmospheric pressure (I_C^0 and I_S^0 respectively).

The opposite sign of the luminescence response of the core and the shell is emphasized in Figure 3.9, where we report I_C and I_S collected at the end of each

pressure step (highlighted with dots in Figure 3.8b) as a function of the O₂ pressure.

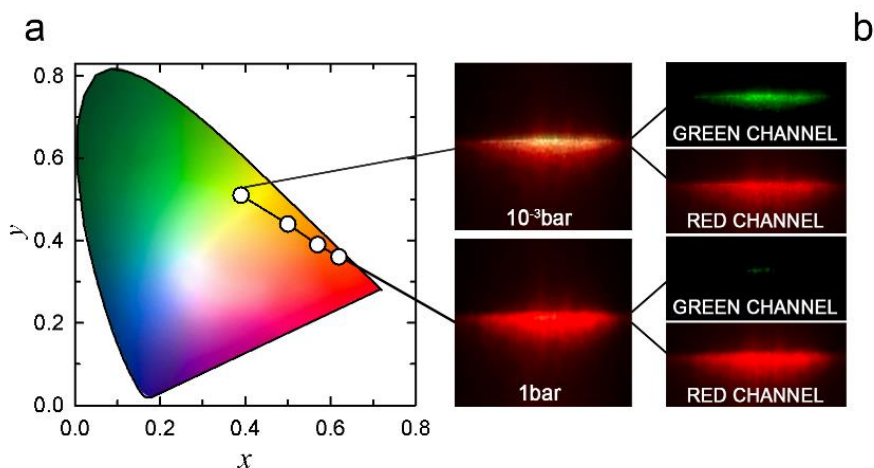


Figure 3.10. **Color-analysis of a sample of DiB NCs under different pressure levels.** (a) Overall emission colour of a DiB-NC film extracted from the PL spectra in 'a' and projected onto the CIE (Commission Internationale de l'Éclairage) chromaticity diagram. (b) Photographs of a DiB NCs sample at oxygen pressure of 1 bar and 10⁻³ bar (top left and top right, respectively) under UV illumination collected using UV-filtered camera (illumination spot 1 cm × 1 cm). The signals detected selectively by the red and green channels are reported in the right panels for direct confirmation of suppressed cross-readout.

In order to provide a solid method to compare the performances of our PSPs to other materials, we carried out a Stern-Volmer analysis on a step-like measurements as reported in Figure 3.11. The Stern-Volmer analysis is the most well-known model used to evaluate and compare PSPs materials and optical oxygen sensors, by reporting the ratio I_{Ref}/I as a function of the oxygen partial pressure (P/P_{Ref} , mostly used for PSPs applications) or oxygen concentration (mol, frequently used for generic oxygen sensing). When the analyte concentration is low enough to follow Henry's Law, the Stern-Volmer model results in a linear fit from which the linear coefficient, k_{SV} , can be extracted and used for comparisons of different materials. When deviations from linearity are present, due to inhomogeneity of the system, or when multiple orders of magnitude are probed,

the two-site Stern-Volmer model is used. Figure 3.11 reports a two-site Stern-Volmer plot with the total ratiometric response of DiB NCs as a function of the oxygen partial pressure (p_{O_2}), across three orders of magnitude of pressure ($P=10^{-3}$ - 1 bar) as in Figure 3.9. The analysis is based on the following equation:

$$\frac{I}{I^0} = \frac{f_1}{1 + k_{SV,1}^i \cdot p_{O_2}} + \frac{f_2}{1 + k_{SV,2}^i \cdot p_{O_2}}$$

Interestingly, this model holds for both the total ratiometric response and for the individual core and shell behaviors, as illustrated in the inset of Figure 3.11. This approach yields the following Stern-Volmer coefficients: $k_{SV,1}^{\text{Ratio}} = 1.26 \text{ bar}^{-1}$ ($=31.25 \text{ M}^{-1}$) and $k_{SV,2}^{\text{Ratio}} = 299 \text{ bar}^{-1}$ ($=7415 \text{ M}^{-1}$), which are in good agreement with literature reports^{34, 36, 38, 244, 249-251}.

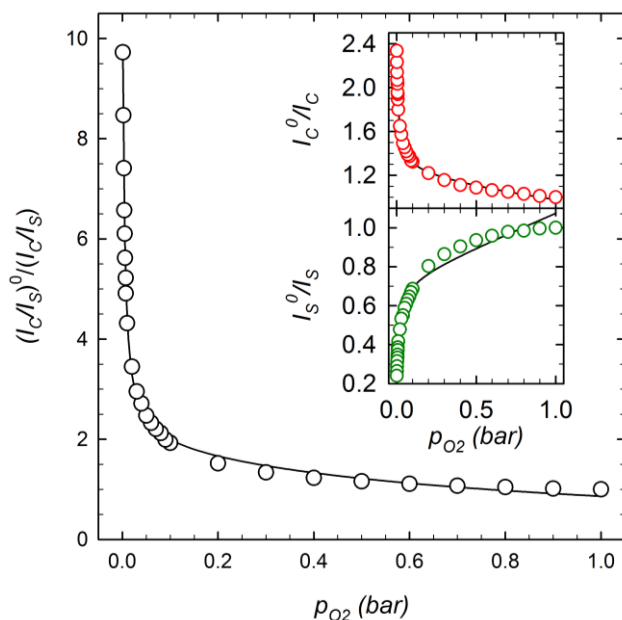


Figure 3.11. **Stern-Volmer analysis of the ratiometric O_2 -response of DiB NCs.** Stern-Volmer plot of the total ratiometric response, reported as $(I_c/I_s)^0/(I_c/I_s)$ as a function of the O_2 partial pressure p_{O_2} , for a pressure range from $P=10^{-3}$ bar to $P=1$ bar. The experimental data have been adequately fitted with the Stern-

Volmer equation applying the two-site model. The Stern-Volmer constants of the two sites are $k_{SV,1}=1.26 \text{ bar}^{-1}$ and $k_{SV,2}=299 \text{ bar}^{-1}$. The insets show the Stern-Volmer plot of the core and shell PL emissions, which highlight the "reverse" response of the core emission (upper panel, red dots). Both trends have been fitted with the same equation with $k_{SV,1}^{core}=0.277 \text{ bar}^{-1}$ and $k_{SV,2}^{core}=84.55 \text{ bar}^{-1}$ and $k_{SV,1}^{shell}=0.463 \text{ bar}^{-1}$ and $k_{SV,2}^{shell}=174.11 \text{ bar}^{-1}$. The conversion between $[\text{bar}^{-1}]$ and $[\text{M}^{-1}]$ has been performed using the ideal gas law and $T=298 \text{ K}$. The measurement is performed at room temperature using 3.1 eV excitation.

Thanks to the peculiar feature of the opposite response from the core and shell domains, the ratiometric response considerably exceeds the sensing response of the individual emitting states, with the enhancement reaching 100% with respect to I_S and over 600% with respect to I_C across the whole investigated pressure range. Interestingly, the strong response to the O_2 pressure leads to significant change of the total emission colour, as displayed in Figure 3.10a, which shows the projection of the emission colour coordinates extracted from the PL spectra of Figure 3.8a onto the CIE (*Commission Internationale de l'Éclairage*) chromaticity diagram. The colour change is easily appreciated by examining the photographs of the DiB-NCs film taken at $P=1 \text{ bar}$ and $P=10^{-3} \text{ bar}$ under UV illumination (Figure 3.10b). At atmospheric pressure, the film appears red, due to the dominant contribution of the core emission at 632 nm (see PL spectra in Figure 3.8a). Upon lowering the O_2 pressure to 10^{-3} bar , the total emission colour turns whitish, as a result of the contribution from strong green emission by the CdS shell. Importantly, since the core and shell emissions are fully spectrally separated a), their respective signals are collected selectively by the red and green detection channels with no cross readout. This is highlighted in the right panels of Figure 3.10b, showing a strong red signal and essentially no green emission at $P=1 \text{ bar}$. Under vacuum, the green signal increases significantly, whilst the red channel shows a concomitant dimming, in agreement with the quenching of the core PL observed upon evacuation of the sample chamber (Figure 3.8a-Figure 3.10a).

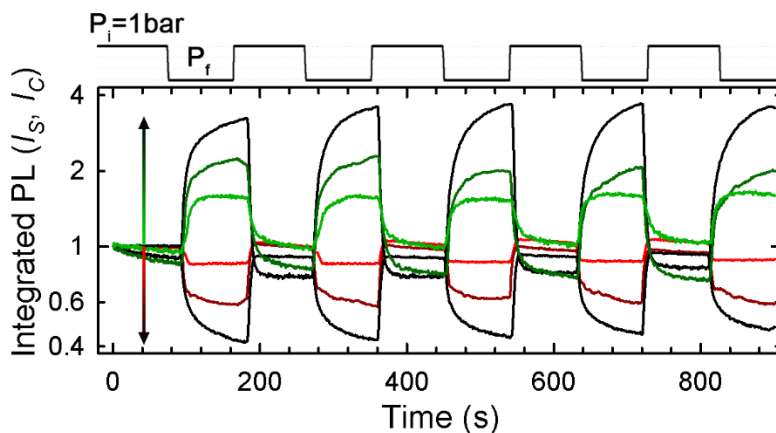


Figure 3.12. **Reproducibility and dynamics of the sensing response.** (a) Integrated PL intensity of core (red lines) and shell (green lines) during O_2 /vacuum cycles, starting from atmospheric pressure ($P_i=1$ bar) down to different final pressures, $P_f=10^{-1}$ bar, 10^{-2} bar and 10^{-3} bar, as indicated by arrows. The pressure steps are shown on the top of the panel for each P_i - P_f step. . All measurements are carried out at room temperature using 400 nm excitation; 1s acquisition time; each pressure step lasts 90 s.

In order to assess the stability of our *r*-PSP and the reproducibility of the sensing response, in Figure 3.12 we report the integrated intensity of the core and shell emission during many O_2 /vacuum cycles, in which the PL is continuously monitored while the sample chamber is rapidly evacuated from atmospheric pressure to 10^{-1} , 10^{-2} and 10^{-3} bar. Each pressure is maintained for 90 seconds after which the initial O_2 pressure is rapidly restored. For any final vacuum level, the luminescence response of both the core and the shell correlates rapidly with the pressure change, which is particularly relevant for high frequency sensing measurements. This is a direct consequence of both the ultrafast nature of the electron trapping process and the fact that our *r*-PSPs can be processed by depositing the DiB NCs directly onto the substrate, without the need for a polymeric binder that typically leads to long response times due to slow permeation of molecular oxygen⁵². The initial emission intensity is fully recovered after each cycle, thus confirming the reproducibility of the sensing response and ensuring that the capping ligands are intact.

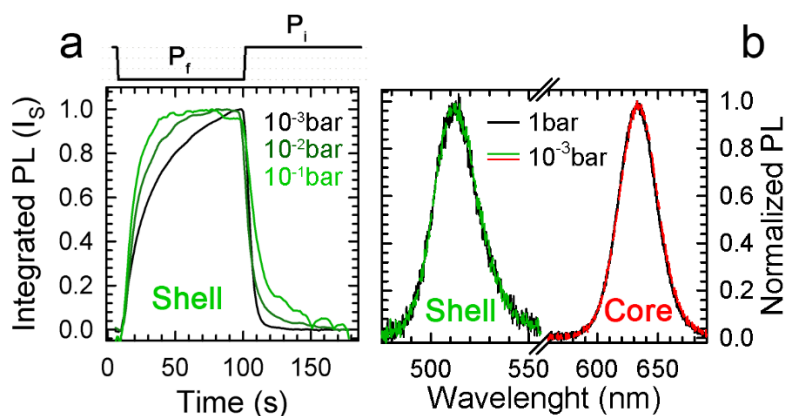


Figure 3.13. **Sensing response dynamics at different pressure levels.** (a) Evolution of the shell PL extracted from 'a' as a function of time for the three O_2 pressure ranges, normalized at their maximum value. (b) Normalized shell and core PL spectra at $P=1$ bar (solid black lines) and $P=10^{-3}$ bar (dashed green and red lines).

We notice that, upon evacuating the sample chamber from 1 bar to 10^{-1} bar, the PL intensity of both the core and the shell correlates rapidly with the O_2 pressure change, leading to an approximately two-fold increase of the shell emission and $\sim 20\%$ dimming of the core PL, followed by a plateau at a constant pressure. On the other hand, at $P=10^{-2}$ - 10^{-3} bar, the PL brightening/dimming is more pronounced (Figure 3.8a,b and Figure 3.12) and proceeds in time even after the chamber pressure has stabilized. This effect is highlighted in Figure 3.13a, where we display the shell PL traces of Figure 3.12 normalized to their intensity maximum for clarity. These observations point to the coexistence of two interaction regimes between the NCs and O_2 that respectively dominate the sensing behaviour under high- and low-pressure conditions. The first is responsible for the stepwise PL response concurrent to the removal of $\sim 99.9\%$ of O_2 from the sample chamber and is ascribed to suppressed electron trapping by collisional interaction between the NC film and molecular oxygen. Accordingly, pumping O_2 back into the chamber results in essentially instantaneous dimming of the shell PL due to largely increased availability of gaseous O_2 molecules in direct contact with the NCs. The second regime leads instead to the slow progressive brightening at lower

pressure, which is most likely owing to the gradual desorption of adsorbed O₂ molecules that require a larger driving force to detach from the NCs surfaces. Notably, no shift of the core and shell PL peak is observed (Figure 3.13b), which confirms that the sensing response is not due to permanent oxidation/reduction of the NCs surfaces²⁰⁹. In order to further assess the suitability of our *r*-PSPs for extended time applications, we tested their stability over prolonged exposition to continuous illumination and O₂/vacuum cycles. Detailed measurements of the sensing response including extended scans of over ten consecutive O₂/vacuum cycles between 1 bar and 2 bar O₂ pressure with different time intervals, and the stability test under UV illumination for over 2 hours are reported in Figure 3.15.

All measurements show full repeatability and stability over time, with no losses of either the PL intensity and the sensing capability over several hours of continuous sensing. From the point of view of prospective applications, it is also important to understand whether the interaction between the NCs and molecular O₂ is a photo-assisted process, as this might affect the accuracy of pressure measurements. To evaluate the effect of exact excitation conditions on the measured radiometric response, we have performed ON/OFF pressure sensing measurements using the same experimental procedure as the one described above while monitoring the NC emission under either continuous or pulsed (10 second pulses) 400 nm excitation. For direct comparison between the two excitation conditions, in Figure 3.14a,b we report the intensity traces for the core and the shell respectively, with five cycles collected using pulsed excitation and five cycles monitored under continuous illumination. No differences in the sensing response are observed, which indicates that the NC-O₂ interaction occurs identically under "dark" and "light" conditions.

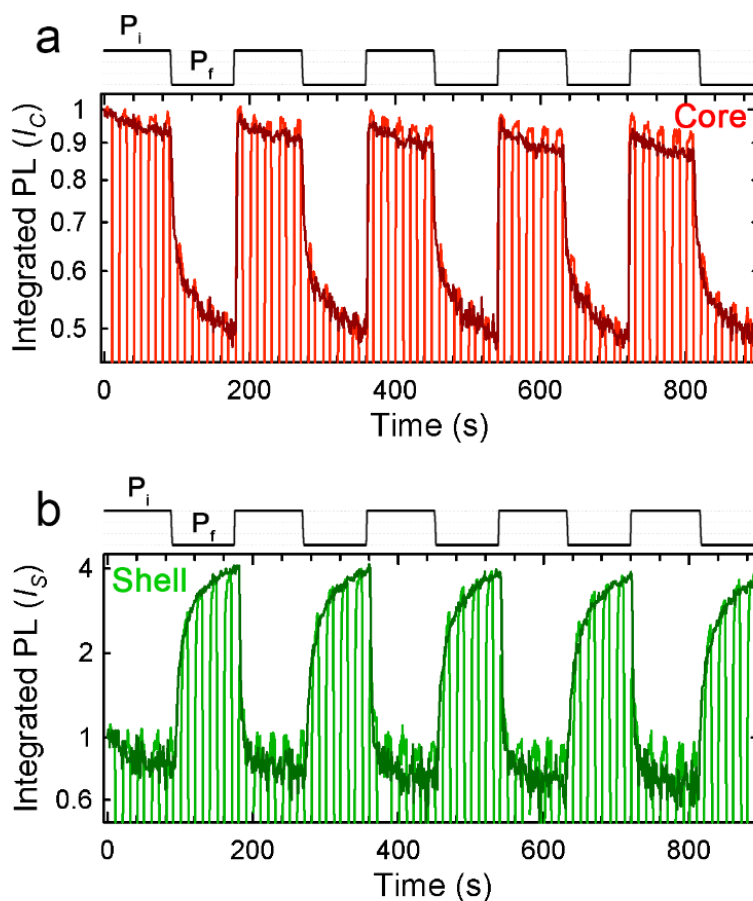


Figure 3.14. **Stability tests under continuous and intermittent UV illumination.** Integrated PL intensity of (a) core (I_c , red line) and (b) shell (I_s , green line) during On/Off pressure cycles from atmospheric oxygen pressure ($P_i=1$ bar) down to $P_f=10^{-3}$ bar collected under continuous (darker lines) or intermittent (lighter lines) illumination. All measurements are carried out at room temperature using 400 nm excitation; 1s acquisition time; each pressure step lasts 90 s.

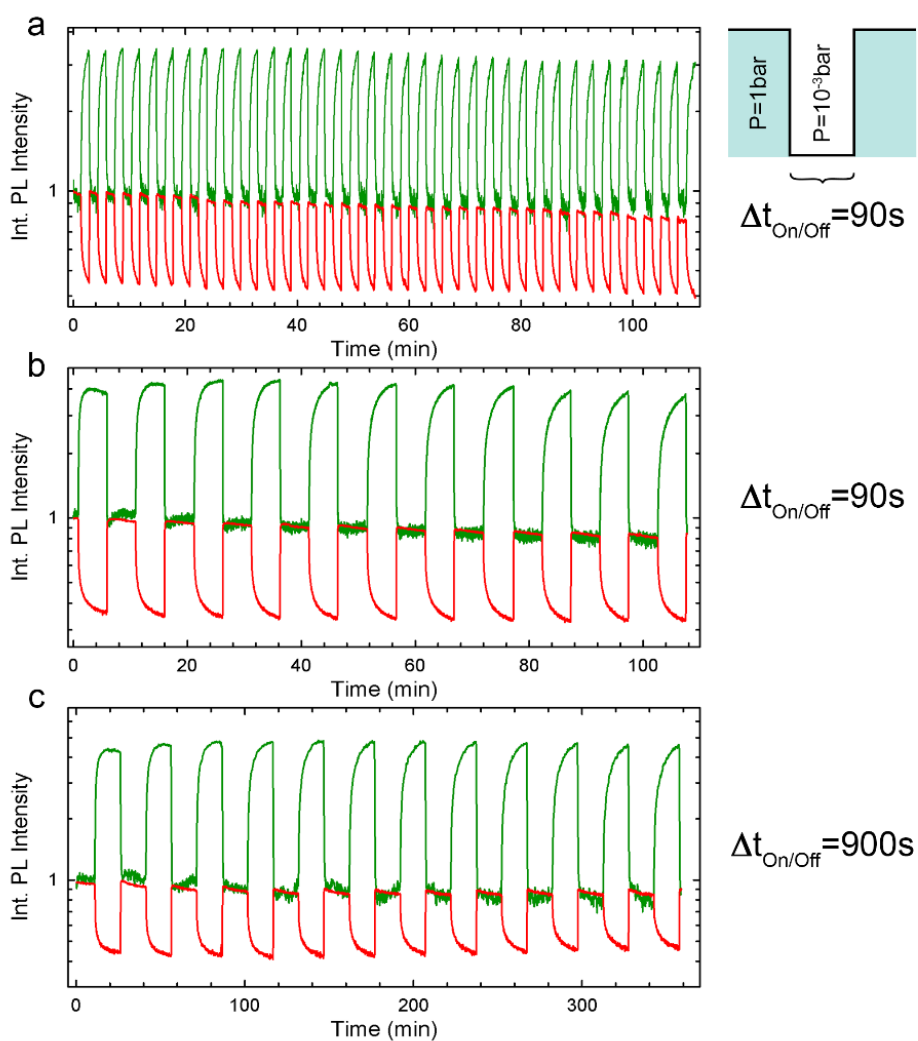


Figure 3.15. **Ratiometric sensing response over extended cycling.** (a) Spectrally integrated core (red line) and shell (green line) PL intensities during multiple consecutive cycles between atmospheric pressure ($P=1\text{ bar}$) and reduced pressure ($P=10^{-3}\text{ bar}$). The ratiometric sensing performance of a sample of DiB NCs is investigated for 2 hours with 90 s 'On/Off' intervals under continuous UV illumination. No intensity quenching is observed due to continuous exposition to UV light; the sensing capability is completely recovered after each cycle and shows

full repeatability over many consecutive pressure changes. (b) Spectrally integrated core (red line) and shell (green line) PL intensities during many consecutive cycles between atmospheric pressure ($P=1$ bar) and reduced pressure ($P=10^{-3}$ bar). The ratiometric sensing performance of a sample of DiB NCs is investigated using 5 minutes for each step (atmospheric pressure or reduced pressure), resulting in 2 hours of consecutive sensing with no losses of either the core or the shell signals, and thus, no loss of sensing capability. (c) Spectrally integrated core (red line) and shell (green line) PL intensity during many consecutive cycles between atmospheric pressure ($P=1$ bar) and reduced pressure ($P=10^{-3}$ bar). The ratiometric sensing performance of a sample of DiB NCs is investigated using 15 minutes for each step (atmospheric pressure or reduced pressure), resulting in 6 hours of consecutive sensing with no intensity quenching in either the core or the shell emission. All measurements are performed at room temperature using 3.1 eV excitation.

A perfect overlap between the PL trends is also found for the core emission excited at 532 nm (2.33 eV) as shown in Figure 3.16.

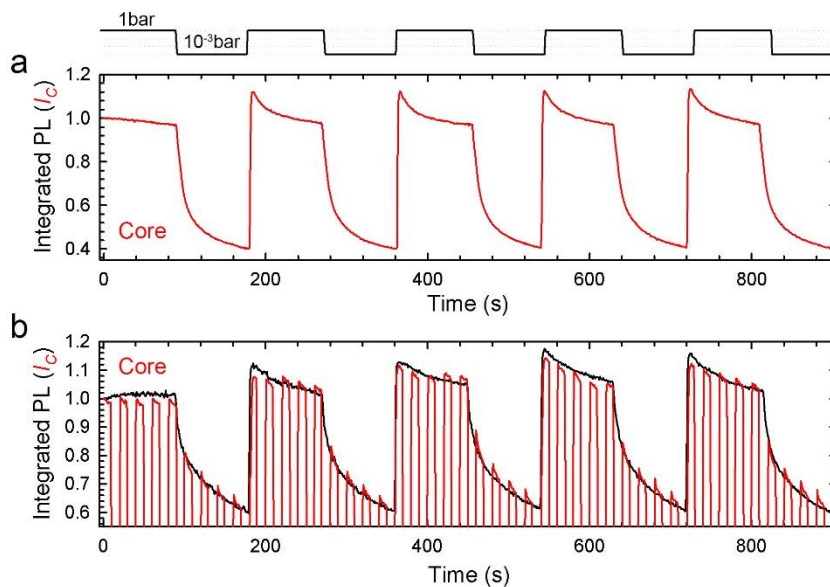


Figure 3.16. **Effects of core-only excitation on core O_2 -sensing response.** (a) Integrated PL intensity of CdSe core emission of 1.5/8.5 CdSe/CdS DiB NCs

during On/Off pressure cycles between $P=1$ bar and $P=10^{-3}$ bar, with 2.33 eV continuous wave excitation. The black line on top of the graph indicates the corresponding pressure values. (b) Overlap of two consecutive PL measurements consisting of On/Off pressure cycles between $P=1$ bar and $P=10^{-3}$ bar, one recorded under continuous excitation (black line) and the other alternating 10 seconds of 2.33 eV illumination and 10 s of dark, while the pressure cycling continued independently (red line). The 'Light On/Off' cycles perfectly overlap with the 'Light On' cycles. All measurements are carried out at room temperature using continuous wave 2.33 eV excitation; 1 s acquisition time, 90 s pressure steps.

3.2.3 Effect of tuning the core and shell relative sizes

We then proceeded to investigate in greater detail the dot-in-bulk paradigm role in the double sensing mechanism by synthesizing and analysing different core/shell CdSe/CdS heterostructures, featuring a slight modification of the respective core and shell sizes, in order to show how a fine-tuning of the heterostructure is pivotal in reaching a distinct sensing capability. Specifically, we synthesized and studied two samples of DiB NCs, whose total diameter is the same of our reference DiB heterostructures, (20 nm), but with different core/shell sizes, namely: 1 nm CdSe core radius and 9 nm CdS shell size, and 3 nm CdSe core radius with 7 nm CdS shell size. A sample of thin-shell CdSe/CdS NCs with 1.5 nm core radius and 3 nm shell size is also used in order to compare the heterostructuring with only a few CdS monolayers to the presence of a thick CdS shell, which is peculiar to the DiB motif. Moreover, we push the DiB paradigm to both its extremes, that is, we compare the behavior of DiB samples to that of their isolated components, 'core-only' CdSe NCs (1.5 nm radius) and 'shell-only' CdS NCs (10 nm radius), in order to investigate the behaviour of both isolated semiconductors.

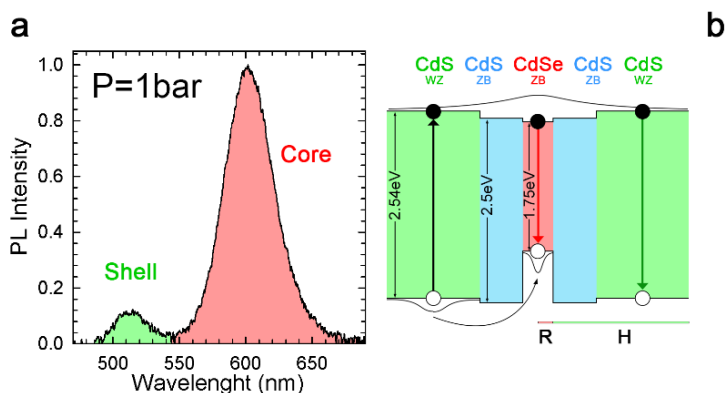


Figure 3.17. **Optical properties of 1CdSe/9CdS NCs.** (a) Normalized photoluminescence (PL) spectrum of a CdSe/CdS NCs sample with 1-nm core radius and 9-nm shell thickness at atmospheric oxygen pressure ($P=1$ bar), showing core and shell emission bands (highlighted by red and green shading, respectively). (b) An approximate band diagram of 1CdSe/9CdS DiB NCs, featuring the ZB-CdS interlayer (~ 3.5 nm) between the ZB CdSe Core and the WZ CdS shell. The measurement is performed at room temperature using 3.1 eV excitation.

We start our analysis with the 1CdSe/9CdS NCs, whose PL is reported in Figure 3.17a. Both shell and core excitons are emitting under low excitation fluence ($5\mu\text{J}/\text{cm}^2$, 400 nm excitation wavelength), as expected by the presence of a sharp interface that enables simultaneous emission from both states as discussed above (see band diagram in Figure 3.17b). The 1CdSe/9CdS DiB NCs exhibit more intense shell PL than the systems with the 1.5 nm CdSe core samples, which can be ascribed to the larger volume of the CdS shell, as well as a blue/shifted core PL. We proceed by testing their oxygen sensitivity by monitoring their PL intensity during many O_2 /vacuum cycles in which the sample chamber is kept at atmospheric pressure ($P=1$ bar) for 90 s and then rapidly evacuated to 10^{-3} bar for 90 s, and filled again to 1bar for five consecutive cycles. Figure 3.18 shows the integrated intensity of the core and shell emission bands while undergoing the pressure cycling.

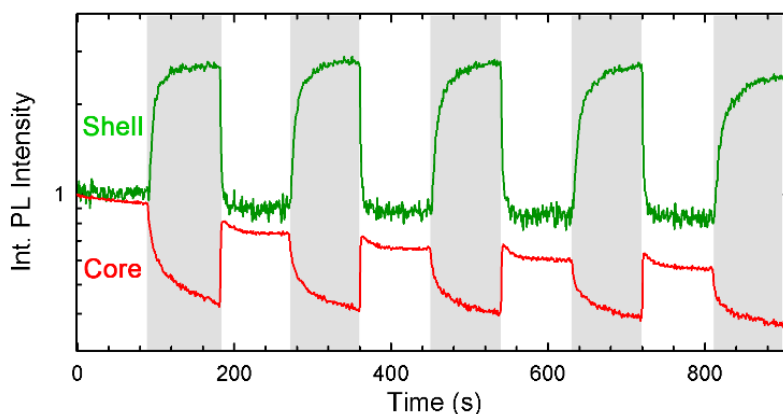


Figure 3.18. **Ratiometric O₂-sensing response of 1CdSe/9CdS NCs.** Integrated PL intensities of core (red line) and shell (green line) emissions during O₂/vacuum cycles, starting from atmospheric pressure ($P=1$ bar, no shade) down to 10^{-3} bar (highlighted with a grey shade); 1 s acquisition time, 90 s pressure steps. The measurement is performed at room temperature using 3.1 eV excitation.

Despite the more intense shell PL intensity under the same excitation fluence, the O₂ response of 1CdSe/9CdS NCs is however slightly weaker than in the 1,5CdSe/8,5CdS sample ($\sim 200\%$ vs $\sim 300\%$ increase of the shell PL intensity, from $P=1$ bar to $P=10^{-3}$ bar), most likely due to the fact that shell electrons are less exposed to the NC surfaces due to the thicker shell. On the other hand, the photobrightening responses observed for the core emission are comparable ($\sim 60\%$, as observed in ref²⁵), indicating a similar tendency to form negative trions in vacuum conditions, which will be discussed in §3.2.5.

We perform the same analysis on the 3CdSe/7CdS NCs, starting from their PL spectrum under atmospheric pressure. Figure 3.19a clearly displays the effect of a larger core to the detriment of the CdS shell, with the expected red-shifted core luminescence and a very weak shell PL (magnified in the inset of Figure 3.19a), as expected due to its smaller volume (Figure 3.19b).

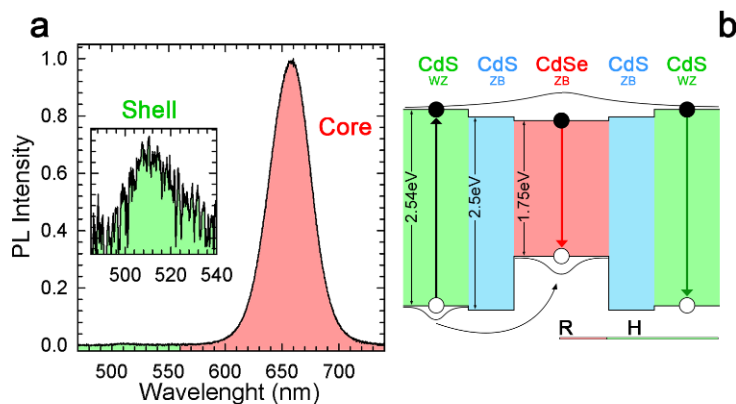


Figure 3.19. **Optical properties and ratiometric O_2 -sensing response of 3CdSe/7CdS NCs.** (a) Normalized PL spectrum of a CdSe/CdS NCs sample with a 3-nm core radius and a 7-nm shell thickness at atmospheric oxygen pressure ($P = 1$ bar), showing a core and a shell emission bands (highlighted by red and green shading, respectively). The inset is a magnified view of the shell emission. (b) An approximate band diagram of 3CdSe/7CdS DiB NCs, featuring the ZB-CdS interlayer (~ 3.5 nm) between the ZB CdSe Core and the WZ CdS shell. The measurement is performed at room temperature under 3.1 eV excitation.

The effect on the sensing response is reported in Figure 3.20, which shows the same measurement described for the 1CdSe/9CdS sample. The shell PL intensity is enhanced by only 100%, and the core emission decreased by $\sim 35\%$. This smaller effect of pressure on the core emission is in agreement with the inverse volume scaling of the Auger recombination rate, whose effect on the trion emission quantum yield in vacuum conditions becomes less detrimental compared to DiB NCs with a smaller core size, thereby making the oxygen-driven recovery process less significant to the enhancement of the PL under atmospheric pressure.

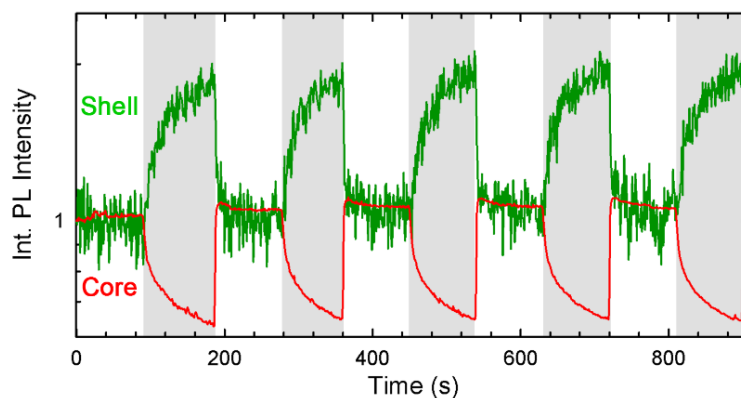


Figure 3.20. **Ratiometric O₂-sensing response of 3CdSe/7CdS NCs.** Integrated PL intensities of the core (red line) and the shell (green line) during O₂/vacuum cycles, starting from atmospheric pressure ($P = 1$ bar) down to 10^{-3} bar (highlighted with grey shades); 1 s acquisition time, 90 s pressure steps. The measurement is performed at room temperature under 3.1 eV excitation.

Figure 3.18 and Figure 3.20 highlight the reproducibility of the measurement under many O₂/vacuum cycles, which suggests that the sensing response is due to the filling/emptying of surface traps and not to permanent oxidation of the NC surfaces or damage to the capping ligands. This is also confirmed by the PL spectra of both 1CdSe/9CdS and 3CdSe/7CdS NCs under reduced pressure, as shown in Figure 3.21a,b.

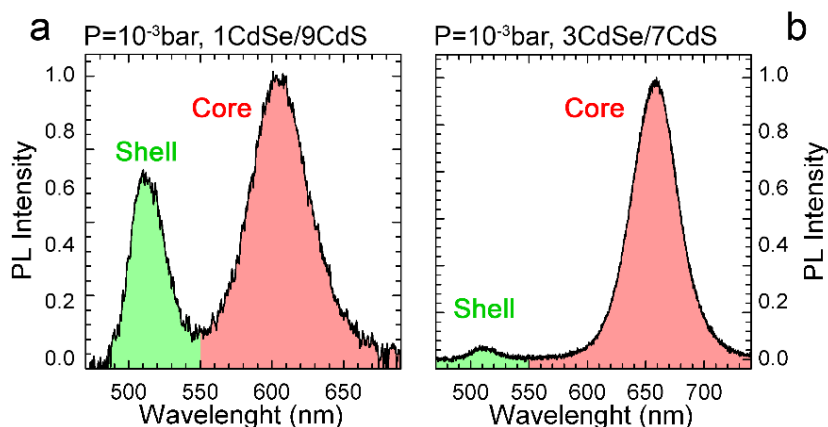


Figure 3.21. **Optical properties under reduced atmosphere of 1CdSe/9CdS and 3CdSe/7CdS NCs.** Normalized PL spectrum of a CdSe/CdS NCs sample with (a) a 1-nm core radius and a 9-nm shell thickness and (b) a 3-nm core radius and a 7-nm shell thickness under reduced oxygen pressure ($P = 10^{-3}$ bar), showing core and shell emission bands (highlighted by red and green shading, respectively). Both measurements were performed at room temperature, under 3.1 eV excitation.

In order to demonstrate that the DiB concept is crucial to the double-sensing mechanism, we perform the same set of measurements shown for the 1CdSe/9CdS and 3CdSe/7CdS samples also for core/shell NCs with a 3 nm only thick CdS shell and a 1.5 nm radius CdSe core. Their PL spectrum only shows emission from core states (Figure 3.22a). However, as reported both for the step-like measurement in Figure 3.22b and for the O_2 /vacuum cycling in Figure 3.22c, the core response is markedly stronger than that observed for thicker shell NCs due to more efficient nonradiative Auger decay of trion states at low pressure in thinner shell NCs. Note that all these NCs have unalloyed (i.e., "sharp") core/shell interfaces.

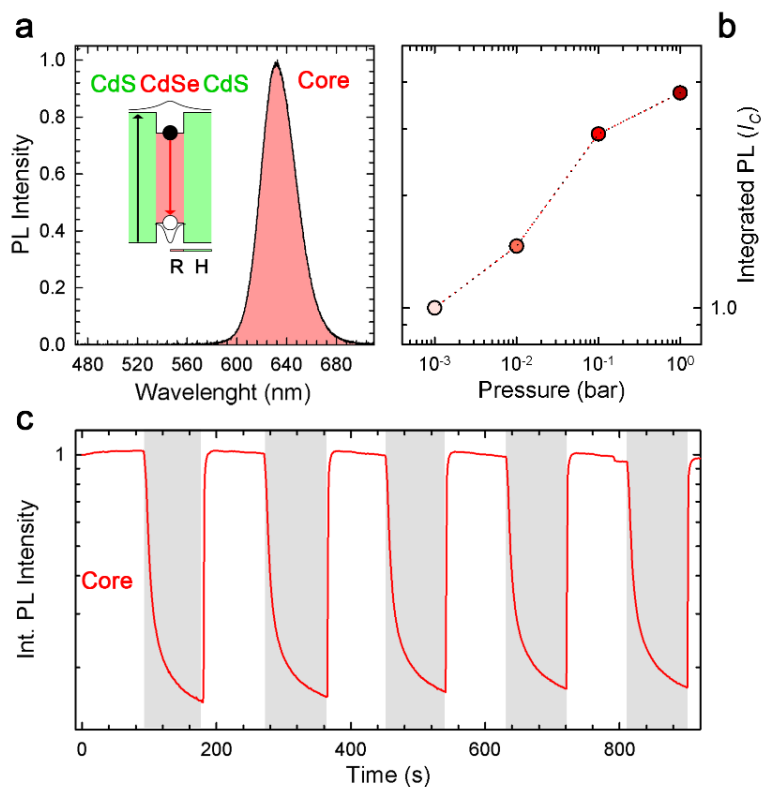


Figure 3.22. **Optical properties and O₂-sensing response of 1.5CdSe/3CdS NCs.** (a) Normalized PL spectrum of a CdSe/CdS NCs sample with 1.5-nm core radius and 3-nm shell thickness (in zincblende structure) at oxygen pressure $P=1$ bar. Inset: approximate band diagram of 1.5CdSe/3CdS NCs. (b) Integrated core PL intensity, I_C , as a function of increasing pressure normalized to its value at $P=10^{-3}$ bar (logarithmic scale). (c) Integrated core PL intensity during O₂/vacuum cycles, starting from atmospheric pressure ($P=1$ bar) down to 10^{-3} bar (highlighted with a grey shading). 1 s acquisition time, 90 s pressure steps. All measurements are performed at room temperature under 3.1 eV excitation.

In order to provide a more direct comparison between the three samples following the DiB paradigm, in Figure 3.23a we report the results of a measurements performed in the same conditions for the 1CdSe/9CdS, 1,5CdSe/8,5CdS and 3CdSe/7CdS NCs. For the three NCs, we monitored the PL intensity of the core and the shell in a step-like measurement, starting from

$P=1$ bar and lowering the oxygen pressure one order of magnitude at a time, down to 10^{-3} bar. Figure 3.23a displays the data for the three samples normalized at their respective values at the lower pressure ($P=10^{-3}$ bar). The same scale is used in order to highlight the difference between the samples. The core luminescence show a 120% increase in both 1,5/8,5 and 1/9 samples, and a limited increase (50%) in 3/7 NCs. The most extended shell variation is reported for 1,5/8,5 NCs (-75%), whereas its tuning is reduced in 1/9 and 3/7 samples for the reasons explained above (-63% and -45%, respectively). The different extent of the core and shell variations consequently affects the overall sensing capability, which is limited for the heterostructures with a smaller (1/9, +500%) and larger (+180%) core size. A practical way to visualize the same results is by plotting them onto a CIE diagram. Figure 3.23b highlights both the different extents of the sensing response in the three samples and the difference in the resulting overall color coming from a fine tuning of the core size (and core exciton energy and emission wavelength, ranging from 597nm, to 628nm, to 658 nm from 1/9, 1,5/8,5 and 3/7 CdSe/CdS NCs, respectively) with respect to the bulk-like character of the shell (maximum emission at ca 510nm for all the three samples). Furthermore, the sensing response of all three samples can be rationalized in term of a Stern-Volmer model. The two-site Stern-Volmer analysis described in §3.2.2 successfully fits the overall sensing response (I_c/I_s) for all the three samples. The corresponding Stern-Volmer coefficient ($k_{SV,1}$ and $k_{SV,2}$) we obtain finely mirror the sensing capabilities of the NCs set: $k_{SV,1}$ values are 0.3 bar^{-1} , 1.26 bar^{-1} and 0.25 bar^{-1} while $k_{SV,2}$ values are 280 bar^{-1} , 299 bar^{-1} and 250 bar^{-1} for 1CdSe/9CdS, 1.5CdSe/8.5CdS and 3CdSe/7CdS NCs, respectively.

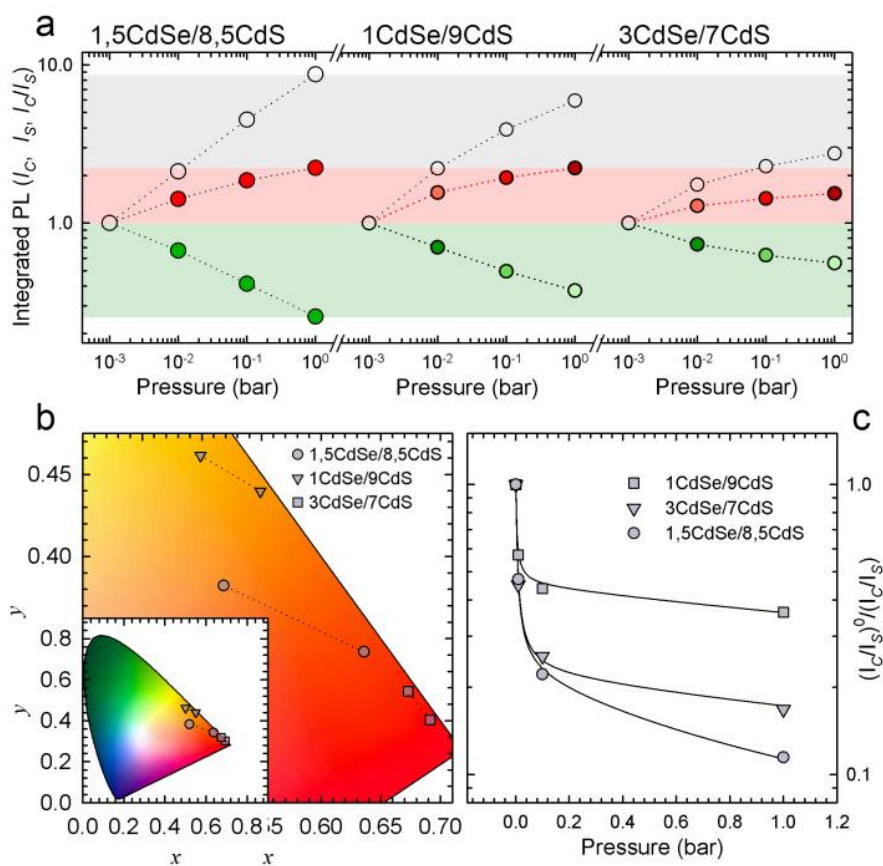


Figure 3.23 **Comparison of O₂ sensing response of different core/shell sized DiB NCs.** (a) Integrated PL intensities of the core (I_c , red dots) and the shell (I_s , green dots), together with their ratio (I_c/I_s) as a function of increasing pressure (logarithmic scale) from $P=10^{-3}$ bar to $P=1$ bar, for the three DiB samples, namely: 1,5CdSe/8,5CdS NCs (left), 1CdSe/9CdS NCs (center), and 3CdSe/7CdS NCs (right). All trends are normalized to their respective value at $P=10^{-3}$ bar (I_c^0 and I_s^0 , respectively). (b) overall emission color of a NC film for the three DiB samples extracted from the respective PL spectra, projected onto the CIE chromaticity diagram. For each sample, the color at $P=1$ bar and $P=10^{-3}$ bar is reported. (c) Stern-Volmer plot of the total ratiometric O₂-response of 1CdSe/9CdS, 1,5CdSe/8,5CdS and 3CdSe/7CdS NCs, reported as $(I_c/I_s)^0/(I_c/I_s)$ as a function of the O₂ partial pressure p_{O_2} , for a pressure range from $P=10^{-3}$ bar to $P=1$ bar. The experimental data have been adequately fitted with the Stern-Volmer equation

applying the two-site model. The Stern-Volmer constants of the two sites are: $k_{SV,1} = 0.3 \text{ bar}^{-1}$, 1.26 bar^{-1} and 0.25 bar^{-1} and $k_{SV,2} = 280 \text{ bar}^{-1}$, 299 bar^{-1} and 250 bar^{-1} for 1CdSe/9CdS, 1.5CdSe/8.5CdS and 3CdSe/7CdS NCs, respectively. All measurements were performed at room temperature using 3.1 eV excitation.

Finally, we perform the same measurements also for core-only and shell-only samples (Figure 3.24a,b), in order to explore their behavior separately. We start by monitoring the PL efficiency of the 1.5-nm core-only CdSe NCs sample while keeping it for 90 s under atmospheric pressure ($P=1\text{bar}$) and 90 s at reduced pressure ($P=10^{-3}\text{bar}$), as reported in Figure 3.24c. They start by showing low intensity PL due to their poor QY of <5%, caused by highly efficient non-radiative surface-related recombination typical of unshelled NCs. The oxygen sensitivity is therefore very weak since the high surface/volume ratio leads to a negligible sub-population of charged NCs, which are responsible for the PL quenching under reduced pressure conditions. This is in agreement with the fluorescence data in vacuum at low temperature reported by Nirmal M. *et al.*²⁵², showing the characteristic dark state decay from neutral excitons, and with the fluorescence line narrowing (FLN) data reported in⁽²⁰⁰⁾.

On the other hand, giant shell-only CdS NCs have higher PL quantum yield and provide good sensitivity to O_2 pressure. While going from $P=1\text{bar}$ to $P=10^{-3}\text{bar}$, their PL intensity shows a 50% increase. The underpinning mechanism is essentially the same as the one described for the shell excitons in 1.5/8.5 DiB NCs: under reduced pressure conditions, the electron scavenging effect of O_2 molecules is minimized, leading to a higher PL quantum yield.

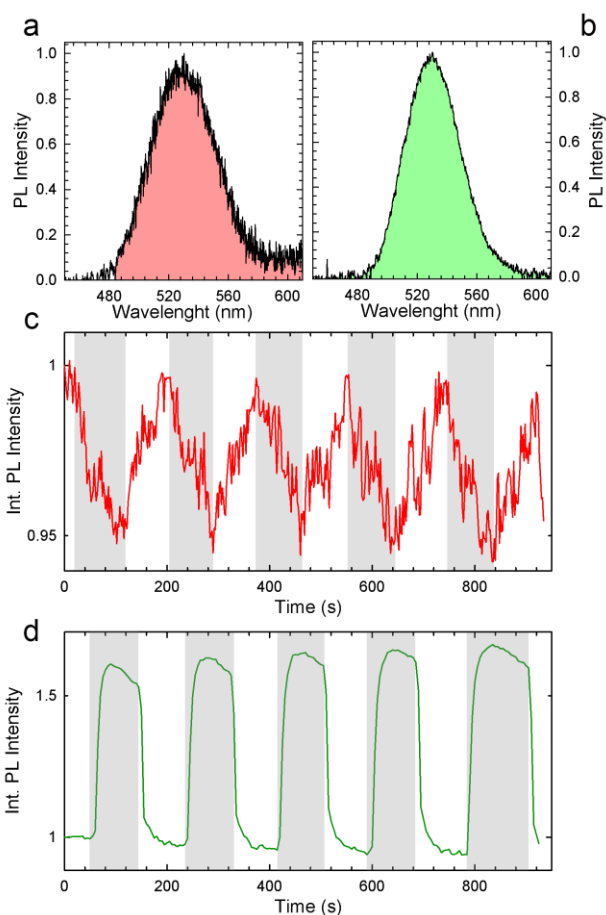


Figure 3.24. **Optical properties and O₂-sensing response of core-only 1.5CdSe and shell-only 10CdS NCs.** (a) Normalized PL spectrum of a CdSe NCs sample with 1.5-nm radius at oxygen pressure ($P=1$ bar). (b) Normalized PL spectrum of a CdS-NC sample with a 10-nm NC radius at oxygen pressure $P = 1$ bar. (c) Integrated PL intensity during O₂/vacuum cycles, starting from atmospheric pressure ($P=1$ bar) down to 10^{-3} bar (highlighted with a grey shading). 1 s acquisition time, 90 s pressure steps. (d) Spectrally integrated PL intensity, I_S , during O₂/vacuum cycles, starting from atmospheric pressure ($P = 1$ bar) down to 10^{-3} bar (highlighted with a grey shading); 1 s acquisition time, 90 s pressure steps. All measurements are performed at room temperature using 3.1 eV excitation.

3.2.4 Single particle ratiometric oxygen sensing using DiB NCs

As we show below, an important feature of DiB NCs is that they behave as ratiometric pressure sensors even at the single-NC level, which makes them capable of reporting O_2 pressure variations with nanoscale spatial resolution. This represents a unique advantage over PSPs based on chromophores blends and simplifies the paint processing by removing issues associated with the inhomogeneous distribution of the emitters on the model surfaces or in the binder, the factors that typically reduce the spatial accuracy in sub-micron-scale pressure studies²⁴⁶.

The ratiometric sensing ability of individual DiB NCs is demonstrated in Figure 3.25, where we show confocal imaging and micro-PL data of isolated NCs (drop casted from a diluted hexane solution onto a quartz substrate with a nominal NC density of $\sim 0.1/\mu\text{m}^2$) as a function of the O_2 pressure. Upon raising the pressure from 10^{-3} bar to 1 bar, all NCs show a progressive transition in their emission colour from green, to orange, and then red, which is in perfect agreement with the results of ensemble measurements (Figure 3.10b).

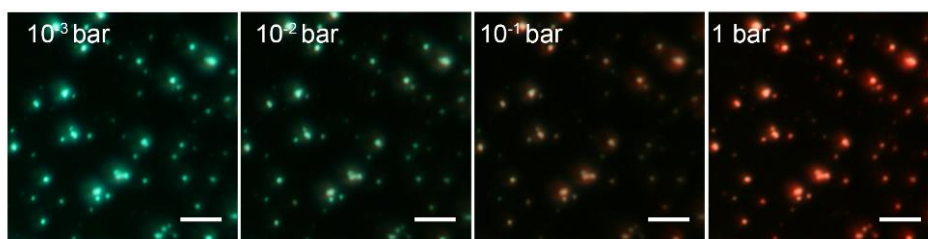


Figure 3.25. **Single particle ratiometric oxygen sensing of DiB NCs.** A large-area spectrally resolved image of a collection of individual DiB NCs as a function of the O_2 pressure under 400 nm excitation (excitation fluence $7\mu\text{J}/\text{cm}^2$), showing a progressive change of the emission colour from green to red upon increasing the chamber pressure. The scale bar corresponds to $5\mu\text{m}$.

Figure 3.26a reports the histogram of the I_C/I_S ratio for 40 individual DiB NCs as a function of the chamber pressure, showing remarkable homogeneity of the ratiometric response across the NC population. This indicates that individual DiB NCs can indeed be used as highly accurate nanoscale ratiometric pressure (or O_2) sensors. Importantly, the ratiometric sensing response I_C/I_S is independent of the

total emission intensity, as highlighted in the correlation plot of I_C/I_S vs. (I_C+I_S) in Figure 3.26b.

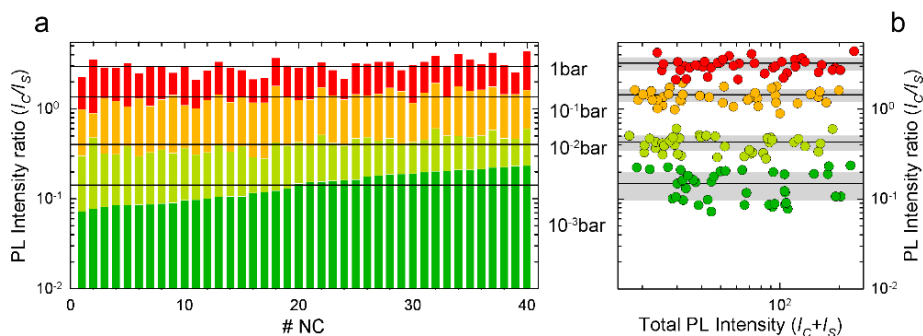


Figure 3.26. **Analysis of the single-particle ratiometric response of DiB NCs.** (a) Histogram of the single-particle ratiometric response expressed as I_C/I_S for 40 individual NCs at the monitored oxygen pressures. (b) Correlation plot of the ratiometric sensing response I_C/I_S vs. the total PL intensity (I_C+I_S) at increasing O_2 pressure, indicating that the sensing response is independent of the total emission intensity. The same colour code applies to all panels and resembles the total emission colour of the NCs: 10^{-3} bar, dark green; 10^{-2} bar, light green; 10^{-1} bar, orange; 1 bar, red. The mean values averaged across the whole NC population are indicated with black solid lines; the respective standard deviations are shown by grey shading.

3.2.5 Photophysical mechanisms of the double sensing response

In order to gain a deeper insight into the photophysical mechanisms underpinning the ratiometric sensing response of DiB-NCs, we have measured the decay dynamics of both the shell and the core luminescence in a controlled atmosphere (Figure 3.27a,b). We start our analysis with the reversed pressure response of the core luminescence, which is key for the realization of the ‘double sensing’ regime. Examining the core time-resolved PL traces in Figure 3.27a we note a $\sim 20\%$ increase of the zero-delay PL intensity with decreasing pressure from 1 bar to 10^{-3} bar, which is accompanied by the acceleration of the decay dynamics. These are the typical spectroscopic signatures of the recombination of charged excitons (trions) consisting of a photoexcited electron-hole pair and a pre-existing carrier (in the case of CdSe/CdS NCs it is predominantly an electron^{212, 213, 253}) produced

by photoionization^{79, 214}. In atmospheric conditions (Figure 3.28a), molecular oxygen continuously removes excess electrons thereby hindering the formation of negative trions. As a result, spectroscopic behaviour of DiB NCs are dominated by neutral excitons. If these excitons are core-localized they are virtually unaffected by surface species due to the protective effect of the ultra-thick CdS shell. Upon evacuation, the oxygen-driven "discharging" process is gradually suppressed, resulting in the formation of negative trions. These species are characterized by an increased emission rate (it is ideally twice that of a neutral exciton), which can explain the increase in the early time PL amplitude observed upon reducing the amount of oxygen in the sample chamber.

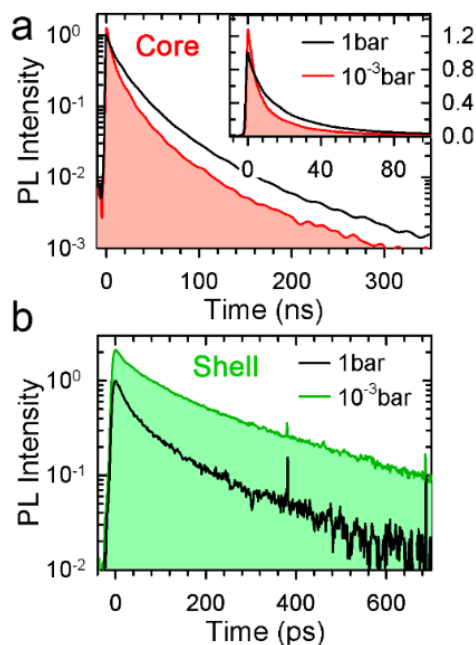


Figure 3.27. **Photophysical mechanism of the dual sensing response.** PL decay curves of (a) core and (b) shell emission measured at $P=1$ bar (red and green lines, respectively) and $P=10^{-3}$ bar (black lines). The inset in 'a' reports the decay curve of the core PL using a linear scale to highlight the increase in the intensity at zero delay time as well as the accelerated decay exhibited at low O_2 pressure.

In addition, we observe the reduction of the PL lifetime, which is due to a combined effect of the enhanced radiative decay and the activation of nonradiative Auger recombination. In DiB NCs with a sharp core/shell interface, the Auger process is not as strongly suppressed as in graded or interfacially alloyed thick-shell CdSe/CdS NCs that could exhibit nearly unity triion PL quantum yields^{254, 255}. As a result, the dominant decay channel for the core PL in the absence of O₂ is nonradiative Auger recombination of negatively charged excitons (Figure 3.28b).

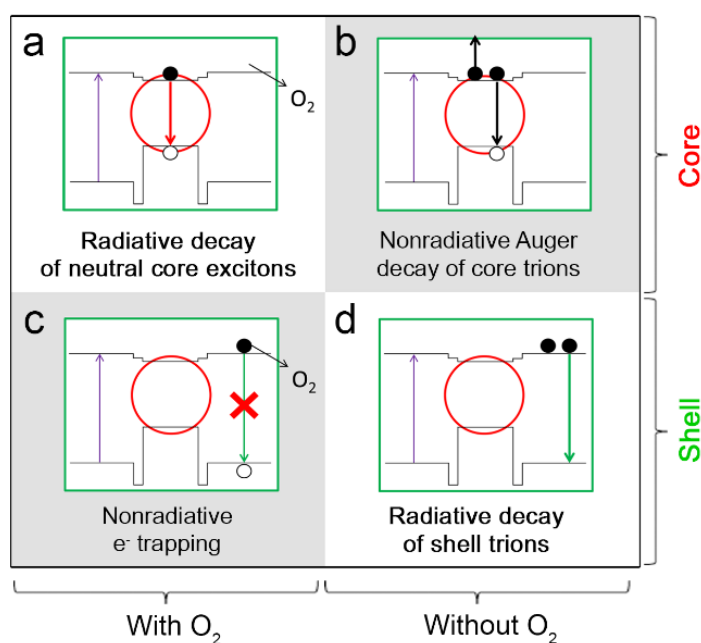


Figure 3.28. **Schematics of the DiB NC-O₂ interaction leading to the observed optical responses.** In the presence of O₂, neutral core excitons recombine radiatively (b), whilst the shell-exciton decay is affected by nonradiative electron processes (c) involving either direct electron extraction by O₂ molecules or trapping at surface defects depleted of electrons due to interactions with O₂. In the absence of O₂, enhanced availability of excess electrons makes nonradiative Auger decay the dominant recombination pathway for negatively charged core excitons (f), while shell excitons decay radiatively (e) thanks to impeded electron capture by O₂ and suppressed Auger recombination; the latter is diminished due

to a large volume of the shell. The regimes dominated by nonradiative recombination are highlighted by grey shading.

The formation of negative trions in NC samples under vacuum is confirmed by circular polarization-resolved PL measurements in high magnetic fields reported in Figure 3.29a-c.

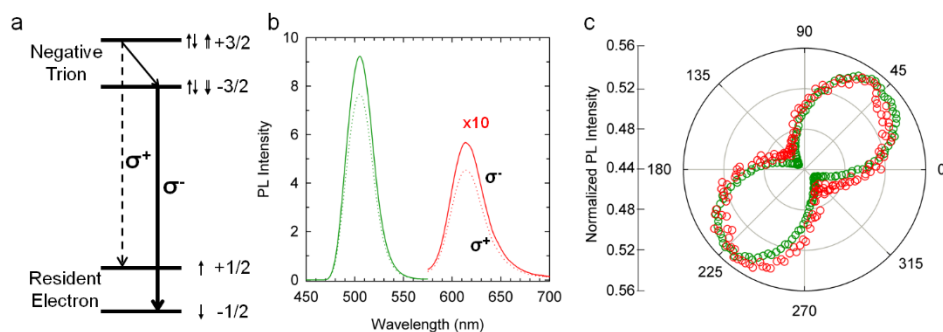


Figure 3.29. **Circular polarization resolved photoluminescence of DiB NCs at low temperature and high magnetic fields.** (a) Energy levels scheme of the radiative recombination of core negatively charged excitons in 1.5/8.5 CdSe/CdS DiB NCs. The initial state is featured by two coupled electrons in the $1S_e$ conduction band state (antiparallel arrows) and one hole in the $1S_{3/2}$ valence band state (bold arrow), and hence by $M = \pm 3/2$. On the contrary, one single resident electron in the conduction band forms the final state, which is characterized by $M = \pm 1/2$. The selection rule $\Delta M = \pm 1$ and the total angular momentum conservation law imply that the allowed recombination mechanisms are $-3/2 \rightarrow -1/2$ and the $+3/2 \rightarrow +1/2$ and involve the emission of counter-clockwise (σ^-) and clockwise (σ^+) polarized photons, respectively. (b) Circularly polarized core (red curves) and shell (green curves) emission at $B = 5$ T and $T = 3$ K. The higher σ^- polarized PL intensity is due to stabilization of the $M = -3/2$ spin sublevel in presence of external magnetic fields. (c) Normalized PL intensities as a function of the angle between the fast axis of the quarter wave plate and the polarization axis of the linear polarizer used to investigate the emitted photon handedness. The normalization constant is the sum of the maximum and minimum PL intensity, i.e. the sum of σ^+ - and σ^- -polarized PL, $I^+ + I^-$.

This data shows that, similarly to giant core/shell CdSe/CdS nanocrystals and core/shell CdSe/CdSe nanoplatelets, magneto-PL from DiB NCs exhibits circular

polarization typical of negatively charged excitons^{214, 256}. We note that O₂/vacuum scans using core-selective excitation at 532 nm (2.33 eV) reported in Figure 3.16 show similar dimming of the core PL as that observed using 400 nm (3.1 eV) excitation, thereby unambiguously confirming that the sensitivity of core emission to O₂ is due only to nonradiative Auger recombination of core trions and not the depletion of the NC conduction band due to progressively more efficient shell emission observed for decreasing O₂ pressure.

Next, we investigate the effect of O₂ on the shell-PL dynamics. Since the thickness of the CdS shell (8.5 nm) is greater than the exciton Bohr radius in CdS (5.6 nm), the shell excitons are bulk-like and hence are virtually unaffected by Auger recombination. The rate of Auger decay scales inversely with the particle volume and, therefore, is expected to be over 300 times lower than in the 1.5 nm CdSe core²⁵⁷. As a result, even in the case of excess electrons, as indicated by circular polarization-resolved magneto-PL measurements in Figure 3.29, the nonradiative decay of shell excitons is primarily not due to Auger recombination, but still surface trapping (Figure 3.28c). Accordingly, upon lowering the chamber pressure, which is equivalent to raising the Fermi levels, leads to passivation of electron surface traps which is manifested in the strong increase of the zero delay PL intensity, accompanied by the extension of the PL lifetime (Figure 3.27b, Figure 3.28d). The resulting effect of these changes is the >300% enhancement of the emission intensity observed in cw measurements (Figure 3.8b). This confirms that the shell-PL dynamics is dominated by activation/suppression of electron capture either directly by O₂ or electron-deficient surface traps. This further points to the co-existence of two trapping processes occurring on two different timescales: (i) ultrafast electron capture with the characteristic time unresolvable in our measurements with ~6 ps resolution (streak-camera detection), thereby modulating the zero-delay PL intensity without affecting its temporal dynamics, and (ii) a slower electron trapping channel competing with radiative recombination of shell excitons, whose progressive suppression at decreasing pressure leads to slower PL dynamics^{24, 176}.

3.2.6 Ratiometric sensing response with different gases and pressure

Further evidence of the dominant effect of oxygen on the PL intensity of core and shell excitons is provided by On/Off pressure cycling with other gases, as reported in Figure 3.30 and Figure 3.31.

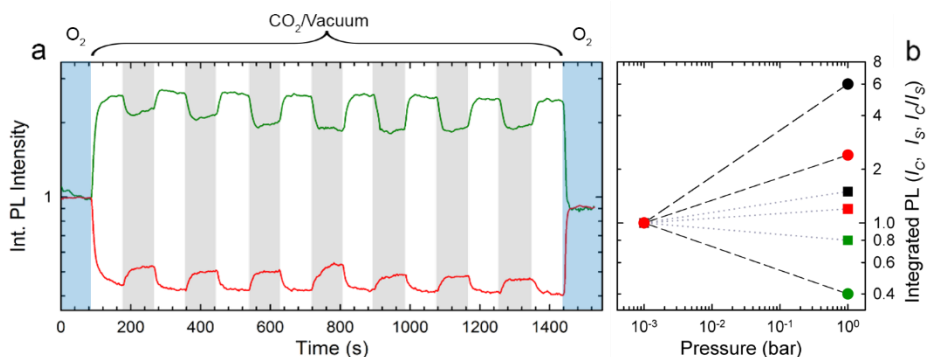


Figure 3.30. **Ratiometric sensing response of DiB NCs to carbon dioxide.** (a) Spectrally integrated PL intensity of DiB NCs during 'On/Off' gas/vacuum cycles. The scan starts with 90 s at $P=1$ bar in O₂ (blue shaded areas), after which the chamber is evacuated to 10⁻³ bar. After 90 s, the chamber is filled with CO₂, purity grade 4.5 (≥ 99.995 Vol. %), up to $P=1$ bar (grey shaded areas). After 90 seconds, the chamber is evacuated again and later refilled with CO₂ for seven consecutive cycles in order to assess the reproducibility of the response. After the seventh cycle in CO₂, the chamber is filled with O₂ ($P=1$ bar) in order to measure the response to oxygen in the same measurement as for CO₂. The measurement is performed at room temperature under 3.1 eV excitation. Both the shell (green line) and the core (red line) responses are normalized to their respective value at 10⁻³ bar pressure (I_C^0 and I_S^0 respectively). (b) The I_C (red symbols), I_S (green symbols) and I_C/I_S (black symbols) values for extracted from 'a' for O₂/vacuum response (circles) and CO₂/vacuum response (squares).

Specifically, the PL intensity of both the core and the shell was recorded while filling the sample chamber with CO₂ (Figure 3.30a,b) and humid air (Figure 3.31).

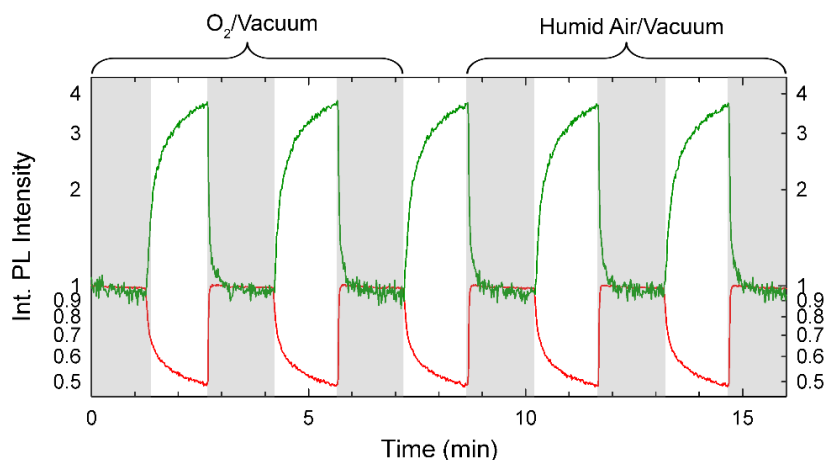


Figure 3.31. **Ratiometric sensing response of DiB NCs to humid air and oxygen.** Spectrally integrated PL intensity of DiB NCs during 'On/Off' O₂/vacuum cycles (first three cycles) and humid-air/vacuum cycles (second three cycles) starting from O₂ (P=1 bar, highlighted with grey shading) down to P=10⁻³ bar. After the first three cycles, the chamber is evacuated and refilled with humid air for three consecutive cycles, while continuously monitoring the PL. The absolute humidity is 20.5 g/kg, corresponding to common ambient conditions in which sensing varnishes could be employed (i.e. about 85% humidity at room temperature). The measurement is performed at room temperature under 3.1 eV excitation.

The ratiometric double sensing response is also observed upon exposure of the NCs to CO₂, although with a weaker sensitivity than in the case of oxygen due to a weaker reactivity of CO₂. This observation suggests that DiB-NCs can also be applied as environmental gas sensors. Furthermore, data indicate (Figure 3.31) that the sensing response to wet air is similar to that observed for dry O₂, which suggests that humidity has a negligible effect on the PSP behavior. This extends the potential use of DiB-NCs as gas flow sensors in ambient conditions, without distortions due to variations in humidity.

Finally, a simple adjustment of our setup allowed us to monitor the sensing behavior of DiB NCs in overpressure conditions, that is, while increasing the oxygen pressure in the sample chamber from P=1bar to P=2bar (Figure 3.32a).

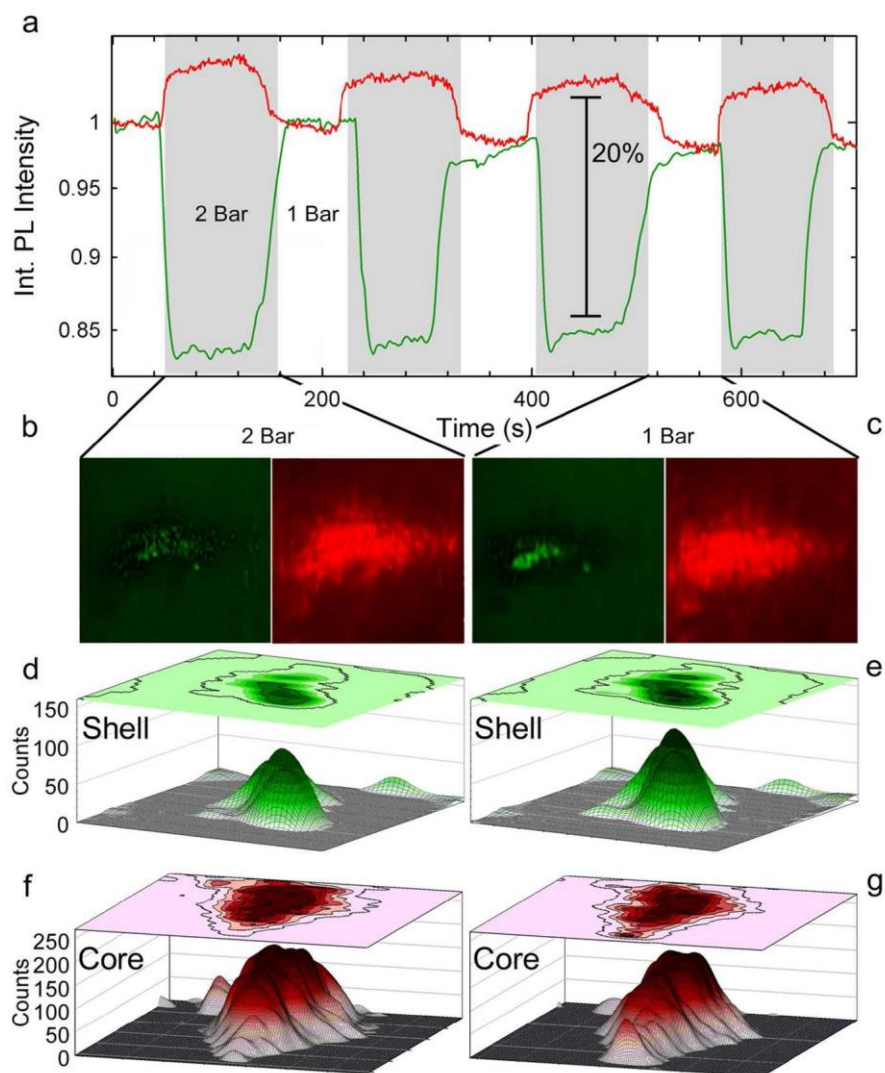


Figure 3.32. **Ratiometric sensing response of DiB NCs at oxygen pressure between 1bar and 2 bar.** (a) Spectrally integrated PL intensity of the 1.5/8.5 DiB NCs during cycles from atmospheric pressure up to 2 bar (highlighted with grey shading). (b) Photograph of a DiB NCs sample at P=2bar collected using the green (left panel) and red (right panel) channel of the CCD. (c) Photograph of a DiB NCs sample at P=1bar collected using the green (left panel) and red (right panel)

channel of the CCD. (d,e) 3D surface intensity plot of the shell emission extrapolated from the photographs collected using the green channel of the CCD showed in 'b' and 'c' respectively. (f,g) 3D surface intensity plot of the shell emission extrapolated from the photographs collected using the red channel of the CCD showed in 'b' and 'c' respectively. The data show that the increase of the pressure from 1 bar to 2 bar produces a ~15% dimming of the shell emission and a ~5% enhancement of the core emission, resulting in a ratiometric sensitivity of ~20%. The measurement is performed at room temperature using 400 nm excitation.

The results show a consistent ratiometric sensing capability that follows the trend observed in the measurements in vacuum and confirm that DiB-NCs can be used also in high pressure conditions. Together with the measurement, we provide a photographs of the system under atmospheric and increased pressure in order to highlight once again how the color change can be monitored with a simple RGB camera (Figure 3.32b-g).

3.2.7 Comparison between O₂ sensing and spectroelectrochemistry

Beside the applicative impact for pressure sensing, the whole body of photoluminescence and magneto-optical data as a function of pressure has a fundamental implication on the effect of vacuum in raising the Fermi energy of NCs, in nearly perfect analogy to what observed upon the application of a negative potential in spectro-electrochemical experiments⁷⁹.

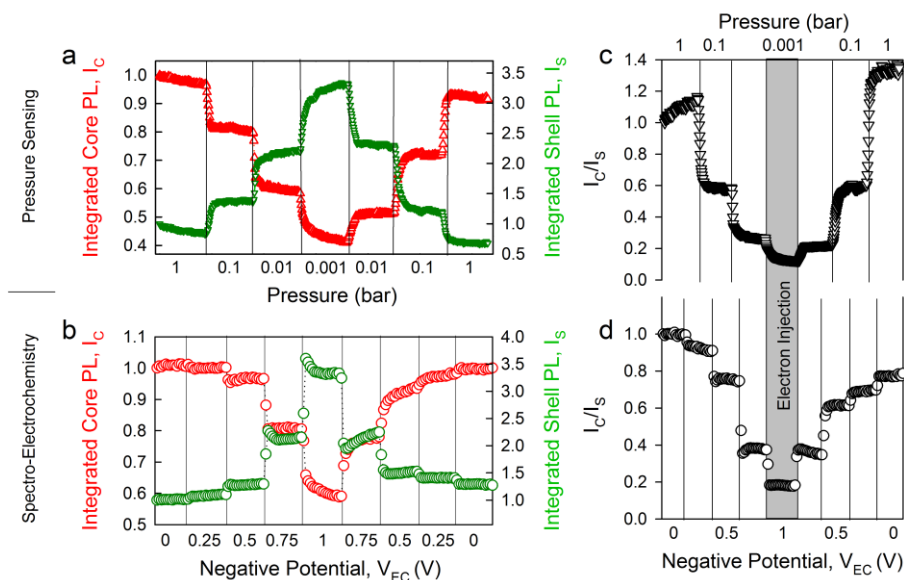


Figure 3.33. **Spectro-electrochemical modulation and Oxygen sensing response of DiB NCs.** (a) Integrated PL intensity of the core (I_C , red line) and the shell (I_S , green line) PL extracted from the stepwise pressure scan (1 s acquisition time per frame, 90 s steps). The pressure is reduced rapidly and kept constant for 90 s, starting from atmospheric pressure ($P=1$ bar) to 10^{-1} , 10^{-2} and 10^{-3} bar, after which the sample chamber is stepwise refilled up to the initial pressure level of $P=1$ bar. in 'a'. Both trends are normalized to the initial PL intensity values at $P=1$ bar. (b) The core (red circles; left axis) and the shell PL intensity (green circles; right axis) as a function of applied negative EC potential of a submonolayer film of DiB NCs ($R_0 = 1.5$ nm, $H = 8.5$ nm) deposited onto a ZnO-nanoparticle-covered layer of indium tin oxide (ITO); all intensities are normalized to their values at $V_{EC} = 0$ V. The respective ratiometric response I_C/I_S are reported in (c) and (d) respectively. The grey shaded area emphasizes the regime of direct electron injection in the NC's conduction band states that is achieved in both experiments.

Specifically, as obtained while lowering the oxygen pressure (Figure 3.33a) and as shown in Figure 3.33b, the application of a negative potential to DiB-NCs leads to the gradual increase of the shell emission and to the concomitant dimming of the core PL. At $V=-1$ V, the core PL dynamics shows the typical features of trion decay,

indicating direct injection of electrons in the NC conduction band states, according to the initial position of the Fermi level near the centre of the core energy gap (core band gap energy ~ 1.9 eV) as expected for undoped NCs (Figure 3.33c,d). This further confirms that the potential drop outside the NCs in the spectro-electrochemical measurements is essentially negligible leading to a one-to-one correlation between the applied potential and the position of the Fermi level (Figure 3.34a). The effect of vacuum on the NC's emission intensity and dynamics (Figure 3.8b and Figure 3.27a,b) shows a striking similarity with the electrochemically-induced modulation (Figure 3.34b,c) and highlights that the progressive removal of oxygen from the NC surroundings effectively leads to the gradual rise of the Fermi energy that eventually matches the position of the conduction band energy at $P=10^{-3}$ bar, resulting in direct injection of electrons in the NC quantized states and the consequent formation of negative core trions (Figure 3.29).

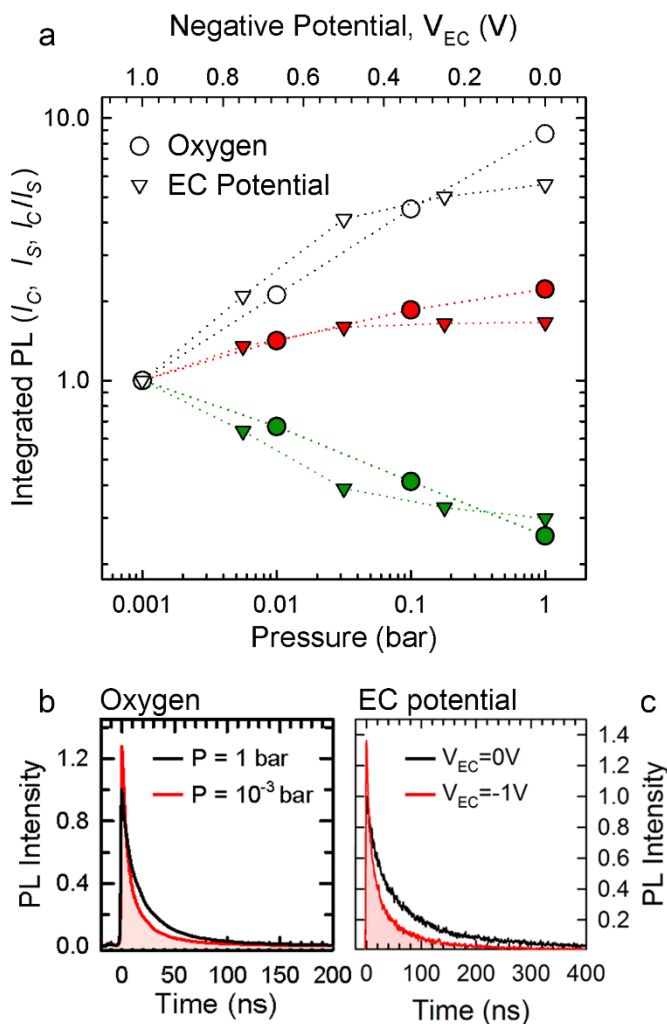


Figure 3.34. **Spectroelectrochemical and oxygen time-resolved sensing response of DiB NCs.** (a) The I_C and I_S values (red and green symbols, respectively) and the I_C/I_S ratio (white symbols) as a function of increasing pressure (circles, bottom axis) and of a decreasing negative potential (triangles, top axis, from $V_{EC}=-1$ V to $V_{EC}=0$ V). All trends are normalized to their respective value at $P=10^{-3}$ bar and $V_{EC}=-1$ V (I_C^0 and I_S^0 respectively). (b) Core decay under atmospheric pressure ($P=1$ bar, black line) and under $P=10^{-3}$ bar (red shaded area). (c) Core decay under $V_{EC}=0$ V (black line) and $V_{EC}=-1$ V (red shaded area).

A similar behaviour has been observed for CdSe/CdS nanoplatelets²⁴. Notably, the magneto optical data for DiB-NCs shown in Figure 3.29, further highlight that such effect is not limited to core states but affects also the shell excitons, leading to the formation of negative shell trions. The effect of the Fermi energy modulation on the dual color emission of DiB NCs has been modelled in ref.⁷⁹ as a function of the occupancy of surface states, leading to the observed behaviour of both the core and the shell PL. We notice that the regime of hole injection could, in principle, be obtained by applying positive electrochemical potentials or, analogously, expose the NCs to high oxygen pressure. However, since the valence band energy of the CdS shell is ~ 1.5 eV below the intrinsic NC's Fermi level, the strongly oxidative conditions required for hole injection would result in significant damage of the NCs as highlighted by the spectro-electrochemistry trend under positive potential shown in ref ⁷⁹, showing incomplete recovery of the luminescence efficiency already for +1V electrochemical potential, likely caused by photo-assisted oxidation.

3.3 Conclusions

In conclusion, we have demonstrated the first example of a ratiometric O₂-sensing PSP based on a single type of two-colour emitter, that features (i) intrinsic ratiometric response at the single particle level, (ii) negligible overlap between the luminescence spectra of the reference and the sensor, (iii) enhanced sensitivity to O₂ partial pressure, and (iv) temperature-independent ratiometric behaviour. Due to the fact that the shell- and core-PL bands of the DiB NCs exhibit trends of opposite directions in response to exposure to oxygen, our 'double-sensor' *r*-PSPs demonstrate an enhanced pressure sensitivity with respect to that achievable with traditional reference-sensor pairs, where the reference channel is "neutral," *i.e.*, not sensitive to O₂. Specifically, as a result of the direct exposure of shell excitons to the NC surfaces, the shell luminescence is strongly affected by effects of electron withdrawing by O₂, which leads to progressive emission quenching with increasing oxygen pressure. In direct contrast, the core PL is enhanced in the presence of oxygen which helps maintain NCs in the neutral state by removing extra-electrons that otherwise trigger fast nonradiative Auger recombination. As a result of these

opposing trends, the ratiometric response of the NCs is largely amplified with respect to that achievable by monitoring the individual emissions of core and shell. Temperature-controlled PL measurements reveal that temperature-induced changes in pressure sensitivity are negligibly small in the interval between 0°C and 70°C. The sensing response probed both at the ensemble and at the single-particle level using continuous and pulsed excitation is fully reproducible and unaffected by prolonged UV illumination. Finally, a nearly complete spectral separation between the core and the shell emission bands leads to no cross-readout between the two detection channels.

Conclusions

In conclusion, this thesis gathers the study of three nanostructured materials that I carried out during my PhD work, and that shares the common perspective of understanding the NCs behavior under different environments. Specifically, I successfully performed spectroelectrochemistry and optical spectroscopy experiments in order to monitor and model the NCs PL intensity while exposing their surfaces to oxidative and reductive conditions, so as to correlate the occupation of surface defects to their emission efficiency. The experiments allowed me on the one hand to unveil the processes that are beneficial or detrimental to the NCs, which in turn helps identifying potential passivation strategies to adopt in future synthesis, and, on the other hand, to make use of their sensing capability and employ them as optical oxygen sensors or PSPs.

Firstly, in Chapter 1 I explored perovskite NCs as a potential inorganic alternative to traditional organic dye-based PSPs. Spectro-electrochemistry experiments on CsPbBr₃ perovskite NCs show that the main nonradiative channel in these NCs is capture of photo-generated holes in localized states that can be reversibly activated (passivated) upon raising (lowering) the Fermi level through the application of reductive (oxidizing) electrochemical potentials. As a result of the activation of hole traps, the PL is strongly quenched whereas their suppression leads to minor brightening, which strongly suggests that their density in unperturbed conditions is likely small. This feature has important consequences on the response of the NC's emission upon their exposure to oxygen gas that leads to strong quenching of the PL quantum efficiency due to the dominant effect of direct extraction of photo-excited electrons from the NC conduction band over the 'curing' behavior of surface hole traps responsible for the strong PL brightening registered for perovskite films and bulk crystals. This further suggests that, despite the much larger surface to volume ratio of nanocrystals with respect

to bulk or film materials, electron rich surface defects are likely less abundant in the firsts, leading to an emission response dominated by direct interaction with the environment. These results, therefore, suggest that the interaction between perovskite NCs and atmospheric agents could be detrimental to their optical properties and thus demands specific and, possibly, more effective passivation strategies for their optimization and stabilization.

In Chapter 2, I proceeded to investigate a different class of nanostructured NCs, namely, CdSe and CdSe/CdS core-only and core/shell nanoplatelets with the remarkable ability to brighten in presence of oxygen, whose strong electron-accepting behavior typically makes it a PL quencher of both organic and inorganic emitters. In this chapter, I studied the processes of charging and trapping in colloidal nanoplatelets by means of spectroelectrochemical methods and time resolved spectroscopy in a controlled atmosphere. The data demonstrates the brightening effect of oxygen on the emission of NPLs whose efficiency is mainly determined by hole trapping in surface defects. Spectroelectrochemical experiments reproduce well the observed environmental effects and further confirm the improved optical stability of heterostructured, core/shell NPLs. The O₂ sensing process is reversible and could be used to realize novel 'reversed' PSPs capable of generating an enhanced light signal when exposed to harsh environments, with potential impact in aerospace planning, environmental sensing and smart building.

Finally, in Chapter 3 I build on the knowledge acquired in the previous works to demonstrate the first example of a ratiometric O₂-sensing PSP based on a single type of two-colour emitter, consisting of dot-in-bulk (DiB), core/shell CdSe/CdS NCs. Such sensor features intrinsic ratiometric response at the single particle level, negligible overlap between the luminescence spectra of the reference and the sensor, enhanced sensitivity to O₂ partial pressure, and temperature-independent ratiometric behaviour. Due to the fact that the shell- and core-PL bands of the DiB NCs exhibit trends of opposite directions in response to exposure to oxygen, our 'double-sensor' *r*-PSPs demonstrate an enhanced pressure sensitivity with respect

to that achievable with traditional reference-sensor pairs, where the reference channel is “neutral,” *i.e.*, not sensitive to O₂. Specifically, as a result of the direct exposure of shell excitons to the NC surfaces, the shell luminescence is strongly affected by effects of electron withdrawing by O₂, which leads to progressive emission quenching with increasing oxygen pressure. In direct contrast, the core PL is enhanced in the presence of oxygen which helps maintain NCs in the neutral state by removing extra-electrons that otherwise trigger fast nonradiative Auger recombination. As a result of these opposing trends, the ratiometric response of the NCs is largely amplified with respect to that achievable by monitoring the individual emissions of core and shell. Temperature-controlled PL measurements reveal that temperature-induced changes in pressure sensitivity are negligibly small in the interval between 0°C and 70°C. The sensing response probed both at the ensemble and at the single-particle level using continuous and pulsed excitation is fully reproducible and unaffected by prolonged UV illumination. Finally, a nearly complete spectral separation between the core and the shell emission bands leads to no cross-readout between the two detection channels.

References

1. Boles, M. A.; Ling, D.; Hyeon, T.; Talapin, D. V. *Nat Mater* **2016**, 15, (2), 141-153.
2. Klimov, V. I., *Nanocrystal quantum dots*. CRC Press: 2010.
3. Lüth, H., *Solid surfaces, interfaces and thin films*. Springer: 2001; Vol. 4.
4. Park, R. L.; Lagally, M. G., *Solid state physics: surfaces*. Academic Press: 1985; Vol. 22.
5. Hines, D. A.; Kamat, P. V. *ACS Appl. Mater. Interfaces* **2014**, 6, (5), 3041-3057.
6. Yoffe, A. D. *Advances in Physics* **2001**, 50, (1), 1-208.
7. Jones, M.; Lo, S. S.; Scholes, G. D. *Proceedings of the National Academy of Sciences* **2009**, 106, (9), 3011-3016.
8. Yu, M.; Fernando, G. W.; Li, R.; Papadimitrakopoulos, F.; Shi, N.; Ramprasad, R. *Appl. Phys. Lett.* **2006**, 88, (23), 231910.
9. Becerra, L. R.; Murray, C. B.; Griffin, R. G.; Bawendi, M. G. *The Journal of Chemical Physics* **1994**, 100, (4), 3297-3300.
10. Katari, J. B.; Colvin, V. L.; Alivisatos, A. P. *J. Phys. Chem.* **1994**, 98, (15), 4109-4117.
11. Gómez-Campos, F. M.; Califano, M. *Nano Lett.* **2012**, 12, (9), 4508-4517.
12. Hines, M. A.; Guyot-Sionnest, P. *J. Phys. Chem.* **1996**, 100, (2), 468-471.
13. Kambhampati, P. *J. Phys. Chem. C* **2011**, 115, (45), 22089-22109.
14. Kramer, I. J.; Sargent, E. H. *ACS Nano* **2011**, 5, (11), 8506-8514.
15. Frantsuzov, P. A.; Marcus, R. A. *Phys. Rev. B* **2005**, 72, (15), 155321.
16. Abdellah, M.; Karki, K. J.; Lenngren, N.; Zheng, K.; Pascher, T.; Yartsev, A.; Pullerits, T. *J. Phys. Chem. C* **2014**, 118, (37), 21682-21686.
17. Califano, M.; Franceschetti, A.; Zunger, A. *Nano Lett.* **2005**, 5, (12), 2360-2364.
18. Chestnoy, N.; Harris, T. D.; Hull, R.; Brus, L. E. *J. Phys. Chem.* **1986**, 90, (15), 3393-3399.

19. Mooney, J.; Krause, M. M.; Saari, J. I.; Kambhampati, P. *Phys. Rev. B* **2013**, 87, (8), 081201.
20. Rosson, T. E.; Claiborne, S. M.; McBride, J. R.; Stratton, B. S.; Rosenthal, S. J. *J. Am. Chem. Soc.* **2012**, 134, (19), 8006-8009.
21. Bowers, M. J.; McBride, J. R.; Rosenthal, S. J. *J. Am. Chem. Soc.* **2005**, 127, (44), 15378-15379.
22. Michalet, X.; Pinaud, F.; Bentolila, L.; Tsay, J.; Doose, S.; Li, J.; Sundaresan, G.; Wu, A.; Gambhir, S.; Weiss, S. *Science* **2005**, 307, (5709), 538-544.
23. Jethi, L.; Krause, M. M.; Kambhampati, P. *J. Phys. Chem. Lett.* **2015**, 6, (4), 718-721.
24. Lorenzon, M.; Christodoulou, S.; Vaccaro, G.; Pedrini, J.; Meinardi, F.; Moreels, I.; Brovelli, S. *Nat Commun* **2015**, 6.
25. Lorenzon, M.; Pinchetti, V.; Bruni, F.; Bae, W. K.; Meinardi, F.; Klimov, V. I.; Brovelli, S. *Nano Lett.* **2016**.
26. Bell, J. H.; Schairer, E. T.; Hand, L. A.; Mehta, R. D. *Annu. Rev. Fluid Mech.* **2001**, 33, (1), 155-206.
27. Gregory, J. W.; Sakaue, H.; Liu, T.; Sullivan, J. P. *Annu. Rev. Fluid Mech.* **2014**, 46, (1), 303-330.
28. Liu, T.; Sullivan, J., Pressure and temperature sensitive paints. Springer, Berlin: 2005.
29. Engler, R. H.; Chr, K.; Trinks, O. *Meas. Sci. Technol.* **2000**, 11, (7), 1077.
30. Gregory, J. W.; Asai, K.; Kameda, M.; Liu, T.; Sullivan, J. P. *Proc. Inst. Mech. Eng. G J. Aerosp. Eng.* **2008**, 222, (2), 249-290.
31. Le Sant, Y.; Mérienne, M. C. *Aerosp. Sci. Technol.* **2005**, 9, (4), 285-299.
32. McLachlan, B. G.; Bell, J. H. *Exp. Therm. Fluid Sci.* **1995**, 10, (4), 470-485.
33. Ishii, M.; Isokawa, H.; Miyazaki, T.; Sakaue, H., Surface State Measurement of a Free-Flight Object by Motion-Capturing Method. In *55th AIAA Aerospace Sciences Meeting*, American Institute of Aeronautics and Astronautics: 2017.
34. Xiang, H.; Zhou, L.; Feng, Y.; Cheng, J.; Wu, D.; Zhou, X. *Inorg. Chem.* **2012**, 51, (9), 5208-5212.
35. Bogard, D. G.; Thole, K. A. *Journal of Propulsion and Power* **2006**, 22, (2), 249-270.

36. Collier, B. B.; Singh, S.; McShane, M. *Analyst* **2011**, 136, (5), 962-967.
37. Carraway, E. R.; Demas, J. N.; DeGraff, B. A.; Bacon, J. R. *Anal. Chem.* **1991**, 63, (4), 337-342.
38. Shi, H.; Ma, X.; Zhao, Q.; Liu, B.; Qu, Q.; An, Z.; Zhao, Y.; Huang, W. *Adv. Funct. Mater.* **2014**, 24, (30), 4823-4830.
39. Yoshihara, T.; Yamaguchi, Y.; Hosaka, M.; Takeuchi, T.; Tobita, S. *Angew. Chem. Int. Ed.* **2012**, 51, (17), 4148-4151.
40. Chihyung, H.; Gregory, J. W.; Sullivan, J. P. *J. Microelectromech. Syst.* **2007**, 16, (4), 777-785.
41. Quaranta, M.; Murkovic, M.; Klimant, I. *Analyst* **2013**, 138, (21), 6243-6245.
42. Pandey, A.; Sarma, D. D. *Zeitschrift für anorganische und allgemeine Chemie* **2016**, 642, (23), 1331-1339.
43. Disotell, K.; Peng, D.; Juliano, T.; Gregory, J.; Crafton, J.; Komerath, N. *Exp Fluids* **2014**, 55, (2), 1-15.
44. Sakaue, H.; Morita, K.; Iijima, Y.; Sakamura, Y. *Sensor Actuat. A-Phys* **2013**, 199, (0), 74-79.
45. Amao, Y.; Ishikawa, Y.; Okura, I. *Anal. Chim. Acta* **2001**, 445, (2), 177-182.
46. Amao, Y.; Miyashita, T.; Okura, I. *React. Funct. Polym.* **2001**, 47, (1), 49-54.
47. Matsuda, Y.; Uchida, T.; Suzuki, S.; Misaki, R.; Yamaguchi, H.; Niimi, T. *Microfluid. Nanofluidics* **2011**, 10, (1), 165-171.
48. Puklin, E.; Carlson, B.; Gouin, S.; Costin, C.; Green, E.; Ponomarev, S.; Tanji, H.; Gouterman, M. *Journal of Applied Polymer Science* **2000**, 77, (13), 2795-2804.
49. Basu, B. J.; Anandan, C.; Rajam, K. S. *Sensor Actuat. B-Chem.* **2003**, 94, (3), 257-266.
50. Basu, B. J.; Thirumurugan, A.; Dinesh, A. R.; Anandan, C.; Rajam, K. S. *Sensor Actuat. B-Chem.* **2005**, 104, (1), 15-22.
51. Fernández-Sánchez, J. F.; Roth, T.; Cannas, R.; Nazeeruddin, M. K.; Spichiger, S.; Graetzel, M.; Spichiger-Keller, U. E. *Talanta* **2007**, 71, (1), 242-250.
52. Kameda, M.; Seki, H.; Makoshi, T.; Amao, Y.; Nakakita, K. *Sensor Actuat. B-Chem.* **2012**, 171-172, 343-349.

53. Lakowicz, J. R.; Weber, G. *Biochemistry* **1973**, 12, (21), 4161-4170.
54. Bae, W. K.; Kwak, J.; Lim, J.; Lee, D.; Nam, M. K.; Char, K.; Lee, C.; Lee, S. *Nano Lett.* **2010**, 10, (7), 2368-2373.
55. Shirasaki, Y.; Supran, G. J.; Bawendi, M. G.; Bulovic, V. *Nat Photon* **2013**, 7, (1), 13-23.
56. Jaiswal, J. K.; Mattoussi, H.; Mauro, J. M.; Simon, S. M. *Nat Biotech* **2003**, 21, (1), 47-51.
57. García-Santamaría, F.; Chen, Y.; Vela, J.; Schaller, R. D.; Hollingsworth, J. A.; Klimov, V. I. *Nano Lett.* **2009**, 9, (10), 3482-3488.
58. Klimov, V. I.; Mikhailovsky, A. A.; Xu, S.; Malko, A.; Hollingsworth, J. A.; Leatherdale, C. A.; Eisler, H.-J.; Bawendi, M. G. *Science* **2000**, 290, (5490), 314-317.
59. Pal, B. N.; Ghosh, Y.; Brovelli, S.; Laocharoensuk, R.; Klimov, V. I.; Hollingsworth, J. A.; Htoon, H. *Nano Lett.* **2011**, 12, (1), 331-336.
60. Ho, Y.-P.; Leong, K. W. *Nanoscale* **2010**, 2, (1), 60-68.
61. Alivisatos, A. P.; Gu, W.; Larabell, C. *Annu. Rev. Biomed. Eng.* **2005**, 7, (1), 55-76.
62. Alivisatos, P. *Nat Biotech* **2004**, 22, (1), 47-52.
63. Deng, D.; Chen, Y.; Cao, J.; Tian, J.; Qian, Z.; Achilefu, S.; Gu, Y. *Chemistry of Materials* **2012**, 24, (15), 3029-3037.
64. Dubertret, B.; Skourides, P.; Norris, D. J.; Noireaux, V.; Brivanlou, A. H.; Libchaber, A. *Science* **2002**, 298, (5599), 1759-1762.
65. Gao, Z.; Narzary, D. P.; Han, J.-C. *International Journal of Heat and Mass Transfer* **2008**, 51, (9-10), 2139-2152.
66. Ahn, J.; Mhetras, S.; Han, J.-C. *Journal of Heat Transfer* **2005**, 127, (5), 521-530.
67. McLaurin, E. J.; Greytak, A. B.; Bawendi, M. G.; Nocera, D. G. *J. Am. Chem. Soc.* **2009**, 131, (36), 12994-13001.
68. Müller, J.; Lupton, J. M.; Rogach, A. L.; Feldmann, J.; Talapin, D. V.; Weller, H. *Appl. Phys. Lett.* **2004**, 85, (3), 381-383.
69. Pechstedt, K.; Whittle, T.; Baumberg, J.; Melvin, T. *J. Phys. Chem. C* **2010**, 114, (28), 12069-12077.
70. Protesescu, L.; Yakunin, S.; Bodnarchuk, M. I.; Krieg, F.; Caputo, R.; Hendon, C. H.; Yang, R. X.; Walsh, A.; Kovalenko, M. V. *Nano Lett.* **2015**.

71. Yakunin, S.; Protesescu, L.; Krieg, F.; Bodnarchuk, M. I.; Nedelcu, G.; Humer, M.; De Luca, G.; Fiebig, M.; Heiss, W.; Kovalenko, M. V. *Nat Commun* **2015**, *6*.
72. Kovalenko, M. V.; Protesescu, L.; Bodnarchuk, M. I. *Science* **2017**, *358*, (6364), 745-750.
73. Ithurria, S.; Tessier, M. D.; Mahler, B.; Lobo, R. P. S. M.; Dubertret, B.; Efros, A. L. *Nat Mater* **2011**, *10*, (12), 936-941.
74. Naeem, A.; Masia, F.; Christodoulou, S.; Moreels, I.; Borri, P.; Langbein, W. *Phys. Rev. B* **2015**, *91*, (12), 121302.
75. She, C.; Fedin, I.; Dolzhenkov, D. S.; Demortière, A.; Schaller, R. D.; Pelton, M.; Talapin, D. V. *Nano Lett.* **2014**, *14*, (5), 2772-2777.
76. Kunneman, L. T.; Tessier, M. D.; Heuclin, H.; Dubertret, B.; Aulin, Y. V.; Grozema, F. C.; Schins, J. M.; Siebbeles, L. D. A. *J. Phys. Chem. Lett.* **2013**, *4*, (21), 3574-3578.
77. Brovelli, S.; Bae, W. K.; Galland, C.; Giovanella, U.; Meinardi, F.; Klimov, V. I. *Nano Lett.* **2013**, *14*, (2), 486-494.
78. Galland, C.; Brovelli, S.; Bae, W. K.; Padilha, L. A.; Meinardi, F.; Klimov, V. I. *Nano Lett.* **2012**, *13*, (1), 321-328.
79. Brovelli, S.; Bae, W. K.; Meinardi, F.; Santiago González, B.; Lorenzon, M.; Galland, C.; Klimov, V. I. *Nano Lett.* **2014**, *14*, (7), 3855-3863.
80. Sutherland, B. R.; Sargent, E. H. *Nat Photon* **2016**, *10*, (5), 295-302.
81. Green, M. A.; Ho-Baillie, A.; Snaith, H. J. *Nat Photon* **2014**, *8*, (7), 506-514.
82. Bae, W. K.; Padilha, L. A.; Park, Y.-S.; McDaniel, H.; Robel, I.; Pietryga, J. M.; Klimov, V. I. *ACS Nano* **2013**, *7*, (4), 3411-3419.
83. Service, R. F. *Science* **2014**, *344*, (6183), 458-458.
84. Snaith, H. J. *J. Phys. Chem. Lett.* **2013**, *4*, (21), 3623-3630.
85. Tsai, H.; Nie, W.; Blancon, J.-C.; Stoumpos, C. C.; Asadpour, R.; Harutyunyan, B.; Neukirch, A. J.; Verduzco, R.; Crochet, J. J.; Tretiak, S.; Pedesseau, L.; Even, J.; Alam, M. A.; Gupta, G.; Lou, J.; Ajayan, P. M.; Bedzyk, M. J.; Kanatzidis, M. G.; Mohite, A. D. *Nature* **2016**, *536*, (7616), 312-316.
86. Nie, W.; Tsai, H.; Asadpour, R.; Blancon, J.-C.; Neukirch, A. J.; Gupta, G.; Crochet, J. J.; Chhowalla, M.; Tretiak, S.; Alam, M. A.; Wang, H.-L.; Mohite, A. D. *Science* **2015**, *347*, (6221), 522-525.

87. Tan, Z.-K.; Moghaddam, R. S.; Lai, M. L.; Docampo, P.; Higler, R.; Deschler, F.; Price, M.; Sadhanala, A.; Pazos, L. M.; Credgington, D.; Hanusch, F.; Bein, T.; Snaith, H. J.; Friend, R. H. *Nat Nano* **2014**, 9, (9), 687-692.
88. Zhang, F.; Zhong, H.; Chen, C.; Wu, X.-g.; Hu, X.; Huang, H.; Han, J.; Zou, B.; Dong, Y. *ACS Nano* **2015**, 9, (4), 4533-4542.
89. Xing, G.; Mathews, N.; Lim, S. S.; Yantara, N.; Liu, X.; Sabba, D.; Grätzel, M.; Mhaisalkar, S.; Sum, T. C. *Nat Mater* **2014**, 13, (5), 476-480.
90. Zhu, H.; Fu, Y.; Meng, F.; Wu, X.; Gong, Z.; Ding, Q.; Gustafsson, M. V.; Trinh, M. T.; Jin, S.; Zhu, X. Y. *Nat Mater* **2015**, 14, (6), 636-642.
91. Chen, S.; Shi, G. *Adv. Mater.* **2017**, 1605448-n/a.
92. Yakunin, S.; Sytnyk, M.; Kriegner, D.; Shrestha, S.; Richter, M.; Matt, G. J.; Azimi, H.; Brabec, C. J.; Stangl, J.; Kovalenko, M. V.; Heiss, W. *Nat Photon* **2015**, 9, (7), 444-449.
93. Sichert, J. A.; Tong, Y.; Mutz, N.; Vollmer, M.; Fischer, S.; Milowska, K. Z.; García Cortadella, R.; Nickel, B.; Cardenas-Daw, C.; Stolarczyk, J. K.; Urban, A. S.; Feldmann, J. *Nano Lett.* **2015**, 15, (10), 6521-6527.
94. Zhang, D.; Eaton, S. W.; Yu, Y.; Dou, L.; Yang, P. *J. Am. Chem. Soc.* **2015**, 137, (29), 9230-9233.
95. Akkerman, Q. A.; D’Innocenzo, V.; Accornero, S.; Scarpellini, A.; Petrozza, A.; Prato, M.; Manna, L. *J. Am. Chem. Soc.* **2015**, 137, (32), 10276-10281.
96. Akkerman, Q. A.; Motti, S. G.; Srimath Kandada, A. R.; Mosconi, E.; D’Innocenzo, V.; Bertoni, G.; Marras, S.; Kamino, B. A.; Miranda, L.; De Angelis, F.; Petrozza, A.; Prato, M.; Manna, L. *J. Am. Chem. Soc.* **2016**, 138, (3), 1010-1016.
97. Nedelcu, G.; Protesescu, L.; Yakunin, S.; Bodnarchuk, M. I.; Grotevent, M. J.; Kovalenko, M. V. *Nano Lett.* **2015**, 15, (8), 5635-5640.
98. Bekenstein, Y.; Koscher, B. A.; Eaton, S. W.; Yang, P.; Alivisatos, A. P. *J. Am. Chem. Soc.* **2015**, 137, (51), 16008-16011.
99. Shamsi, J.; Dang, Z.; Bianchini, P.; Canale, C.; Stasio, F. D.; Brescia, R.; Prato, M.; Manna, L. *J. Am. Chem. Soc.* **2016**, 138, (23), 7240-7243.
100. Kim, Y.; Yassitepe, E.; Voznyy, O.; Comin, R.; Walters, G.; Gong, X.; Kanjanaboos, P.; Nogueira, A. F.; Sargent, E. H. *ACS Appl. Mater. Interfaces* **2015**, 7, (45), 25007-25013.

101. Palazon, F.; Akkerman, Q. A.; Prato, M.; Manna, L. *ACS Nano* **2016**, *10*, (1), 1224-1230.
102. De Roo, J.; Ibáñez, M.; Geiregat, P.; Nedelcu, G.; Walravens, W.; Maes, J.; Martins, J. C.; Van Driessche, I.; Kovalenko, M. V.; Hens, Z. *ACS Nano* **2016**, *10*, (2), 2071-2081.
103. Huang, H.; Chen, B.; Wang, Z.; Hung, T. F.; Susha, A. S.; Zhong, H.; Rogach, A. L. *Chem. Sci.* **2016**, *7*, (9), 5699-5703.
104. Zhang, X.; Lv, L.; Ji, L.; Guo, G.; Liu, L.; Han, D.; Wang, B.; Tu, Y.; Hu, J.; Yang, D.; Dong, A. *J. Am. Chem. Soc.* **2016**, *138*, (10), 3290-3293.
105. Makarov, N. S.; Guo, S.; Isaienko, O.; Liu, W.; Robel, I.; Klimov, V. I. *Nano Lett.* **2016**, *16*, (4), 2349-2362.
106. Park, Y.-S.; Guo, S.; Makarov, N. S.; Klimov, V. I. *ACS Nano* **2015**, *9*, (10), 10386-10393.
107. Rainò, G.; Nedelcu, G.; Protesescu, L.; Bodnarchuk, M. I.; Kovalenko, M. V.; Mahrt, R. F.; Stöferle, T. *ACS Nano* **2016**, *10*, (2), 2485-2490.
108. Swarnkar, A.; Chulliyil, R.; Ravi, V. K.; Irfanullah, M.; Chowdhury, A.; Nag, A. *Angew. Chem. Int. Ed.* **2015**, *54*, (51), 15424-15428.
109. Tian, Y.; Merdasa, A.; Peter, M.; Abdellah, M.; Zheng, K.; Ponseca, C. S.; Pullerits, T.; Yartsev, A.; Sundström, V.; Scheblykin, I. G. *Nano Lett.* **2015**, *15*, (3), 1603-1608.
110. Fu, M.; Tamarat, P.; Huang, H.; Even, J.; Rogach, A. L.; Lounis, B. *Nano Lett.* **2017**.
111. Castañeda, J. A.; Nagamine, G.; Yassitepe, E.; Bonato, L. G.; Voznyy, O.; Hoogland, S.; Nogueira, A. F.; Sargent, E. H.; Cruz, C. H. B.; Padilha, L. A. *ACS Nano* **2016**, *10*, (9), 8603-8609.
112. Eaton, S. W.; Lai, M.; Gibson, N. A.; Wong, A. B.; Dou, L.; Ma, J.; Wang, L.-W.; Leone, S. R.; Yang, P. *Proceedings of the National Academy of Sciences* **2016**, *113*, (8), 1993-1998.
113. Wang, Y.; Li, X.; Song, J.; Xiao, L.; Zeng, H.; Sun, H. *Adv. Mater.* **2015**, *27*, (44), 7101-7108.
114. Sun, S.; Yuan, D.; Xu, Y.; Wang, A.; Deng, Z. *ACS Nano* **2016**, *10*, (3), 3648-3657.

115. Xu, Y.; Chen, Q.; Zhang, C.; Wang, R.; Wu, H.; Zhang, X.; Xing, G.; Yu, W. W.; Wang, X.; Zhang, Y.; Xiao, M. *J. Am. Chem. Soc.* **2016**, *138*, (11), 3761-3768.
116. Yakunin, S.; Protesescu, L.; Krieg, F.; Bodnarchuk, M. I.; Nedelcu, G.; Humer, M.; De Luca, G.; Fiebig, M.; Heiss, W.; Kovalenko, M. V. *Nat. Commun.* **2015**, *6*, 8056.
117. Yassitepe, E.; Yang, Z.; Voznyy, O.; Kim, Y.; Walters, G.; Castañeda, J. A.; Kanjanaboos, P.; Yuan, M.; Gong, X.; Fan, F.; Pan, J.; Hoogland, S.; Comin, R.; Bakr, O. M.; Padilha, L. A.; Nogueira, A. F.; Sargent, E. H. *Adv. Funct. Mater.* **2016**, *26*, (47), 8757-8763.
118. Li, G.; Rivarola, F. W. R.; Davis, N. J. L. K.; Bai, S.; Jellicoe, T. C.; de la Peña, F.; Hou, S.; Ducati, C.; Gao, F.; Friend, R. H.; Greenham, N. C.; Tan, Z.-K. *Adv. Mater.* **2016**, *28*, (18), 3528-3534.
119. Palazon, F.; Di Stasio, F.; Akkerman, Q. A.; Krahne, R.; Prato, M.; Manna, L. *Chemistry of Materials* **2016**, *28*, (9), 2902-2906.
120. Song, J.; Li, J.; Li, X.; Xu, L.; Dong, Y.; Zeng, H. *Adv. Mater.* **2015**, *27*, (44), 7162-7167.
121. Zhang, X.; Lin, H.; Huang, H.; Reckmeier, C.; Zhang, Y.; Choy, W. C. H.; Rogach, A. L. *Nano Lett.* **2016**, *16*, (2), 1415-1420.
122. Zhang, X.; Xu, B.; Zhang, J.; Gao, Y.; Zheng, Y.; Wang, K.; Sun, X. W. *Adv. Funct. Mater.* **2016**, *26*, (25), 4595-4600.
123. Swarnkar, A.; Marshall, A. R.; Sanehira, E. M.; Chernomordik, B. D.; Moore, D. T.; Christians, J. A.; Chakrabarti, T.; Luther, J. M. *Science* **2016**, *354*, (6308), 92-95.
124. Akkerman, Q. A.; Gandini, M.; Di Stasio, F.; Rastogi, P.; Palazon, F.; Bertoni, G.; Ball, J. M.; Prato, M.; Petrozza, A.; Manna, L. *Nature Energy* **2016**, *2*, 16194.
125. Liu, W.; Lin, Q.; Li, H.; Wu, K.; Robel, I.; Pietryga, J. M.; Klimov, V. I. *J. Am. Chem. Soc.* **2016**.
126. Parobek, D.; Roman, B. J.; Dong, Y.; Jin, H.; Lee, E.; Sheldon, M.; Son, D. H. *Nano Lett.* **2016**.
127. Mir, W. J.; Jagadeeswararao, M.; Das, S.; Nag, A. *ACS Energy Lett* **2017**, *2*, 537-543.
128. van der Stam, W.; Geuchies, J. J.; Altantzis, T.; van den Bos, K. H. W.; Meeldijk, J. D.; Van Aert, S.; Bals, S.; Vanmaekelbergh, D.; de Mello Donegá, C. *J. Am. Chem. Soc.* **2017**.

129. Begum, R.; Parida, M. R.; Abdelhady, A. L.; Murali, B.; Alyami, N. M.; Ahmed, G. H.; Hedhili, M. N.; Bakr, O. M.; Mohammed, O. F. *J. Am. Chem. Soc.* **2017**, 139, (2), 731-737.
130. Swarnkar, A.; Ravi, V. K.; Nag, A. *ACS Energy Lett.* **2017**.
131. Frost, J. M.; Butler, K. T.; Brivio, F.; Hendon, C. H.; van Schilfgaarde, M.; Walsh, A. *Nano Lett.* **2014**, 14, (5), 2584-2590.
132. Walsh, A.; Scanlon, D. O.; Chen, S.; Gong, X. G.; Wei, S.-H. *Angewandte Chemie* **2015**, 127, (6), 1811-1814.
133. Bakulin, A. A.; Selig, O.; Bakker, H. J.; Rezus, Y. L. A.; Müller, C.; Glaser, T.; Lovrincic, R.; Sun, Z.; Chen, Z.; Walsh, A.; Frost, J. M.; Jansen, T. L. C. *J. Phys. Chem. Lett.* **2015**, 6, (18), 3663-3669.
134. Brivio, F.; Walker, A. B.; Walsh, A. *APL Materials* **2013**, 1, (4), 042111.
135. Leguy, A. M. A.; Frost, J. M.; McMahon, A. P.; Sakai, V. G.; Kockelmann, W.; Law, C.; Li, X.; Foglia, F.; Walsh, A.; O'Regan, B. C.; Nelson, J.; Cabral, J. T.; Barnes, P. R. F. *Nat. Commun.* **2015**, 6, 7124.
136. Quarti, C.; Mosconi, E.; De Angelis, F. *Phys. Chem. Chem. Phys.* **2015**, 17, (14), 9394-9409.
137. Quarti, C.; Mosconi, E.; De Angelis, F. *Chemistry of Materials* **2014**, 26, (22), 6557-6569.
138. Brivio, F.; Frost, J. M.; Skelton, J. M.; Jackson, A. J.; Weber, O. J.; Weller, M. T.; Goñi, A. R.; Leguy, A. M. A.; Barnes, P. R. F.; Walsh, A. *Phys. Rev. B* **2015**, 92, (14), 144308.
139. Mosconi, E.; De Angelis, F. *ACS Energy Lett.* **2016**, 1, (1), 182-188.
140. Blancon, J.-C.; Nie, W.; Neukirch, A. J.; Gupta, G.; Tretiak, S.; Cagnet, L.; Mohite, A. D.; Crochet, J. J. *Adv. Funct. Mater.* **2016**, 26, (24), 4283-4292.
141. Wehrenfennig, C.; Eperon, G. E.; Johnston, M. B.; Snaith, H. J.; Herz, L. M. *Adv. Mater.* **2014**, 26, (10), 1584-1589.
142. Yettapu, G. R.; Talukdar, D.; Sarkar, S.; Swarnkar, A.; Nag, A.; Ghosh, P.; Mandal, P. *Nano Lett.* **2016**.
143. Brandt, R. E.; Stevanović, V.; Ginley, D. S.; Buonassisi, T. *MRS Communications* **2015**, 5, (2), 265-275.
144. Dirin, D. N.; Protesescu, L.; Trummer, D.; Kochetygov, I. V.; Yakunin, S.; Krumeich, F.; Stadie, N. P.; Kovalenko, M. V. *Nano Lett.* **2016**, 16, (9), 5866-5874.

145. Kang, J.; Wang, L.-W. *J. Phys. Chem. Lett.* **2017**, 8, (2), 489-493.
146. Zakutayev, A.; Caskey, C. M.; Fioretti, A. N.; Ginley, D. S.; Vidal, J.; Stevanovic, V.; Tea, E.; Lany, S. *J. Phys. Chem. Lett.* **2014**, 5, (7), 1117-1125.
147. Qin, H.; Meng, R.; Wang, N.; Peng, X. *Adv. Mater.* **2017**, n/a-n/a.
148. Choi, J.-H.; Oh, S. J.; Lai, Y.; Kim, D. K.; Zhao, T.; Fafarman, A. T.; Diroll, B. T.; Murray, C. B.; Kagan, C. R. *ACS Nano* **2013**, 7, (9), 8275-8283.
149. Feng, Y.; Cheng, J.; Zhou, L.; Zhou, X.; Xiang, H. *Analyst* **2012**, 137, (21), 4885-4901.
150. Lorenzon, M.; Christodoulou, S.; Vaccaro, G.; Pedrini, J.; Meinardi, F.; Moreels, I.; Brovelli, S. *Nature Commun.* **2015**, 6.
151. Saba, M.; Aresti, M.; Quochi, F.; Marceddu, M.; Loi, M. A.; Huang, J.; Talapin, D. V.; Mura, A.; Bongiovanni, G. *ACS Nano* **2013**, 7, (1), 229-238.
152. Abate, A.; Saliba, M.; Hollman, D. J.; Stranks, S. D.; Wojciechowski, K.; Avolio, R.; Grancini, G.; Petrozza, A.; Snaith, H. J. *Nano Lett.* **2014**, 14, (6), 3247-3254.
153. Han, P.; Mihi, A.; Ferre-borrull, J.; Pallarés, J.; Marsal, L. F. *J. Phys. Chem. C* **2015**, 119, (19), 10693-10699.
154. Hens, Z.; Moreels, I.; Martins, J. C. *ChemPhysChem* **2005**, 6, (12), 2578-2584.
155. Xu, S.; Ziegler, J.; Nann, T. *Journal of Materials Chemistry* **2008**, 18, (23), 2653-2656.
156. Motti, S. G.; Gandini, M.; Barker, A. J.; Ball, J. M.; Srimath Kandada, A. R.; Petrozza, A. *ACS Energy Lett.* **2016**, 1, (4), 726-730.
157. Galisteo-López, J. F.; Anaya, M.; Calvo, M. E.; Míguez, H. *J. Phys. Chem. Lett.* **2015**, 6, (12), 2200-2205.
158. Fang, H.-H.; Adjokatse, S.; Wei, H.; Yang, J.; Blake, G. R.; Huang, J.; Even, J.; Loi, M. A. *Science Advances* **2016**, 2, (7).
159. Tian, Y.; Merdasa, A.; Unger, E.; Abdellah, M.; Zheng, K.; McKibbin, S.; Mikkelsen, A.; Pullerits, T.; Yartsev, A.; Sundström, V.; Scheblykin, I. G. *J. Phys. Chem. Lett.* **2015**, 6, (20), 4171-4177.
160. Javaux C; Mahler B; Dubertret B; Shabaev A; Rodina, A. V.; EfrosAl, L.; Yakovlev, D. R.; Liu F; Bayer M; Camps G; Biadala L; Buil S; Quelin X; Hermier, J. P. *Nat Nano* **2013**, 8, (3), 206-212.

161. Liu, F.; Biadala, L.; Rodina, A. V.; Yakovlev, D. R.; Dunker, D.; Javaux, C.; Hermier, J.-P.; Efros, A. L.; Dubertret, B.; Bayer, M. *Phys. Rev. B* **2013**, 88, (3), 035302.
162. Leijtens, T.; Eperon, G. E.; Barker, A. J.; Grancini, G.; Zhang, W.; Ball, J. M.; Kandada, A. R. S.; Snaith, H. J.; Petrozza, A. *Energy & Environmental Science* **2016**, 9, (11), 3472-3481.
163. Cottingham, P.; Brutchey, R. L. *Chemical Communications* **2016**, 52, (30), 5246-5249.
164. Slater, J. C. *The Journal of Chemical Physics* **1964**, 41, (10), 3199-3204.
165. Ahrens, L. H. *Geochimica et Cosmochimica Acta* **1952**, 2, (3), 155-169.
166. Crooker, S. A.; Barrick, T.; Hollingsworth, J. A.; Klimov, V. I. *Appl. Phys. Lett.* **2003**, 82, (17), 2793-2795.
167. Niimi, T.; Yoshida, M.; Kondo, M.; Oshima, Y.; Mori, H.; Egami, Y.; Asai, K.; Nishide, H. *J. Thermophys. Heat Tr.* **2005**, 19, (1), 9-16.
168. Ravi, V. K.; Markad, G. B.; Nag, A. *ACS Energy Lett.* **2016**, 1, (4), 665-671.
169. Brovelli, S.; Galland, C.; Viswanatha, R.; Klimov, V. I. *Nano Lett.* **2012**, 12, (8), 4372-4379.
170. Galland, C.; Ghosh, Y.; Steinbrueck, A.; Sykora, M.; Hollingsworth, J. A.; Klimov, V. I.; Htoon, H. *Nature* **2011**, 479, (Copyright (C) 2014 American Chemical Society (ACS). All Rights Reserved.), 203-207.
171. Jha, P. P.; Guyot-Sionnest, P. *J. Phys. Chem. C* **2010**, 114, (49), 21138-21141.
172. Dewald, J. F. *J. Phys. Chem. Solids* **1960**, 14, (0), 155-161.
173. Jin, S.; Song, N.; Lian, T. *ACS Nano* **2010**, 4, (3), 1545-1552.
174. Padilha, L. A.; Robel, I.; Lee, D. C.; Nagpal, P.; Pietryga, J. M.; Klimov, V. I. *ACS Nano* **2011**, 5, (6), 5045-5055.
175. Nazzal, A. Y.; Qu, L.; Peng, X.; Xiao, M. *Nano Lett.* **2003**, 3, (6), 819-822.
176. Lakowicz, J., *Principles of Fluorescence Spectroscopy*. 3rd ed.; Springer: 2006.
177. Stranks, S. D.; Eperon, G. E.; Grancini, G.; Menelaou, C.; Alcocer, M. J. P.; Leijtens, T.; Herz, L. M.; Petrozza, A.; Snaith, H. J. *Science* **2013**, 342, (6156), 341-344.

178. Li, Y.; Yan, W.; Li, Y.; Wang, S.; Wang, W.; Bian, Z.; Xiao, L.; Gong, Q. *Scientific Reports* **2015**, *5*, 14485.
179. Xing, G.; Mathews, N.; Sun, S.; Lim, S. S.; Lam, Y. M.; Grätzel, M.; Mhaisalkar, S.; Sum, T. C. *Science* **2013**, *342*, (6156), 344-347.
180. Wan Ki Bae, S. B. a. V. I. K. *MRS Bulletin* **2013**, *38*, 721-730.
181. Sargent, E. H. *Nat Photon* **2012**, *6*, (3), 133-135.
182. Grim, J. Q.; Christodoulou, S.; Di Stasio, F.; Krahne, R.; Cingolani, R.; Manna, L.; Moreels, I. *Nat Nano* **2014**, advance online publication.
183. Kress, S. J. P.; Richner, P.; Jayanti, S. V.; Galliker, P.; Kim, D. K.; Poulidakos, D.; Norris, D. J. *Nano Lett.* **2014**, *14*, (10), 5827-5833.
184. Brokmann, X.; Messin, G.; Desbiolles, P.; Giacobino, E.; Dahan, M.; Hermier, J. P. *New Journal of Physics* **2004**, *6*, (1), 99.
185. PandeyA; BrovelliS; ViswanathaR; LiL; Pietryga, J. M.; Klimov, V. I.; Crooker, S. A. *Nat Nano* **2012**, *7*, (12), 792-797.
186. Meinardi, F.; Colombo, A.; Velizhanin, K. A.; Simonutti, R.; Lorenzon, M.; Beverina, L.; Viswanatha, R.; Klimov, V. I.; Brovelli, S. *Nat Photon* **2014**, *8*, (5), 392-399.
187. Talapin, D. V.; Lee, J.-S.; Kovalenko, M. V.; Shevchenko, E. V. *Chemical reviews* **2009**, *110*, (1), 389-458.
188. Reiss, P.; Protière, M.; Li, L. *Small* **2009**, *5*, (2), 154-168.
189. Rainò, G.; Stöferle, T.; Moreels, I.; Gomes, R.; Kamal, J. S.; Hens, Z.; Mahrt, R. F. *ACS Nano* **2011**, *5*, (5), 4031-4036.
190. Allione, M.; Ballester, A.; Li, H.; Comin, A.; Movilla, J. L.; Climente, J. I.; Manna, L.; Moreels, I. *ACS Nano* **2013**, *7*, (3), 2443-2452.
191. Borys, N. J.; Walter, M. J.; Huang, J.; Talapin, D. V.; Lupton, J. M. *Science* **2010**, *330*, (6009), 1371-1374.
192. Cassette, E.; Mahler, B.; Guigner, J.-M.; Patriarche, G.; Dubertret, B.; Pons, T. *ACS Nano* **2012**, *6*, (8), 6741-6750.
193. Joo, J.; Son, J. S.; Kwon, S. G.; Yu, J. H.; Hyeon, T. *J. Am. Chem. Soc.* **2006**, *128*, (17), 5632-5633.
194. Sitt, A.; Salant, A.; Menagen, G.; Banin, U. *Nano Lett.* **2011**, *11*, (5), 2054-2060.
195. Achtstein, A. W.; Schliwa, A.; Prudnikau, A.; Hardzei, M.; Artemyev, M. V.; Thomsen, C.; Woggon, U. *Nano Lett.* **2012**, *12*, (6), 3151-3157.
196. Tessier, M. D.; Mahler, B.; Nadal, B.; Heuclin, H.; Pedetti, S.; Dubertret, B. *Nano Lett.* **2013**, *13*, (7), 3321-3328.

197. Ithurria, S.; Talapin, D. V. *J. Am. Chem. Soc.* **2012**, 134, (45), 18585-18590.
198. Mahler, B.; Nadal, B.; Bouet, C.; Patriarche, G.; Dubertret, B. *J. Am. Chem. Soc.* **2012**, 134, (45), 18591-18598.
199. Tessier, M. D.; Spinicelli, P.; Dupont, D.; Patriarche, G.; Ithurria, S.; Dubertret, B. *Nano Lett.* **2013**, 14, (1), 207-213.
200. Brovelli, S.; Schaller, R. D.; Crooker, S. A.; García-Santamaría, F.; Chen, Y.; Viswanatha, R.; Hollingsworth, J. A.; Htoon, H.; Klimov, V. I. *Nat Commun* **2011**, 2, 280.
201. Soni, U.; Pal, A.; Singh, S.; Mittal, M.; Yadav, S.; Elangovan, R.; Sapra, S. *ACS Nano* **2014**, 8, (1), 113-123.
202. Pelton, M.; Ithurria, S.; Schaller, R. D.; Dolzhenkov, D. S.; Talapin, D. V. *Nano Lett.* **2012**, 12, (12), 6158-6163.
203. Tessier, M. D.; Javaux, C.; Maksimovic, I.; Loriette, V.; Dubertret, B. *ACS Nano* **2012**, 6, (8), 6751-6758.
204. Maserati, L.; Moreels, I.; Prato, M.; Krahne, R.; Manna, L.; Zhang, Y. *ACS Appl. Mater. Interfaces* **2014**, 6, (12), 9517-9523.
205. Duncan, T. V.; Méndez Polanco, M. A.; Kim, Y.; Park, S.-J. *J. Phys. Chem. C* **2009**, 113, (18), 7561-7566.
206. Pick Chung, L.; Robert, A. N.; Masud, M.; Nasser, P. *Nanotechnology* **2013**, 24, (1), 015501.
207. Ramamoorthy, R.; Dutta, P. K.; Akbar, S. A. *Journal of Materials Science* **2003**, 38, (21), 4271-4282.
208. Troyanovsky, I.; Sadovskii, N.; Kuzmin, M.; Mosharov, V.; Orlov, A.; Radchenko, V.; Phonov, S. *Sensor Actuat. B-Chem.* **1993**, 11, (1&2), 201-206.
209. Cordero, S. R.; Carson, P. J.; Estabrook, R. A.; Strouse, G. F.; Buratto, S. K. *J. Phys. Chem. B* **2000**, 104, (51), 12137-12142.
210. Meng, C.; Xiao, Y.; Wang, P.; Zhang, L.; Liu, Y.; Tong, L. *Adv. Mater.* **2011**, 23, (33), 3770-3774.
211. García-Santamaría, F.; Brovelli, S.; Viswanatha, R.; Hollingsworth, J. A.; Htoon, H.; Crooker, S. A.; Klimov, V. I. *Nano Lett.* **2011**, 11, (2), 687-693.
212. Galland, C.; Ghosh, Y.; Steinbruck, A.; Sykora, M.; Hollingsworth, J. A.; Klimov, V. I.; Htoon, H. *Nature* **2011**, 479, (7372), 203-207.
213. Jha, P. P.; Guyot-Sionnest, P. *ACS Nano* **2009**, 3, (4), 1011-1015.

214. Javaux C; MahlerB; DubertretB; ShabaevA; Rodina, A. V.; EfrosAl, L.; Yakovlev, D. R.; LiuF; BayerM; CampsG; BiadalaL; BuilS; QuelinX; Hermier, J. P. *Nat Nano* **2013**, 8, (3), 206-212.
215. Galland, C.; Ghosh, Y.; Steinbrück, A.; Hollingsworth, J. A.; Htoon, H.; Klimov, V. I. *Nat Commun* **2012**, 3, 908.
216. Ingole Pravin, P.; Hickey Stephen, G.; Waurisch, C.; Gaponik, N.; Eychmüller, A., Effect of Electrochemical Charge Injection on the Photoluminescence Properties of CdSe Quantum Dot Monolayers Anchored to Oxide Substrates. In *Zeitschrift für Physikalische Chemie*, 2013; Vol. 227, p 1173.
217. Boehme, S. C.; Wang, H.; Siebbeles, L. D. A.; Vanmaekelbergh, D.; Houtepen, A. J. *ACS Nano* **2013**, 7, (3), 2500-2508.
218. Shim, M.; Guyot-Sionnest, P. *Nature* **2000**, 407, (6807), 981-983.
219. Padilha, L. A.; Robel, I. n.; Lee, D. C.; Nagpal, P.; Pietryga, J. M.; Klimov, V. I. *ACS Nano* **2011**, 5, (6), 5045-5055.
220. Wolfbeis, O. S. *Adv. Mater.* **2008**, 20, (19), 3759-3763.
221. Gregory, J. W.; Sullivan, J. P.; Raman, G.; Raghu, S. *AIAA J.* **2007**, 45, (3), 568-576.
222. Nagai, H.; Naraoka, R.; Sawada, K.; Asai, K. *AIAA J.* **2008**, 46, (1), 215-222.
223. Gregory, J.; Sullivan, J.; Sakaue, H.; Huang, C. Y., Molecular sensors for MEMS. In *40th AIAA Aerospace Sciences Meeting & Exhibit*, American Institute of Aeronautics and Astronautics: 2002.
224. Dickert, F. L.; Besenböck, H.; Tortschanoff, M. *Adv. Mater.* **1998**, 10, (2), 149-151.
225. Frederiksen, M. S.; Glud, R. N. *Limnol. Oceanogr.* **2006**, 51, (2), 1072-1083.
226. Sánchez-Barragán, I.; Costa-Fernández, J. M.; Sanz-Medel, A.; Valledor, M.; Campo, J. C. *Trends Anal. Chem.* **2006**, 25, (10), 958-967.
227. Babilas, P.; Liebsch, G.; Schacht, V.; Klimant, I.; Wolfbeis, O. S.; Szeimies, R.-M.; Abels, C. *Microcirculation* **2005**, 12, (6), 477-487.
228. Wu, M.; Lin, Z.; Schäferling, M.; Dürkop, A.; Wolfbeis, O. S. *Analytical Biochemistry* **2005**, 340, (1), 66-73.
229. Sakaue, H.; Miyamoto, K.; Miyazaki, T. *J. Appl. Phys.* **2013**, 113, (8), 084901.
230. Wang, X.-d.; Wolfbeis, O. S. *Chem. Soc. Rev.* **2014**, 43, (10), 3666-3761.

231. Mosser, V.; Suski, J.; Goss, J.; Obermeier, E. *Sensor Actuat. A-Phys* **1991**, 28, (2), 113-132.
232. Li, M.; Wang, M.; Li, H. *Opt. Express* **2006**, 14, (4), 1497-1504.
233. Khalil, G. E.; Costin, C.; Crafton, J.; Jones, G.; Grenoble, S.; Gouterman, M.; Callis, J. B.; Dalton, L. R. *Sensor Actuat. B-Chem.* **2004**, 97, (1), 13-21.
234. Demas, J. N.; DeGraff, B. A., Design and Applications of Highly Luminescent Transition Metal Complexes. In *Topics in Fluorescence Spectroscopy*, Lakowicz, J. R., Ed. Springer US: 1994; Vol. 4, pp 71-107.
235. Liu, T.; Guille, M.; Sullivan, J. P. *AIAA J.* **2001**, 39, (1), 103-112.
236. Yasuhiro, E.; Keisuke, A., Effects of Antioxidants on Photodegradation of Porous Pressure-Sensitive Paint. In *22nd AIAA Aerodynamic Measurement Technology and Ground Testing Conference*, American Institute of Aeronautics and Astronautics: 2002.
237. Bell, J. H. In *Accuracy limitations of lifetime-based pressure-sensitive paint (PSP) measurements*, Instrumentation in Aerospace Simulation Facilities, 2001. 19th International Congress on ICIASF 2001, Aug 2001, 2001; pp 5-16.
238. Borisov, S. M.; Vasylevska, A. S.; Krause, C.; Wolfbeis, O. S. *Adv. Funct. Mater.* **2006**, 16, (12), 1536-1542.
239. Stich, M. I. J.; Nagl, S.; Wolfbeis, O. S.; Henne, U.; Schaeferling, M. *Adv. Funct. Mater.* **2008**, 18, (9), 1399-1406.
240. Köse, M. E.; Omar, A.; Virgin, C. A.; Carroll, B. F.; Schanze, K. S. *Langmuir* **2005**, 21, (20), 9110-9120.
241. Ma, J.; Ji-Yao, C.; Guo, J.; Wang, C. C.; Yang, W. L.; Xu, L.; Wang, P. N. *Nanotechnology* **2006**, 17, (9), 2083.
242. Gouterman, M. *J. Chem. Educ.* **1997**, 74, (6), 697.
243. Park, J.; Lee, J.; Kwag, J.; Baek, Y.; Kim, B.; Yoon, C. J.; Bok, S.; Cho, S.-H.; Kim, K. H.; Ahn, G. O.; Kim, S. *ACS Nano* **2015**.
244. Amelia, M.; Lavie-Cambot, A.; McClenaghan, N. D.; Credi, A. *Chemical Communications* **2011**, 47, (1), 325-327.
245. Borisov, S. M.; Klimant, I. *Anal. Chim. Acta* **2013**, 787, 219-225.
246. Baleizão, C.; Nagl, S.; Schäferling, M.; Berberan-Santos, M. N.; Wolfbeis, O. S. *Anal. Chem.* **2008**, 80, (16), 6449-6457.
247. Zhang, G.; Palmer, G. M.; Dewhirst, M. W.; Fraser, C. L. *Nat Mater* **2009**, 8, (9), 747-751.

248. Pinchetti, V.; Meinardi, F.; Camellini, A.; Sirigu, G.; Christodoulou, S.; Bae, W. K.; De Donato, F.; Manna, L.; Zavelani-Rossi, M.; Moreels, I.; Klimov, V. I.; Brovelli, S. *ACS Nano* **2016**, 10, (7), 6877-6887.
249. Dou, Z.; Yu, J.; Cui, Y.; Yang, Y.; Wang, Z.; Yang, D.; Qian, G. *J. Am. Chem. Soc.* **2014**, 136, (15), 5527-5530.
250. Liu, Y.; Guo, H.; Zhao, J. *Chemical Communications* **2011**, 47, (41), 11471-11473.
251. Yoshihara, T.; Yamaguchi, Y.; Hosaka, M.; Takeuchi, T.; Tobita, S. *Angewandte Chemie* **2012**, 124, (17), 4224-4227.
252. Nirmal, M.; Norris, D. J.; Kuno, M.; Bawendi, M. G.; Efros, A. L.; Rosen, M. *Phys. Rev. Lett.* **1995**, 75, (20), 3728-3731.
253. Javaux, C.; Mahler, B.; Dubertret, B.; Shabaev, A.; Rodina, A. V.; Efros, A. L.; Yakovlev, D. R.; Liu, F.; Bayer, M.; Camps, G.; Biadala, L.; Buil, S.; Quelin, X.; Hermier, J. P. *Nat. Nanotechnol.* **2013**, 8, (Copyright (C) 2014 American Chemical Society (ACS). All Rights Reserved.), 206-212.
254. Park, Y. S.; Malko, A. V.; Vela, J.; Chen, Y.; Ghosh, Y.; García-Santamaría, F.; Hollingsworth, J. A.; Klimov, V. I.; Htoon, H. *Phys. Rev. Lett.* **2011**, 106, (18), 187401.
255. Nasilowski, M.; Spinicelli, P.; Patriarce, G.; Dubertret, B. *Nano Lett.* **2015**.
256. Christodoulou, S.; Vaccaro, G.; Pinchetti, V.; De Donato, F.; Grim, J. Q.; Casu, A.; Genovese, A.; Vicidomini, G.; Diaspro, A.; Brovelli, S.; Manna, L.; Moreels, I. *J. Mater. Chem. C* **2014**, 2, (17), 3439-3447.
257. Robel, I.; Gresback, R.; Kortshagen, U.; Schaller, R. D.; Klimov, V. I. *Phys. Rev. Lett.* **2009**, 102, (17), 177404.